LA-8940-HDR

UC-66a
Issued: September 1981

Evaluation of the Second Hot Dry Rock Geothermal Energy Reservoir: Results of Phase I, Run Segment 5

G. A. Zyvoloski
R. L. Aamodt
R. G. Aguilar
D. A. Counce
H. N. Fisher
T. A. Grant*
C. O. Grigsby
R. H. Hendron
C. E. Holley, Jr.
R. G. Lawton
H. D. Murphy
C. Pearson
R. M. Potter
P. E. Trujillo, Jr.

---

*The Zia Company, Los Alamos, NM 87544.

Los Alamos
Los Alamos National Laboratory
Los Alamos, New Mexico 87545

DISCLAIMER

CONTENTS

ABSTRACT 1

1. HISTORICAL BACKGROUND 2

2. OPERATIONS 6
  2.1. Operational Sequence 6
  2.2. Data Acquisition 6
  2.2.1. Surface Loop System 6
  2.2.2. Downhole System 7
  2.3. Barber-Nichols 60-kW Electrical Generating Unit 8

3. RESERVOIR GEOMETRY 10

4. WATER LOSSES 12
  Comparison with Diffusion Model 15

5. FLOW IMPEDANCE 19
  Distributed Impedances 19

6. HEAT TRANSFER 26
  6.1. Temperature and Flow Data 26
  6.2. Multiple-Fracture Model 28
  6.3. Independent-Fracture Model 34
  Description and Genesis of the Model 34
  6.4. Comparison of the Models 39
  6.5. Comparison of Reservoir Geometry Determined by Heat-Transfer Modeling with Geometry Determined by Microseismicity 41

7. GEOCHEMISTRY 47
  7.1. Variation in Concentrations with Time 47
  7.2. Geochemical Behavior of the Reservoir 52
  7.3. Geothermometry 54
  7.4. Fresh-Water Flush 56
  7.5. Dissolved Gases 61
  7.6. Radon 62
  7.7. Comparison with Previous Experiments 63

8. RADIOACTIVE AND DYE TRACER EXPERIMENTS 65
  8.1. Tracer Volume Studies 66
  8.2. Fracture Mapping with Radioactive Tracers 71
  8.2.1. Properties of Fractures in the EE-1 Openhole 74
  8.2.2. Properties of Fractures Cutting Across the EE-1 Borehole . 74
  8.2.3. Properties of Fracture Intersections with the GT-2B Openhole 78

9. SEISMICITY 80

10. CONCLUSIONS 83

ACKNOWLEDGMENTS 83

REFERENCES 84

APPENDIX A: DEFINITIONS OF STATISTICAL VOLUMES 87

APPENDIX B: SAMPLING AND ANALYSIS PROCEDURES FOR RUN SEGMENT 5 . . 88
1. WATER SAMPLING PROCEDURES 88

2. WATER ANALYSIS PROCEDURE 89
2.1. Total Suspended Solids (TSS) 89
2.2. PH, EH, HCO_3^-, CO_3^-, and Conductivity 89
2.3. Silica 90
2.4. Boron 91
2.5. Atomic Absorption Analysis 91

3. DISSOLVED GAS SAMPLES 93

EVALUATION OF THE SECOND HOT DRY ROCK GEOTHERMAL ENERGY RESERVOIR: RESULTS OF PHASE I, RUN SEGMENT 5

by

G. A. Zyvoloski, R. L. Aamodt, R. G. Aguilar, D. A. Counce,
H. N. Fisher, T. A. Grant, C. O. Grigsby, R. H. Hendron, C. E. Holley, Jr.,
R. G. Lawton, H. D. Murphy, C. Pearson, R. M. Potter, and P. E. Trujillo, Jr.

ABSTRACT

The results of a long-term (286 day) flow test of the second hot dry rock reservoir at the Fenton Hill field site are presented. This second reservoir was created by fracturing an interval of granitic rock located at a depth of 2.93 km (9620 ft) in the same wellbore pair used in the creation of the first, smaller reservoir. The new fracture system has a vertical extent of at least 320 m (1050 ft), suggesting that the combined heat-transfer area of the old and new fracture systems is much greater than that of the old system. The virgin rock temperature at the bottom of the deeper interval was 197°C (386°F).

Downhole measurements of the water temperature at the reservoir outlet, as well as temperatures inferred from geothermometry, showed that the thermal drawdown of the reservoir was about 8°C, and preliminary estimates indicate that the minimum effective heat-transfer area of the new reservoir is 45 000 m^2 (480 000 ft^2), which is six times larger than the first reservoir. Thermal energy was extracted at a rate of 3 MW. Reservoir residence time studies with sodium fluorescein and irradiated ammonium bromide indicate that the volume of the second reservoir is nine times larger than that of the first reservoir. Near the end of the experiment the rate of water loss permeated to the rock surrounding the fracture system was 4.6×10^{-4} m^3/s (7 gpm).

Despite the much larger fracture size, this loss rate was only 30% more than that of the first reservoir after an equivalent period of time. The flow impedance, a measure of the resistance to circulating flow through the reservoir, was 1.6 GPa s/m^3 (15 psi/gpm) under low back-pressure conditions. The seismic activity observed was slight; the small number of microearthquakes that were observed were attributed to an unrelated drilling operation.

For the first time, electrical power was generated from hot dry rock. The Barber Nichols unit developed 60 kW of electric power and performed well at design conditions. However, mechanical problems made continuous operation during the flow test impossible.

The results of this experiment show that the enlarged system created by fracturing from the same pair of wellbores as the older system possesses a much larger heat-transfer system with only a small price being paid in additional water loss. These results hold great promise for commercial-sized hot dry rock reservoirs.

1. HISTORICAL BACKGROUND

Smith et al.[1] describe in detail the concept of extracting energy from hot dry rock (HDR). Here, only a brief account is given. The basic idea is to form a manmade geothermal reservoir by drilling into low-permeability basement rock to a depth where the temperature is high enough to be useful and form a reservoir by hydraulic fracturing. A circulation loop is formed by drilling a second hole to intersect the hydraulically fractured region. Thermal power would be extracted from this system by injecting cold water down the first hole, forcing the water to sweep by the rock surface into the fracture system, and then returning the hot water to the surface where the thermal energy would be converted to electrical energy or used for other purposes. Pressure in the system would be maintained so that only liquid water would exist.

The HDR reservoirs at Fenton Hill are located in the Jemez Mountains of northern New Mexico as shown in Fig. 1-1. The first deep borehole, Geothermal Test-2 (GT-2) was drilled in granitic rock to a depth of 2.929 km (9610 ft) where the temperature was 197°C (386°F). A series of hydraulic fracturing experiments was then performed in GT-2. Energy Extraction-1 (EE-1) was drilled toward the largest of the GT-2 fractures in an effort to complete the heat-extraction system. Because of survey errors during the directional drilling, the EE-1 borehole did not intersect the GT-2 fracture. Although the EE-1 borehole missed the fracture by only 6 m (20 ft), the impedance was too high to permit a viable

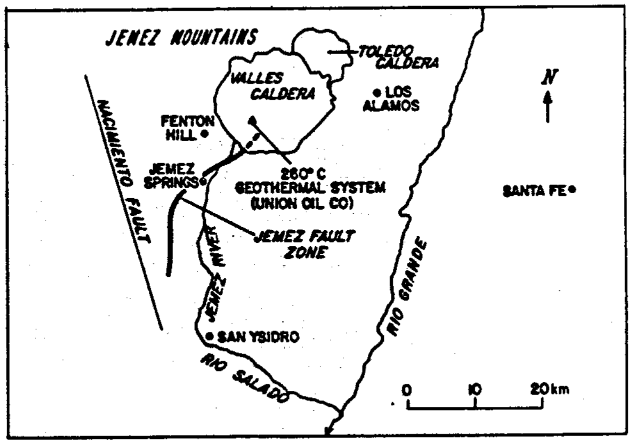

Fig. 1-1.
Location of Fenton Hill Hot Dry Rock site i
the Jemez Mountains of northern New Mexico.

heat-extraction experiment. Various attempts to improve the flow communication between the boreholes,[2] including the hydraulic fracturing of EE-1, proved unsuccessful. Eventually an acceptable connection was achieved by sidetracking GT-2 at 2.5 km and redrilling it towards the top of a large fracture centered at about 2.75 km in EE-1. Several paths were drilled, and eventually one, which penetrated several major natural joints or natural fractures but probably did not intersect the major fracture, was obtained. This path had low enough impedance to proceed with a heat-extraction test. The combination of the original GT-2 wellbore and the redrilling is referred to as the GT-2B wellbore.

Reservoir performance was first evaluated by a 75-day period of closed-loop operation from January 28 to April 13, 1978. Hot water from the production well, GT-2B, was directed to the water-to-air heat exchanger where the water was cooled to approximately 25°C before reinjection. The relatively low power produced did not economically justify the conversion of the geoheat to electricity, so the heat was simply dissipated into the atmosphere by the heat exchanger. The cooled water, in addition to the make-up water that was required to replace downhole losses to the rock surrounding the fractured region, was then pumped down the injection well, EE-1, and through the fracture system. Heat was transferred to the water by conduction within the nearly impervious rock contiguous to the fracture walls, and the heated water was withdrawn by the production well.

The assessment of the first reservoir in EE-1 and GT-2 is referred to as "Run Segment 2," or the "75-day test." (Run Segment 1 consisted of a short precursor experiment conducted in September 1977.) The average thermal power extracted during Run Segment 2 was 4 MW. The flow impedance, initially 1.7 GPa/m^3 (15 psi/gpm), decreased by a factor of 5 as thermal contraction and continued pressurization resulted in the opening of natural joints that provided additional communication with the producing well. Water losses to the rock surrounding the fracture steadily diminished, and eventually this loss rate was less than 1% of the injected rate. The geochemistry of the produced fluid was benign, and the seismic effects associated with heat extraction were immeasurably small. However, the relatively rapid thermal drawdown of the produced water, from 175 to 85°C (345 to 185°F), indicated that the effective heat-transfer area was small, about 8000 m^2 (86 000 ft^2), and essentially confined in a fractured region between the main injection and production zones in the EE-1 and GT-2B wells. Details are found in Refs. 3-5.

It was discovered during a later experiment[6] that, as a result of deteriorated casing cement, the water injected into EE-1 was flowing in the annulus to depths as shallow as 700 m (2500 ft). This posed a potential danger to the ground-water aquifers as well as high water losses. To alleviate these problems, and also to investigate the feasibility of creating a larger fracture from the same wellbores, the EE-1 casing was recemented near its casing bottom at 2.93 km (9600 ft); this eliminated most of the flow communication with the old main EE-1 fracture situated at 2.75 km (9020 ft). A new reservoir was then formed by extending a hydraulic fracture from an initiation depth of 2.93 km (9620 ft) in EE-1. Fracture extension was performed with two massive hydraulic fracturing (MHF) treatments conducted in mid-March of 1979.[7] In the first of these, Expt. 203, 603 m^3 (168 000 gal) of water were injected, whereas 755 m^3 (200 000 gal) were injected during the following Expt. 195. In both cases water was used as the fracturing fluid, with no viscosity-increasing or fluid-loss additives, and the downhole fracturing pressure was raised about 20 MPa (3000 psi) above hydrostatic in both operations. Extensive seismic measurements of the fracturing process were made with downhole geophones, and these, as well as other results, are reported in Ref. 8. The resulting large fracture (described in Sec. 3) propagated upward to at least 2.6 km (8600 ft). Thus, the new fracture appeared to have a minimum inlet-to-outlet spacing of 320 m (1050 ft), more than three times that of the first fracture, which suggested that the effective heat-transfer area might be significantly greater than the first reservoir. Evaluation of the new reservoir was accomplished during a 23-day heat-extraction and reservoir-assessment experiment that began October 23, 1979. This segment of operation with the EE-1/GT-2B well pair was Run Segment 4, or Expt. 215. The results of Run Segment 4 are presented in Ref. 8.

The long-term reservoir characteristics were then investigated in Run Segment 5, or Expt. 217, the subject of this report. The rather lengthy experiment of 286 days was necessary to determine heat-transfer area from thermal-drawdown data. It was also very important to observe water loss and impedance (flow resistance) trends for a long time if the experiment was to be useful in scaling up to a commercial-size reservoir. Run Segment 5 was preceded by a start-up phase in which the flow rate dependence of the impedance was investigated at a number of low flow rates. The results of this phase are reported separately.[9] Similarly, the Stress Unlocking Experiment (SUE) that followed Run Segment 5 is covered in a separate report.[10]

2. OPERATIONS

The general plan for Run Segment 5 was the same used for earlier experiments: inject water into borehole EE-1 and extract the geothermally heated fluid from borehole GT-2B. The heated water was to be cooled with an air-cooled heat exchanger and then recirculated, with the downhole water loss replenished through a make-up pump. A description of the surface equipment may be found in Ref. 3. As the experiment was to be a long-term heat-extraction test, constant surface pressures with essentially constant flow rates would be the mode of operation. The only major perturbation of these conditions was to be a 9-day shut-in midway through the run segment. Wellhead pressures of 9.65 MPa (1400 psi) at EE-1 and 1.38 MPa (200 psi) at GT-2B were planned. The data-acquisition system and techniques are described in Sec. 2.2.

2.1. Operational Sequence

Run Segment 5 was characterized by smooth operation. The pumps were quickly brought up to the desired pressures and remained there except for the scheduled 9-day shut-in at day 68, periodic logging runs, and shut-ins caused by temporary power failures. In the last two-thirds of the experiment, a gradual decrease in the wellhead pressure was observed. This decrease in pressure was attributed to a reduction in input flow due to corrosion of pump impeller surfaces. During the last 120 days of the experiment, a significant increase in the water loss was observed. A leak into the EE-1 annulus was responsible for the increase. This leak also caused a change in the bottom-hole temperature in EE-1. The make-up system was able to handle adequately the increased flow that was required.

2.2 Data Acquisition

The data-acquisition system for Run Segment 5 fell into two categories. One system monitored the surface loop sampling 37 pressures, temperatures, and flow rates. This system was on-line 24 h per day, 7 days per week. The second system was used to obtain data for specialized downhole experiments.

2.2.1. Surface Loop System.

The surface-loop data-acquisition system consists of a Hewlett Packard 9835A desk-top computer and its peripheral equipment. All loop signals are hard wired from the pressure transducers, flow meters, and thermocouples to signal conditioners. The signal conditioners provide power, calibration, and balance networks for the transducers. The conditioner outputs are connected to a multiplexer. The computer controls each relay in the multiplexer individually, allowing a multimeter to read any selected data channel. The multimeter is capable of reading and outputting a signal approximately 18 times per second. The computer was programmed to read the data, integrate and reduce it to engineering units, and display the reduced data on a cathode ray tube. This cycle was repeated approximately every 7 s. Integrated raw data were stored on a floppy disk and integrated reduced data were printed once every hour. If the loop conditions were significantly disturbed by, for example, a power failure, the computer was programmed to store and print data once every minute.

In addition to reading, storing, and printing data, the computer was programmed to check the circulating pump pressures and temperatures on every cycle. If any value exceeded predetermined limits, the computer closed a relay to an alarm warning the operator of a possible emergency situation. If the value exceeded emergency limits, the computer was programmed to shut down the pumps.

An external digital electronics unit was designed to take care of any computer malfunctions. The computer sent a pulse to this unit once every cycle. If, for any reason, the computer hung up and quit sending pulses, the unit interrupted the power to the computer after 90 s. This initiated an automatic computer restart in which the computer read the previous disk file to refresh its memory.

2.2.2. Downhole System. The downhole data-acquisition system is also a computer based system, of the same type as that used for the surface system. It is wired to diesel powered logging rigs, one at each wellbore. Each logging rig has approximately 6100 m (20 000 ft) of spooled, 7-conductor wireline, which is used to lower instrument sondes downhole. On each rig there is an electronic depth counting system to measure the length of wireline that has been lowered downhole. This data-acquisition system was used to take data for downhole measurements such as temperature surveys to obtain downhole temperature distribution, spinner logs to obtain wellbore water velocities, and radioactive tracer logs to locate flow entrances and exits from the wellbores.

The temperature sonde used a thermistor as the temperature transducer. Four wireline conductors are used, two for current excitation and two for voltage sensing leads. During a temperature survey, the computer is programmed to trigger on wireline depth. At the given depth interval, the date, time, thermistor current, and thermistor voltage are read and then stored on a floppy disk. A computer calculates thermistor resistance, and from the calibration relation, it then calculates the temperature, prints the reduced data on an impact printer, and plots the temperature vs depth on an HP9872, four-color, digital plotter.

The spinner sonde is basically a turbine-type flow meter, which measures water velocities relative to the sonde. As the turbine impeller turns, electronic pulses are sent to the surface and converted to frequency. The calculator is programmed to read time, depth, and frequency, store the data, and plot frequency vs depth as fast as possible. Scan times are of the order of one scan per second.

Radioactive tracer logs, using irradiated ammonium bromide, NH_4Br^{82}, at a strength of 400 mCi or less, are used to locate entrances and exits from the wellbores. After the radioactive source was injected into the system, both wellbores were continuously logged with gamma-radiation counters to monitor the paths of the radioactivity. The data acquisition for this type of survey is similar to that for a spinner log except that both wellbores are logged at the same time. On-line plots of gamma-radiation activity vs depth were made for each wellbore.

2.3. Barber-Nichols 60-kW Electrical Generating Unit

In May 1980 an electric generating unit was added to the surface loop. The unit was designed and assembled by Barber-Nichols Engineering to specifications written for the expected conditions at Fenton Hill and for a binary-fluid arrangement. The secondary or working fluid selected was refrigerant 114 (R-114), which was to be vaporized in a shell and tube pool boiler with tube-in-tube preheater. The vapor is expanded through a single-stage axial flow turbine turning at 3600 rpm (60 kW), which exhausts to air cooled condensers. The boiler feed pump is a multistage mixed-flow unit belt driven from the turbine shaft. Specifications were for 140°C inlet geothermal fluid and 4°C ambient air (the annual average at Fenton Hill). A wide range of inlet temperature limits was established.

The installation was completed with the unit in parallel to loop heat exchangers and the generated power being fed into the site secondary power system with safety shut down provisions. Initial start up of the unit was accomplished with very little difficulty and full load was quickly demonstrated. Although the unit had been carefully leak tested before delivery, instrumentation added at installation caused some continuing loss of refrigerant, and after running several weeks the unit was shut down. When additional fluid was finally received, the unit was again operated until a short developed in the generator (a standard 3600 rpm unit). Warranty covered repairs were slow, so a substitute smaller (50 kW) generator was installed for the final few weeks of Run Segment 5. This unit continued satisfactorily to the end of the flow test. The continuous operation of the generating unit was interrupted by the scheduled system shut-ins for wellbore logging and for determining thermal recovery. The operation was also upset by several unexpected problems. Any shut-in caused a rather long downtime for the generating unit because the unit required manual adjustment on each restart. With the small crews running the flow test, this was time consuming.

The summary results indicate a successful electric generating system using R-114 as the working fluid and maintaining the geothermal fluid as superheated water for closed recirculating. The supply temperature was 130°C and operating periods occurred with winter (below 0°C) and summer (~22°C) ambient air. Efficiency for the generating cycle at design conditions is 5.7%, with a source utilization factor of 24.7%. These rather low values may be attributed to the air cooled condenser operating at high altitude and the parasite loads associated with the unit.

3. RESERVOIR GEOMETRY

The reservoir geometry can be inferred from several different experiments and a variety of data. The most common data used are that obtained from tracer, spinner and temperature logs, and heat-extraction experiments. These experiments, together with the assumption that the minimum earth stress at reservoir depth is in the horizontal direction, have led to the inferred fracture geometry shown in Figs. 3-1 and 3-2.

Figure 3-1 is an early conceptual model of the system showing the small fracture (Run Segment 2) and the larger fracture (Run Segments 4 and 5) connected by a set of nonvertical natural joints with a dip of about 60° from the horizontal. Note that the fractures are shown to be circular in Fig. 3-1. This is only speculation. However, unlike oil and gas reservoirs where distinct changes in the lithology, such as upper and lower confining shale layers, result in roughly rectangular fractures, it is thought that the

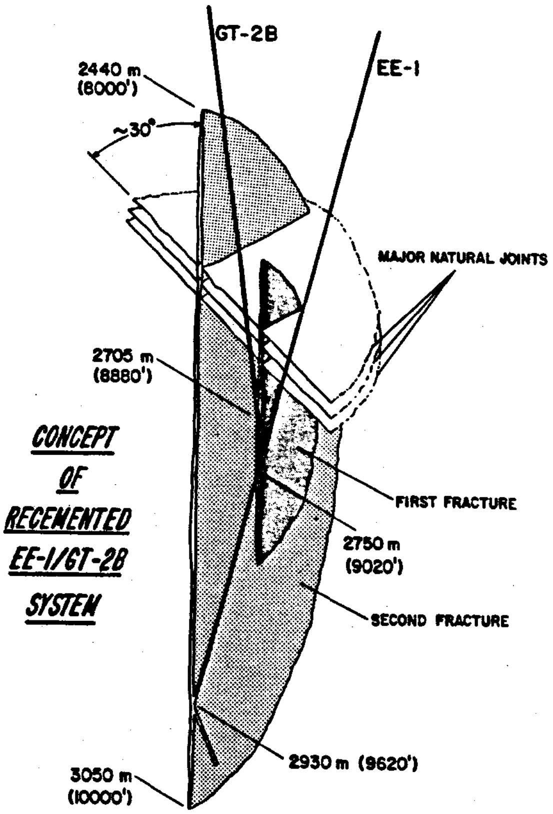

Fig. 3-1.
Inferred reservoir geometry (early conception).

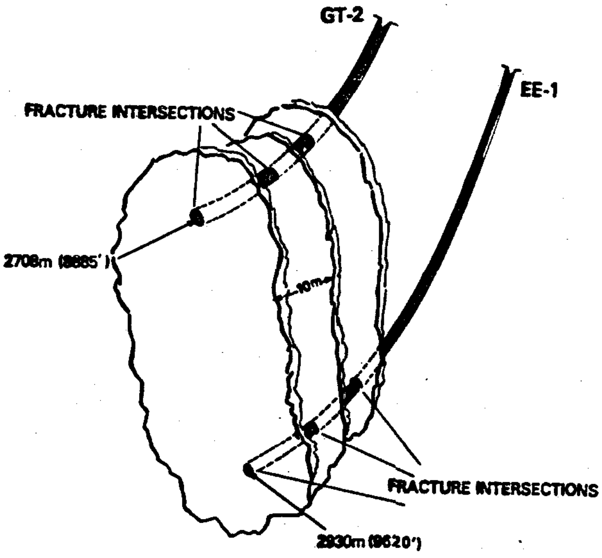

Fig. 3-2.
Inferred reservoir geometry (present conception.

fractures in this HDR system are roughly circular because of the gross homogeneity of the rock. Almost all the heat-transfer area in this model of the system is in the two fractures. The independent-fractures model (discussed in Sec. 6.3) is based on this representation of the reservoir. Based on heat-transfer analysis, the area of the first fracture was initially put at 8000 m^2, which gives an equivalent diameter of 100 m. In contrast, heat-transfer analysis puts the larger fracture at 35 000 m^2, or an equivalent diameter of about 200 m^2.

Figure 3-2 is a more recent view of the system. This model is characterized by a multitude of vertically oriented fractures. This view of the reservoir evolved after a detailed analysis of temperature drawdown and recovery curves in both wellbores (more details are given in Sec. 6.1). This model gave a total heat-transfer area of the reservoir of 45 000 m^2.

4. WATER LOSSES

The water loss of an HDR system is very important because this water must be provided from some outside source. This information can be vital for environmental as well as economic reasons. The water-loss rate, that is, the rate at which water permeates the rock formation surrounding the fracture system, is the difference between the injection rate and the produced, or recovered, rate at GT-2B. The water loss rate is a strong function of system pressures and flow rate. Wellhead pressures and flow rates for Run Segment 5 are presented in Figs. 4-1 and 4-2. The actual measurement of the volumetric rate of water loss was performed with the make-up water flow meter except for short periods when these data were not available. Then the actual difference between the EE-1 and GT-2 wellhead flow rate was used. Because the make-up pump provides the difference between the injection rate and the produced flow rate (after the latter is cooled by the heat exchanger), this measurement eliminates nearly all of the small error that would be caused by temperature induced density differences.

It is interesting to compare the results of this experiment with that of previous experiments. In this way the relationship between system size and water loss may be examined. Direct comparisons of the raw data indicate that the water-loss rates for the enlarged reservoir evaluated in Run Segments 4 and 5 are approximately 40% higher than the smaller, first reservoir evaluated in Run Segment 2 (the 75-day test). Because the operating pressure (EE-1 surface pressure) was ~10% higher during Run Segment 5, the reservoir parameters governing water loss were not more than 30% greater for Run Segment 5 as compared to Run Segment 2.

Use of the pressure-dependent diffusion model[3,8,11] confirms this comparison. Curve fitting to the water-loss-rate data from Run Segment 5 with this model also indicates that the reservoir parameters that determine the response to short-term pressure transients are different than the parameters of the first reservoir tested in Run Segment 2.[11] These short-term transients reflect local properties of the reservoir and indicate that flow in the lower part of the reservoir is governed by a higher stress than the earlier reservoir.

Figures 4-3 and 4-4 are the data for the duration of Run Segment 5. Figure 4-3 is the water-loss rate as measured by the make-up pump flow meter, and Fig. 4-4 is the integral of the water-loss rate. Starting about day 150,

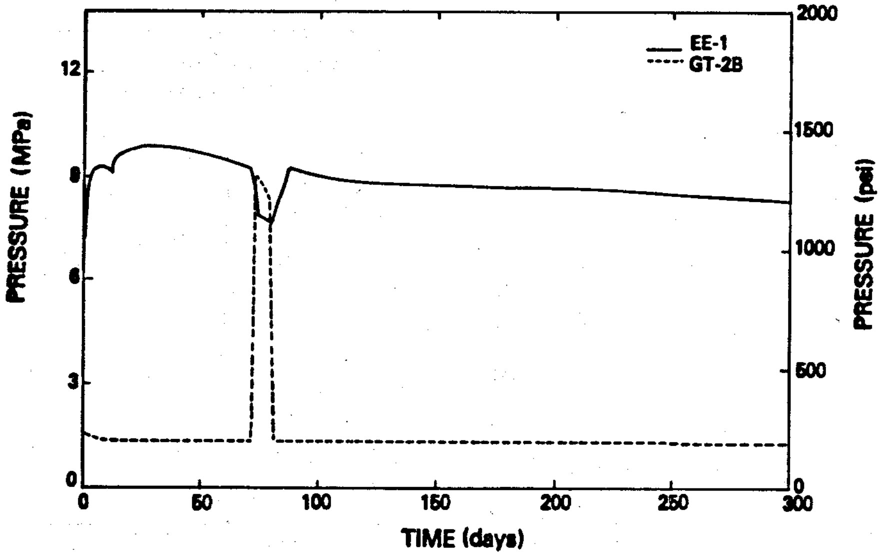

Fig. 4-1.
Wellhead pressures for Run Segment 5.

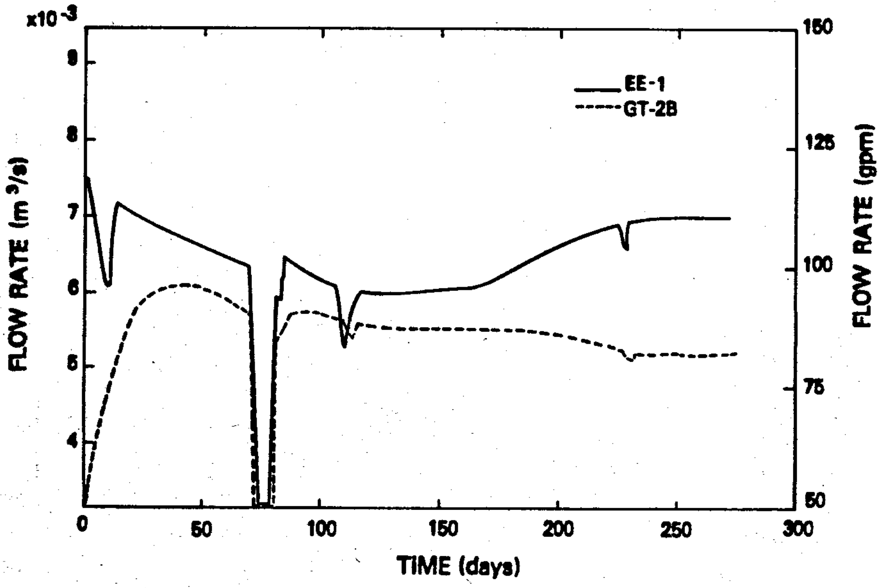

Fig. 4-2.
Wellbore flow rates for Run Segment 5.

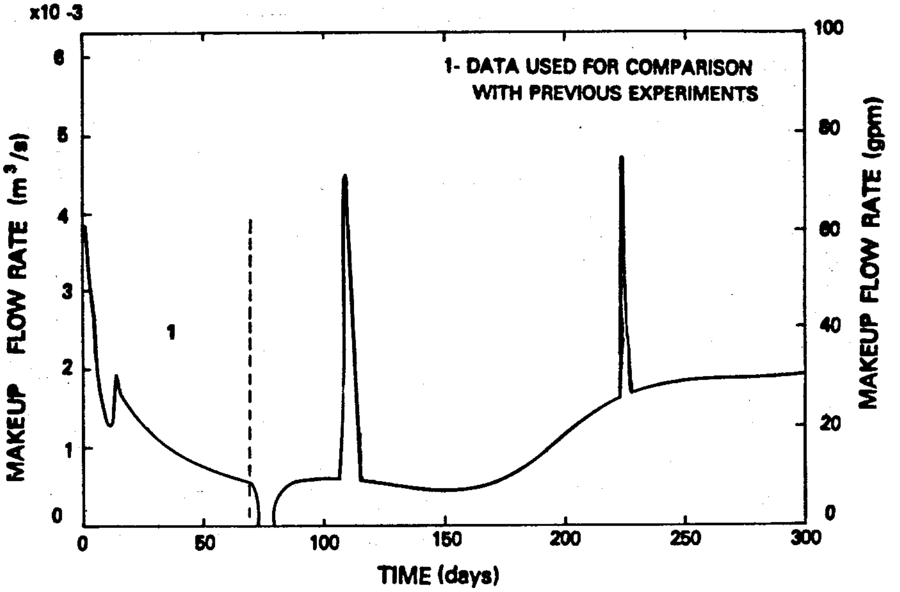

Fig. 4-3.
Water-loss rate for Run Segment 5.

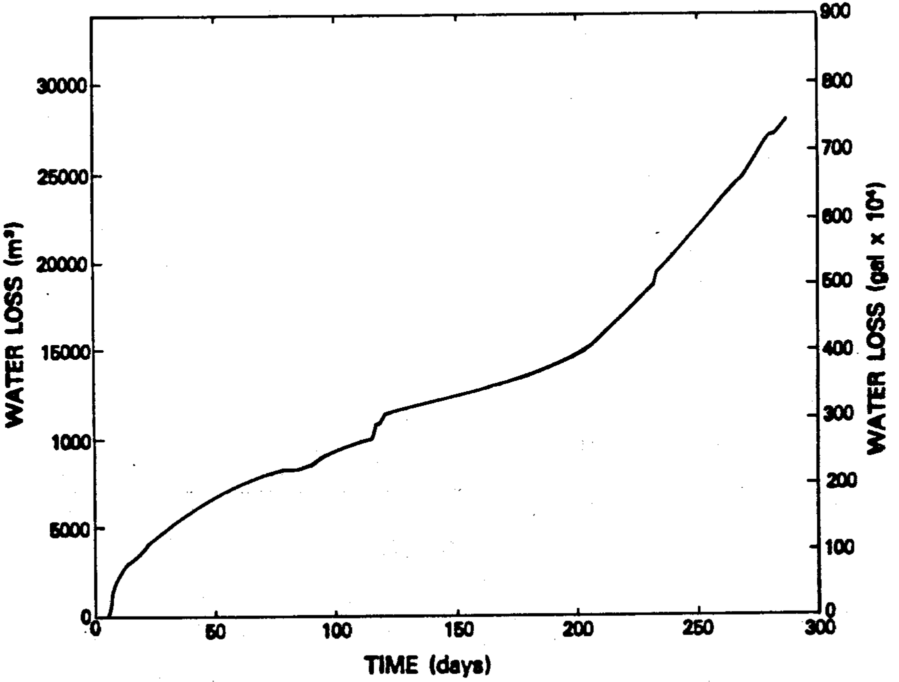

Fig. 4-4.
Cumulative water loss for Run Segment 5.

a fracture connection from the pressurized reservoir formed in the annulus region of EE-1, resulting in flow to the surface through the annulus. This caused the water make-up to increase dramatically and made it difficult to analyze the water loss during the last 130 days of the experiment. There was also another perturbation in the water-loss data caused by a 7-day shut-in experiment starting on day 74. For these reasons the first 70 days [labeled (1) in Fig. 4-3] are used for comparison with other experiments.

The water-loss flow rate for Run Segment 2 is displayed in Fig. 4-5. The data contain many operational transients and are smoothed by a fit to the pressure-dependent flow model.[3] The break in the data at (1) in Fig. 4-5 is due to the start of a slow pressure decline in EE-1. The extremely low values of flow at the end of the experiment are due to this transient[3] and should not be used for comparisons with the Run Segment 5 system. The early time data are best suited for comparison with other systems.

Water-loss measurements were also made during the high back-pressure experiment (Run Segment 3, also known as Expt. 186, Ref. 6) with both EE-1 and GT-2 pressurized. The loss rates of that experiment were equal to or greater than those of Run Segment 5. The exact amount depends on how much is allotted to the annulus leak at early times. Reference 6 should be consulted for details.

A direct comparison of Figs. 4-3 and 4-5 shows that for the first 30 days, the loss rates of Run Segment 5 are somewhat higher than Run Segment 2. Because of the existence of so many transients, however, the easiest comparison is on the accumulative or integrated losses that smooth out the transients. These integrated losses are shown in Fig. 4-6. The dashed curve (2) is the Run Segment 2 result scaled linearly to the Run Segment 5 pressure. The remaining difference is only 30% of the Run Segment 2 losses.

Comparison With Diffusion Model

The development of the mathematical model for water loss is described in detail in Ref. 11 and will not be presented here. The computer code used was the AYER finite-element code that is described in Ref. 12. The diffusion model and the resulting fits to the Run Segment 2 data (the dashed curve of Fig. 4-5) are detailed in Refs. 3 and 11; and, for Run Segment 3, in Ref. 6. The best fit obtained thus far to the Run Segment 5 data is shown in Fig. 4-7. The flow transient located at 15 days is induced by the pressure steps at 15 days (1) in Fig. 4-3.

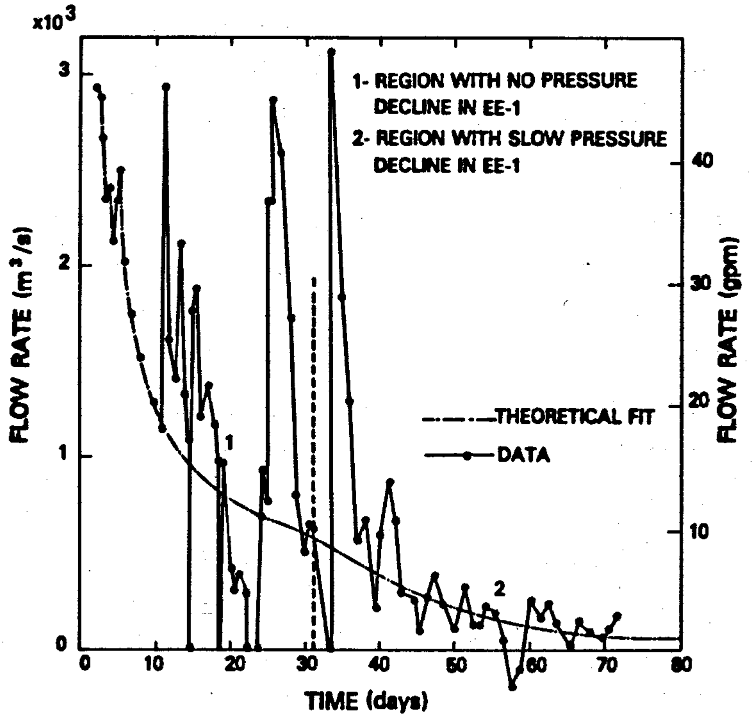

Fig. 4-5.
Water-loss rate for Run Segment 2 with comparison of computer model data fits.

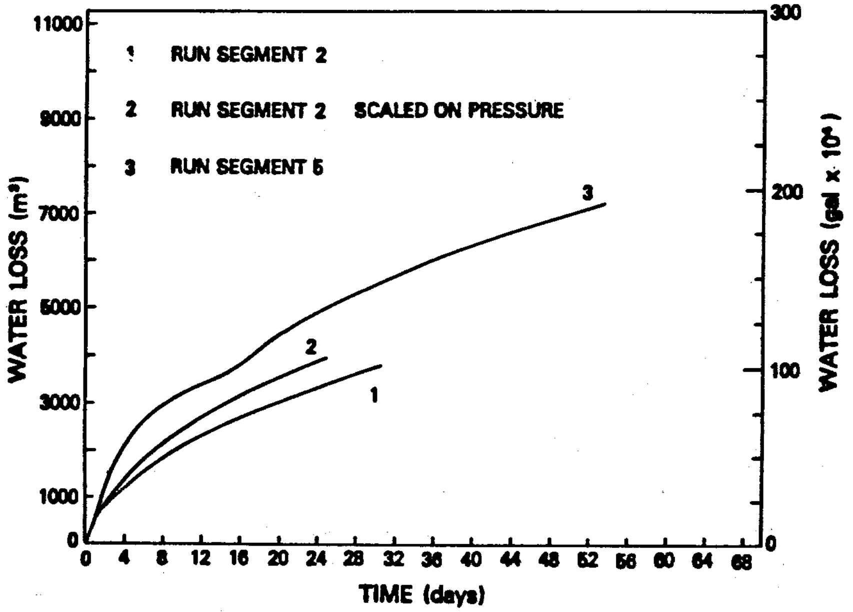

Fig. 4-6.
Comparison of cumulative water loss for Run Segments 2 and 5.

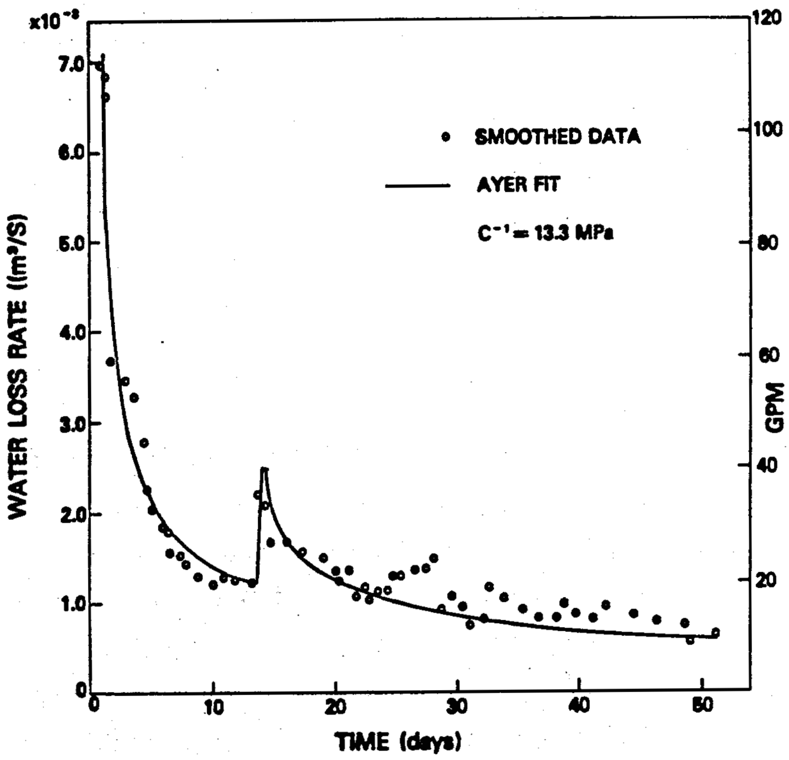

Fig. 4-7.
Water-loss rate for Run Segment 5 showing results from computer modeling.

These fits are most sensitive to two parameters. (1) The reservoir flow receptivity α, $\alpha = A\sqrt{k\beta}$ is evaluated at starting or hydrostatic pressure. Here, A is the diffusing area, k the permeability, and β the system compressibility. (2) C is a constant that determines the pressure dependence of α as

$$\alpha \propto \frac{1}{(1 - CP)^{\eta}}$$

(see Ref. 3). This parameter is best interpreted as the reciprocal of the sum of the confining stress and a fracture modulus.

The current best values for α at hydrostatic pressure and C^{-1} obtained from the fits are summarized in the following table.

Run Segment	α ($m^3 MPa^{-1/2}$)*	C^{-1}(MPa)
2	1.4×10^{-6}	9.3
3	$1.4 \times 10^{-6} \alpha$--$2.8 \times 10^{-6}$	9.3
5	1.9×10^{-6}	13.3--20.0

The α for Segment 5 is 30% higher than that for Run Segment 2 and probably reflects the addition of the lower portion of the reservoir, that is, the reservoir enlargement. The value of C was determined mainly by one flow transient in Run Segment 5. The range of C^{-1} indicated in the table reflects the lack of sensitivity of the parameter. Short-term transients, even in the water losses, affect some local parameters. Perhaps the response of the lower portion of the reservoir is determined by a larger component of _in situ_ stress.

---

*In all previous reports α has been reported as the one-sided or one-half the measured value. Also β in α has been normalized to a rock compressibility of 2.7×10^{-5} MPa^{-1}. Here both of these conventions have been discarded and α is reported as the full measured value in SI units.

5. FLOW IMPEDANCE

The flow impedance, defined as the difference of the inlet and outlet pressures divided by the outlet flow rate, is an important parameter used in determining pumping requirements. In addition, knowledge of the distribution of impedance may help to understand the fracture geometry.

Measurements of impedance for the main flow period (March 10 to December 8) are shown in Fig. 5-1, both uncorrected and with buoyancy corrections. The uncorrected impedance is simply the difference between the injection and production wellhead pressures divided by the circulated through-flow rate measured at the GT-2B production wellhead. The corrected impedance accounts for the fact that the water in the injection well was colder than in the production well so an additional pressure difference existed because of density variations. The calculated pressure correction as a result of these density variations is shown in Fig. 5-2. Wellbore temperatures were estimated with a transient heat transmission code.[13] Generally, uncorrected impedances are 20% lower than corrected values. In reviewing the overall impedance behavior shown in Fig. 5-1, it may be helpful to refer back to Figs. 4-1 and 4-2, which show wellhead pressures and flow rates for the same period of time.

Note that the fracture system described in the section on system geometry had an impedance of 14.2 GPa s/m^3 (130 psi/gpm) before the hydraulic fracture treatments of March 1979. During Run Segment 4 the impedance was nearly constant at about 1.8 GPa s/m^3 (17 psi/gpm), corrected for buoyancy. One of the goals of Run Segment 5 was to observe the impedance behavior during a long-term heat-extraction test.

Distributed Impedances

The overall flow impedance shown in Fig. 5-1 is thought to be the sum of several components, such as impedances associated with restricted flow paths at wellbore-fracture intersections and flow resistances distributed along the fractures. Shut-in experiments have proved useful in determining the distribution of impedances in the wellbore fracture system. This information may then be used in attempts to decrease the impedance.

A number of temporary shut-ins of EE-1 and GT-2B were scheduled during Run Segment 5. During these short ($\sim$1-h) shut-ins the pressures in both wells were monitored at the surface. Figure 5-3 shows a typical pressure-time plot from one such shut-in. As demonstrated in Run Segment 4, the EE-1 pressure P approaches a value, P_a, which can be chosen so that, after a short transient

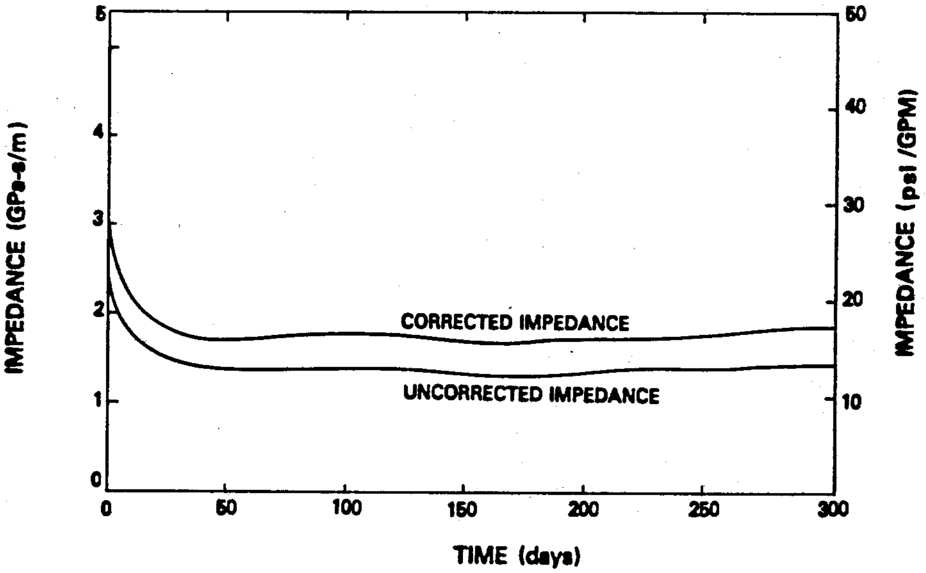

Fig. 5-1.
Uncorrected and corrected for buoyancy impedances during Run Segment 5.

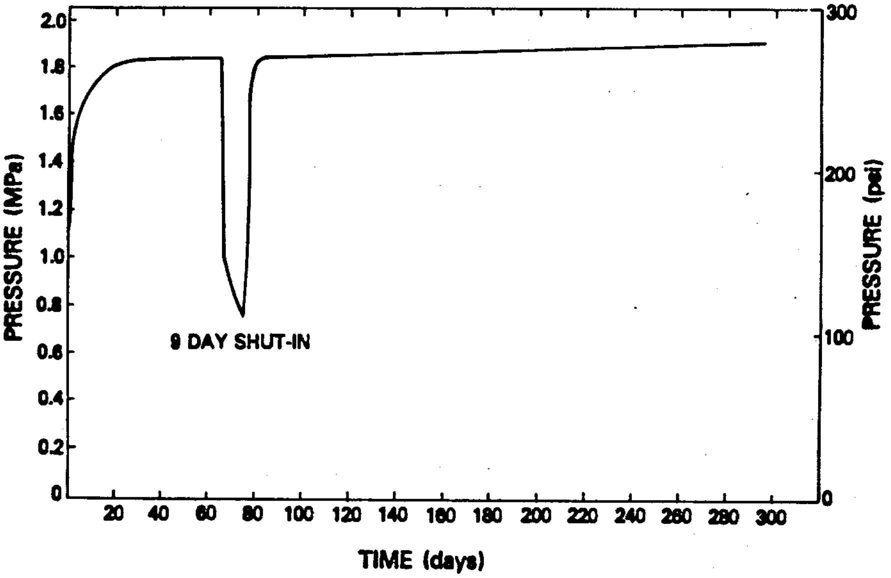

Fig. 5-2.
Buoyancy pressure correction during Run Segment 5.

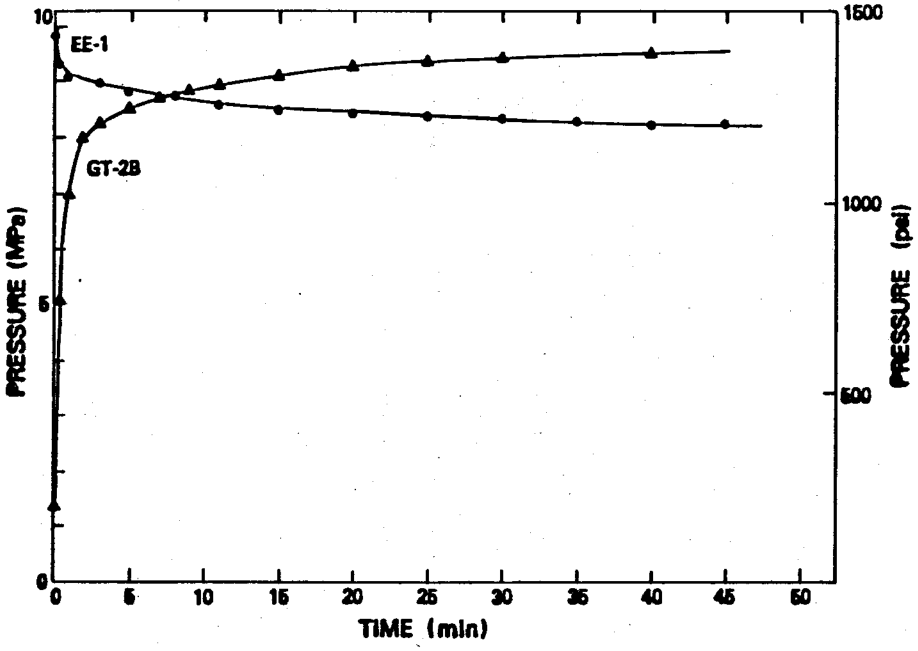

Fig. 5-3.
Example pressure-time plot for distributed buoyancy calculations.

period, the plot of log $(P-P_a)$ vs time over the shut-in time period is linear. The straight line that best fits this data is calculated and extrapolated to zero time. The pressure intercept P at zero time is denoted P_0. Computer calculations have shown that P_0 is the surface pressure corresponding to a point near the fracture entrance, and the impedance from the EE-1 wellbore to this point is defined to be the entrance impedance Z_1.

Similarly, the pressure in the exit well rises towards another asymptotic value, P_a, when the well is shut-in, and a plot of log (P_a-P) is linear when P_a is properly chosen. As before, a value of P_0 and the exit impedance, Z_2, can be found.

Table 5-I shows the parameters P_c (the initial pressure before shut-in), P_0, P_a, the flow rate $\dot{Q}$ before shut-in, and the entrance and exit impedances, Z_1 and Z_2, for the seven shut-in experiments in Run Segment 5.

With these values, it is possible to deduce the total impedance through the fracture without calculating the buoyancy correction (that is, the difference in pressure at the bottom of the reservoir due to density differences in the hot and cold wells) as follows: Let P_{0E} and P_{0G} be the pressures at the surface as deduced from the extrapolated semilog plots discussed above and shown in Table 5-I, while P_1 and P_2 are the corresponding pressures inside the

TABLE 5-I

INITIAL WELLHEAD PRESSURES, P_c, AND EXTRAPOLATED PRESSURES, P_o AND P_a, DETERMINED FROM SHUT-IN DATA

	EE-1					GT-2B				
	Pressure (MPa)			Flow		Pressure (MPa)			Flow	
Date (1980)	P_c	P_o	P_a	Q ($m^3/s \times 10^{-3}$)	Z_1 (GPa·sec/m^3)	P_c	P_o	P_a	Q ($m^3/s \times 10^{-3}$)	Z_2 (GPa·sec/m^3)
4/14	9.786	8.958	8.201	6.88	0.12	1.323	8.441	9.821	6.43	1.107
4/28	9.669	8.947	8.263	6.69	0.108	1.323	8.416	9.883	5.93	1.196
5/20	9.284	8.494	7.919	6.37	0.124	1.296	8.251	9.559	6.12	1.136
6/26	8.925	8.204	7.746	6.06	0.119	1.323	8.093	9.469	5.80	1.167
7/27	8.753	7.916	7.491	5.99	0.14	1.316	8.091	9.29	5.68	1.193
9/03	8.560	7.769	7.526	5.95	0.132	1.206	7.881	9.097	5.93	1.116
11/05	8.573	7.23	6.809	7.13	0.188	1.158	7.041	8.325	5.58	1.054

fracture. Let P_{aE} and P_{aG} be the asymptotic surface pressures given in Table 5-II. Referring to Fig. 5-4, define ρ_1 as the mean density in the EE-1 well and ρ_2 in GT-2B. Let $\dot{Q}_1$ and $\dot{Q}_2$ be the corresponding flows. Assume that the mean flow through the fracture impedance, Z_F, (the impedance remaining after the entrance and exit impedances, Z_1 and Z_2, are removed) is $(\dot{Q}_1 + \dot{Q}_2)/2 = \dot{Q}$, and the density of fluid in the fracture is $(\rho_1 + \rho_2)/2$. Then

$$P_{OE} - P_{OG} = P_1 - P_2 - \rho_1 g h_1 + \rho_2 g h_2, \quad (1)$$

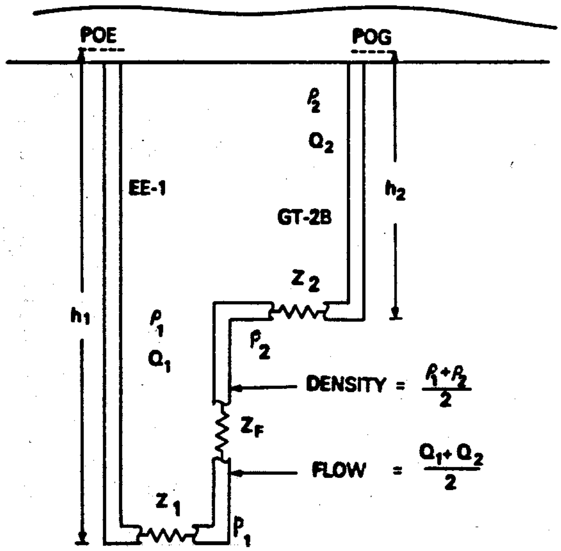

Fig. 5-4.
Wellbore and fracture model for distributed impedance calculations.

and

$$P_1 - P_2 = \dot{Q} Z_F + (\rho_1 + \rho_2) g (h_1 - h_2)/2 , \quad (2)$$

where g is the acceleration due to gravity. Combining these equations, we have

$$P_{OE} - P_{OG} = \dot{Q} Z_F - (\rho_1 - \rho_2) g (h_1 + h_2)/2 . \quad (3)$$

Then the pressure difference, $P_{aE} - P_{aG}$, should be given by Eq. (3) after all internal flow has ceased, that is, P_1 and P_2 differ by the hydrostatic head:

$$P_{aE} - P_{aG} = - (\rho_1 - \rho_2) g (h_1 + h_2)/2) . \quad (4)$$

Substituting from Eq. (4) into Eq. (3),

$$Z_F = (P_{OE} - P_{OG} + P_{aG} - P_{aE})/\dot{Q} . \quad (5)$$

Table 5-II gives the values of Z_1, Z_2, Z_F, and total impedance Z as determined in this manner.

The mean value of the total impedance, Z, is 1.57 GPa s/m^3 (14.35 psi/gpm), about 0.1 GPa s/m^3 less than the value obtained using the total

TABLE 5-II

CALCULATION OF LOCAL IMPEDANCES FROM SHUT-IN DATA

Date (1980)	$P_{OE} - P_{OG}$	$P_{aG} - P_{oG}$	$Q = (Q_1 + Q_2)/2$	Z_F (From Eq. 5)	Z_1	Z_2	Z
4/14	0.517	1.62	6.66	0.321	0.12	1.107	1.548
4/28	0.531	1.62	6.31	0.31	0.108	1.196	1.645
5/20	0.243	1.64	6.25	0.301	0.124	1.136	1.561
6/26	0.111	1.723	5.93	0.309	0.119	1.167	1.595
7/27	-0.175	1.799	5.84	0.278	0.14	1.193	1.611
9/03	-0.112	1.571	5.96	0.245	0.132	1.126	1.503
11/05	0.189	1.516	6.36	0.268	0.188	1.054	1.510

pressure drop and calculated buoyancy. There appears to be good agreement, considering the assumptions in the two methods, and particularly, that the exit flow only is considered in the usual impedance calculation.

It is of interest to compare the results obtained here with those of Run Segment 4. The entrance region impedance was 0.11 GPa s/m^3 for Run Segment 4, very similar to the initial value in Run Segment 5 of 0.12 GPa s/m^2. During Run Segment 5 a steady increase was noted reaching a value of 0.19 GPa s/m^3 near the end of the run. The fracture impedance was 0.40 GPa s/m^3 for Run Segment 4 and 0.45 GPa s/m^3 for Run Segment 5, and the exit impedance was 1.0 GPa s/m^3 for Run Segment 4 and 1.05 GPa s/m^3 for Run Segment 5. These results suggest there may be small changes in the distribution of impedance due primarily to pressurization and thermal effects, but the overall impedance stayed remarkably constant. In particular, the impedance did not show the large decrease that occurred in Run Segment 2 (75-day test). In that experiment the impedance decreased from about 1.5 GPa s/m^3 to about 0.33 GPa s/m^3. However, a thermal drawdown of about 100°C occurred in Run Segment 2, whereas only 8°C occurred in Run Segment 5.

6. HEAT TRANSFER

The heat-transfer system in Run Segment 5 is complicated and is governed by flow in several large fractures. In the past, analyses of the heat-transfer system were made that assumed a system of independent fractures. In the earlier system of Run Segment 2, this proved useful and good fits were obtained. In the present experiment, drawdown and recovery as well as flow measurements suggest that the reservoir can be modeled best as a system of parallel, thermally interacting fractures. The first model is termed the independent-fractures model, whereas the second is termed the multiple-fracture model. After summarizing the temperature and flow data in Sec. 6.1, the rationale for the new, multiple-fracture model and its results will be presented in Sec. 6.2. The results of the older, independent-fracture model will be presented in Sec. 6.3, and both models will be compared in Sec. 6.4.

6.1. Temperature and Flow Data

The periodic temperature and spinner flow logs taken in GT-2B during Run Segment 5 give a temporal history of the temperature and flow rates of the three fractures that intersect the GT-2B wellbore as depicted in Fig. 3-2. The fracture zones are centered approximately at 2626 m, 2673 m, and 2703 m (depth along wellbore). The temperatures and flows for these zones are plotted in Figs. 6-1, 6-2, and 6-3 along with the total flow in the casing and the mixed temperature in the casing. The reservoir inlet temperatures obtained from three logs in EE-1 are also shown in Fig. 6-1. Several observations can be made immediately.

- The outlet temperatures show little curvature in Fig. 6-1 when plotted on a scale with the inlet temperature near zero on the scale. The small temperature change makes fits to the data insensitive to the details of the model.
- When plotted on a larger scale, the temperatures show regular trends (Fig. 6-3) that allow the determination of approximate reservoir parameters. Early transients in the temperature data can be due to vertical temperature gradients resulting from previous flow experiments. Vertical gradients that cooled before Run Segment 5 are not included in the multiple-fracture model but are included in the independent-fracture model.
- No temperature rise in the wellbore is observed. Only the lower fracture zone shows a significant long-term rise in temperature. This

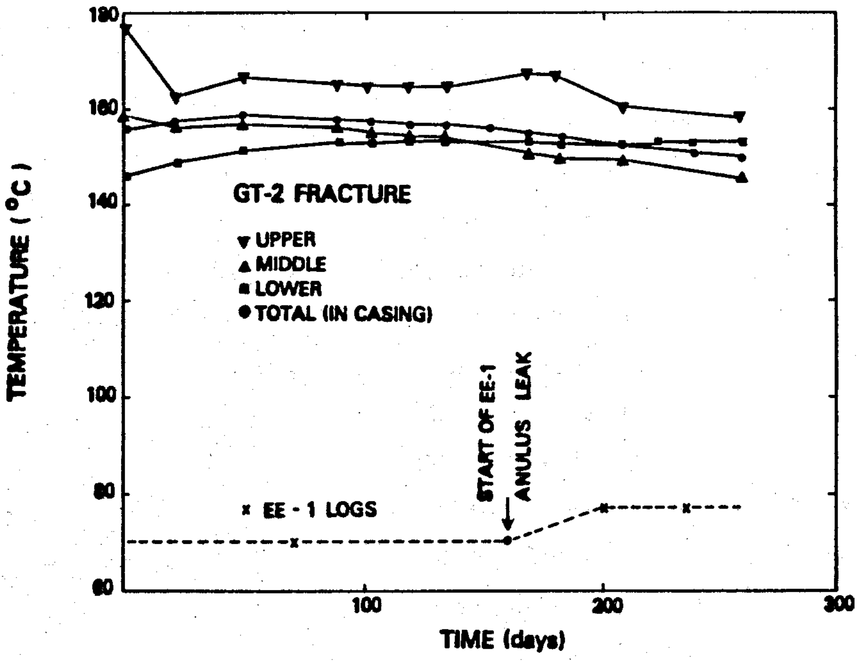

Fig. 6-1.
Temperature history for several regions in the GT-2B wellbore and EE-1 wellbore.

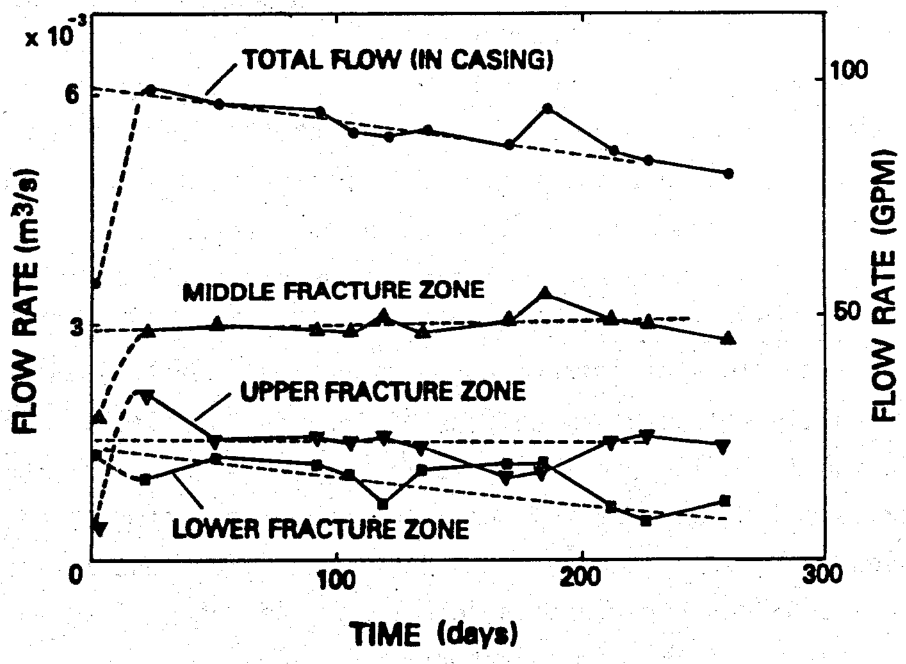

Fig. 6-2.
Flow rate histories in the GT-2B wellbore.

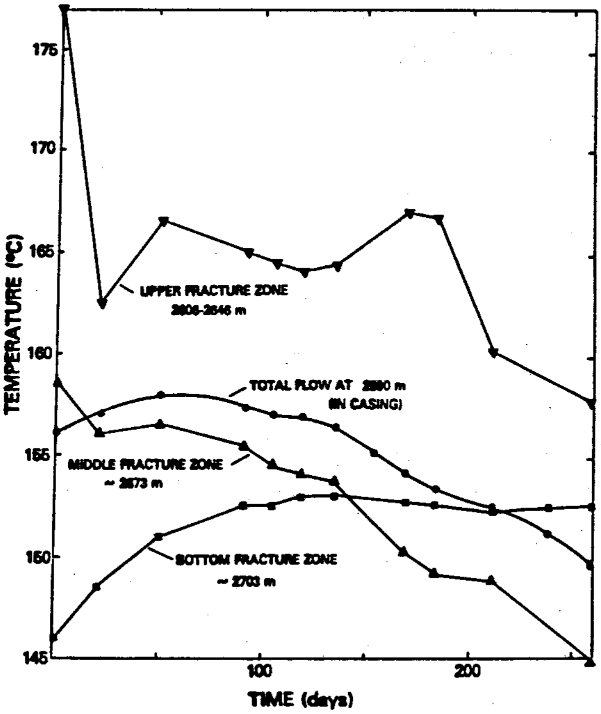

Fig. 6-3.
Temperature history in GT-2B wellbore plotted on an expanded scale.

indicates that only a small fraction of the heat-exchange area is hotter than the mean reservoir.

- The mixed outlet temperature remains near that expected in the recovered temperature field of the previous flow experiments. This infers that most of the heat-exchange area is in the thermally depleted volume of the reservoir and that heat from the lower reservoir acted mainly to warm the old reservoir.
- After the start of the EE-1 annulus leakage flow, the reservoir inlet temperature increased 7°. This preheat of the inlet water indicates a new flow path, and effectively, in some way an enlargement of the system. The increase in inlet temperature is nearly equal to the overall decrease in the average outlet temperature, and thus this preheat must have retarded the drawdown significantly.

6.2. Multiple-Fracture Model

In this section the temperature drawdown data will be interpreted in terms of a multiple-fracture model containing several partly independent flow paths. In the following section a single large fracture is assumed with several flow exits. The evidence for multiple independent flow paths in both the early Phase I reservoir (Run Segments 1, 2, and 3) and the recemented (Run Segments 4 and 5) reservoir exists in much of the data. This evidence will be discussed in terms of three main categories.

(1) Multiple temperature depressions exist in all wellbores after all flow experiments. Spinner and temperature logs in the three production wells (GT-2, GT-2A, and GT-2B) have shown at least five major flow exits distributed over a horizontal distance of almost 40 m (125 ft) and a vertical distance of

80 m (250 ft). Temperature logs in the injection well (EE-1) have shown at least eight major or minor flow exits or crossings in 900 m (2800 ft) vertical and 100 m (300 ft) horizontal. While only two or three of these crossings occur in the reservoir vicinity, the existence of so many crossings in the lower 900 m of EE-1 suggests the propensity for a multiple-fracture system. Figure 6-4 is a temperature log in EE-1 just prior to Run Segment 5. More than a year after recovery, the two peaks of the Run Segments 2 and 3 (thermal depletions of the first reservoir) are still distinguishable. The overall depletion of the first reservoir has the characteristic shape of two superimposed Gaussian-shaped curves that match the recovered temperature field of flat vertical fractures.

(2) The temperature drawdown shows characteristics of independent flow paths. In Fig. 6-3 the lower fracture is seen to draw down at a slower rate than the upper and middle fractures. The temperatures of the lower and middle fractures cross at 140 days. This behavior would be unlikely if the upper and middle fractures were direct extensions of the lower fracture.

(3) The tracer studies indicate that the modal volume (see Sec. 8 and Appendix A) of the middle fracture was larger than the modal volume of the upper fracture during Run Segment 5. Figure 6-5 shows the modal volume V of each of the major flow paths for two of the bromine tracer experiments during Run Segment 5. The occurrence of the maximum modal volume in the middle fracture would be unlikely if the upper fracture were an extension of the middle fracture. However, it is true that the same situation could exist if unusual fluid dynamic considerations resulted in fluid "short-circuiting" from the inlet to the upper fracture outlet.

The gross heterogeneous nature of the reservoir must also be considered. The upper part of the reservoir was repeatedly cooled and pressurized prior to the reservoir enlargement in March 1979. The lower part, which is accessed by connections below the casing, has a different flow history.

The vertical extent and temperatures in the reservoir are best illustrated by the temperature log in Fig. 6-4, which is measured along the intersection of the nearly vertical (within 7°) EE-1 wellbore with the reservoir. The temperatures along the wellbore are depressed an extra 10°C by unrecovered wellbore cooling. The minimum temperature (plus 10°C) in the upper reservoir represents the flow entrances and is lower than the average fracture temperatures. Earlier temperature logs show three main fracture crossings of EE-1 in

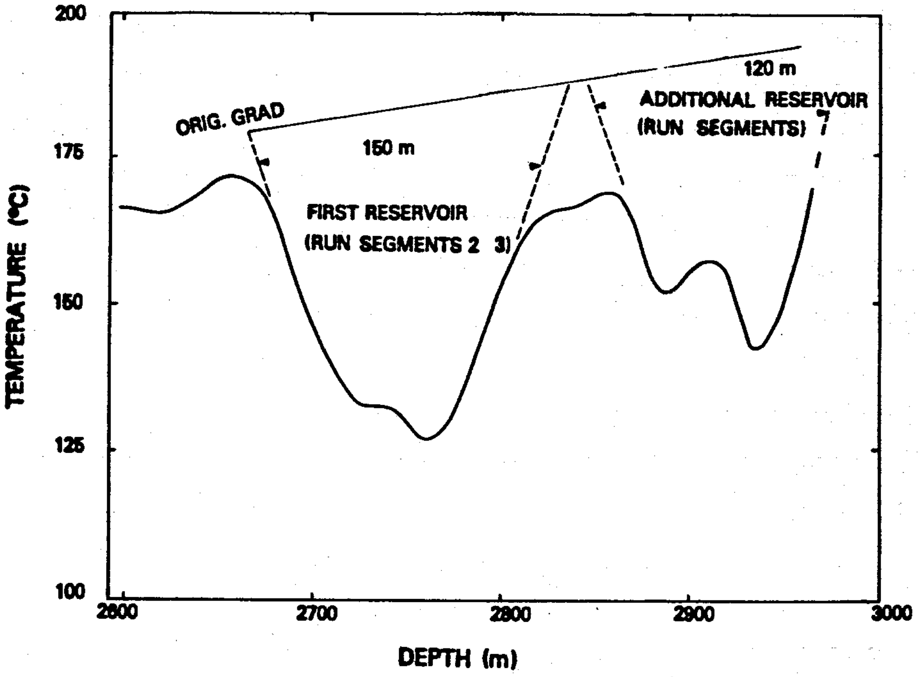

Fig. 6-4.
Temperature log in EE-1 wellbore showing temperature field caused by previous run segments.

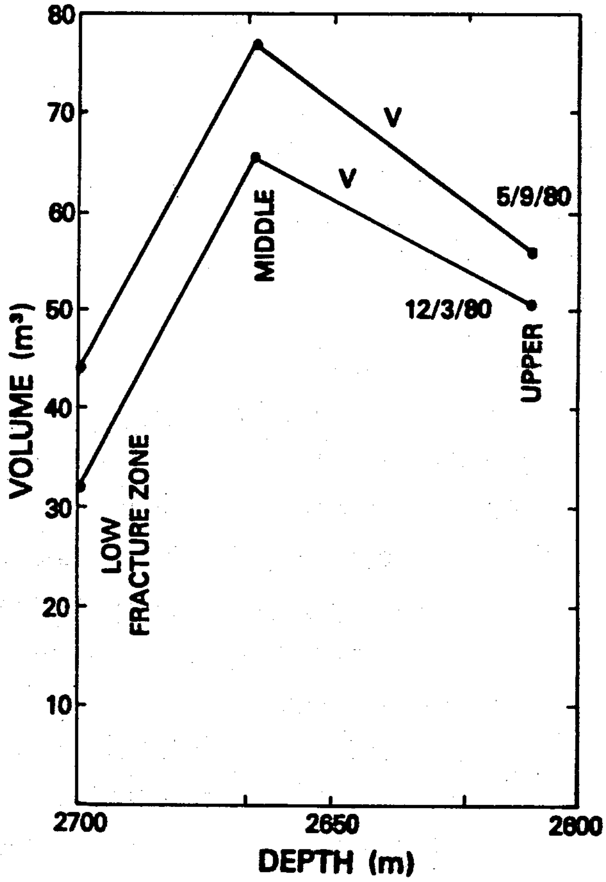

Fig. 6-5.
Modal volumes of fracture systems.

the upper reservoir. The temperature depression in the lower part of the reservoir was created mainly by the large flow in Run Segment 4. The extent of this temperature depression indicates that this part of the reservoir consists of either one major flow path that is ∼60 m (180 ft) wide, which crosses the wellbore twice, or of two narrower flow paths.

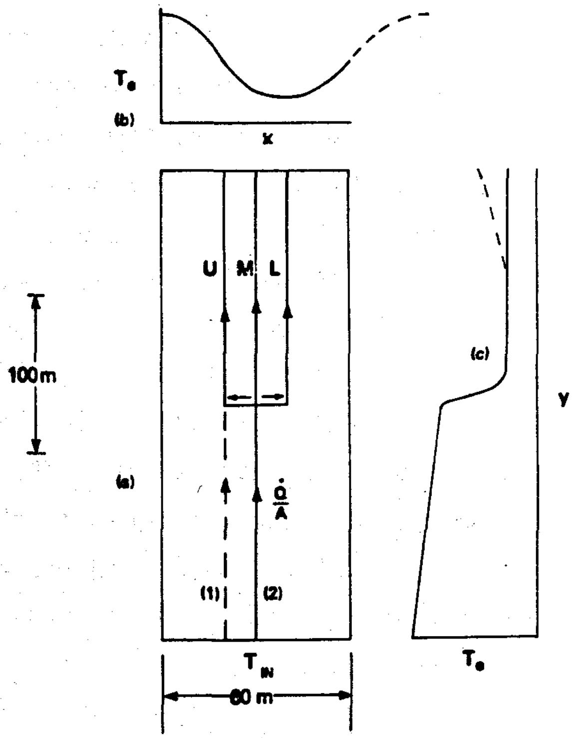

Fig. 6-6.
Simplified model for multiple fractures heat-transfer calculations.

The foregoing considerations suggest a simple two-dimensional heat transfer model with lumped parameters (Fig. 6-6). The grid, shown in Fig. 6-6(a) consists of a multiple-fracture system embedded in a two-dimensional rock matrix. Three-dimensional heat-conduction effects are ignored. A specific flow rate ($\dot{Q}/A$) is programmed into each branch of the fracture. Because the flow rate ($\dot{Q}$) is known, this is a specification of the area (A) of each branch. At the midpoint of the reservoir, a small transverse region connects the upper and lower systems. The lower system has one or two fractures; the upper system has three. Each problem in the parameter study runs from the beginning of Run Segment 4 through the end of Run Segment 5. This was done because the changes for each run should be applicable to both experiments. The initial temperature field was determined by the depletion of the reservoir in Run Segments 2 and 3. Because the vertical gradients in each fracture of the upper reservoir were unknown, no attempt was made to include them. The transverse temperature profile (x direction in Fig. 6-6) was Gaussian with a minimum width determined by the recovery time since Run Segment 2 and a maximum width determined by the total energy removed in Run Segments 2 and 3. Because the temperatures in the lower part of the reservoir are determined by Run Segment 4, they were initially set to the measured original geothermal gradient temperature. A typical transverse profile is shown in Fig. 6-6(b). A typical vertical profile is shown in Fig. 6-6(c).

The adjustable parameters are considered to be (a) the area of each branch of the fracture system and (b) the average starting temperature of each fracture in the upper system, which is determined by the exact position in the grid. Because the actual starting temperature of each fracture is determined by its entire flow history and proximity to other fractures, it would be difficult to obtain an accurate value to insert in the model.

The time-dependent flow programmed into the calculations was approximated by the dashed lines in Fig. 6-2. The total flow is maintained in the upper and lower reservoirs. In the upper part the flow is divided between the three major flow paths as indicated. One multiple-fracture model has the flow divided between two fractures in the lower half. The flow split is adjusted in the calculations as an additional parameter. The second model has only one fracture in the lower half of the reservoir but maintains three fractures in the upper portion.

Figures 6-7 and 6-8 are the best fits to the temperature data obtained thus far. Table 6-I summarizes the areas used in each model. Model A (Fig. 6-7) has two fractures in the lower reservoir, whereas Model B (Fig. 6-8) has only one. The best estimate of the total heat-exchange area at the end of Run Segment 5 is 45 000 m^2, with 30 000 m^3 residing in the portion of the reservoir cooled by the Run Segments 2 and 3 flows.

TABLE 6-I

SUMMARY OF HEAT-EXCHANGE AREAS FOR RUN SEGMENT 5 AREAS
(m^2)

Reservoir	Fracture	Model A	Model B
Upper	Upper	7 500	7 500
	Main	15 000	15 000
	Lower	7 500	7 500
Lower	Two fractures	15 000	
	One fracture		7 500
Total Areas		45 000	37 500

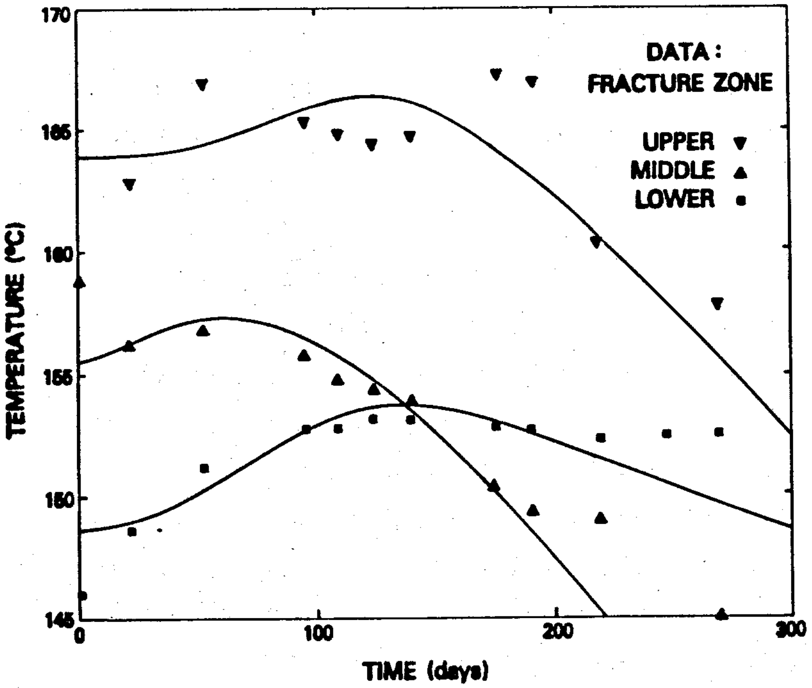

Fig. 6-7.
Computer model comparison with field data for multiple-fracture model having two lower fractures.

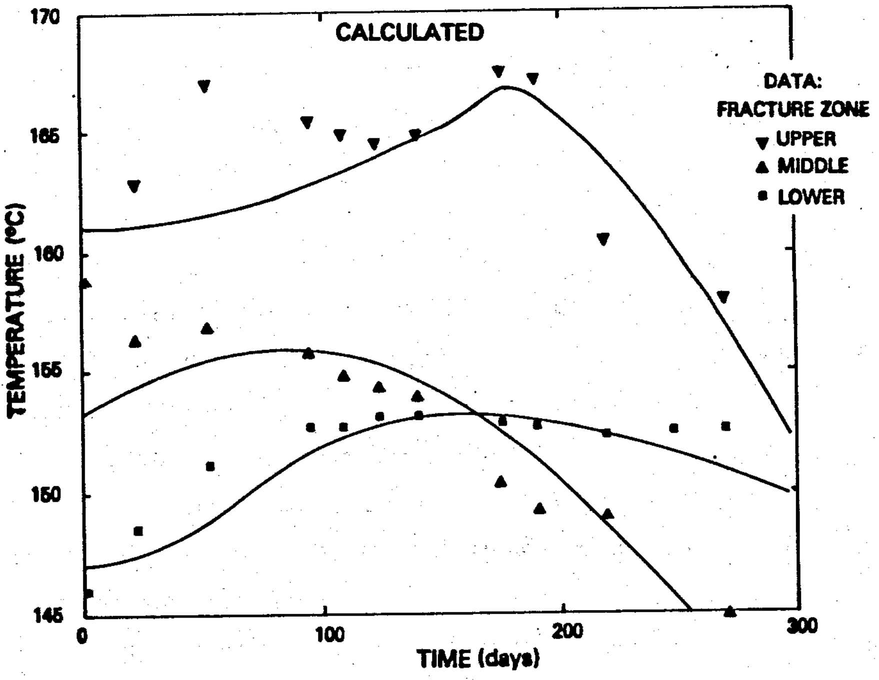

Fig. 6-8.
Computer model comparison with field data for multiple-fracture model with a single lower fracture.

6.3. Independent-Fractures Model

Despite the evidence cited above in support of a multiple-fracture model, with thermal interaction between fractures, the data were also analyzed with a model that treats the reservoir as two independent fractures. Independent means that the two fractures are far enough apart that the regions of thermal decline around each fracture did not overlap. Thus each fracture could be treated as an independent fracture embedded in an infinite rock mass, hence the name independent-fractures model (occasionally referred to as the "single" fracture model). This simplified model was considered in addition to the multiple, interacting-fractures model described in the previous section, because: (1) It continues an historical trend. In the past, the old reservoir data were fitted rather well with the independent-fractures model. By continuing use of this model for the new reservoir, the effects of gross changes in reservoir size are easily derived and readily presented and compared. (2) The independent-fracture model is considerably simpler. Although it fails to predict in detail some aspects of reservoir behavior, it predicts rather well the overall thermal drawdown of the reservoir. Because of its simplicity, it is a convenient means of describing the reservoir and allows convenient prediction of future behavior.

Description and Genesis of the Model. The model and its application to HDR geothermal reservoirs are described in detail in Refs. 4, 14, and 15. The model is based upon previous work by Harlow.[16] Because of these previous presentations, only a brief, nonmathematical description is needed here. The model numerically solves five coupled partial differential equations. The first three equations describe the fluid dynamics within a fracture. Two-dimensional flow parallel to the fracture plane is considered, and the equations of conservation of mass and conservation of momentum are satisfied. The fluid dynamic equations allow dependence of water properties, particularly viscosity, upon temperature and pressure. Advection, viscous drag, and buoyancy terms[14] are included in the momentum equations. The remaining two equations account for conservation of energy in both the water and the surrounding rock. The rock is assumed impermeable so that the water is confined to the fractures, and consequently, a small error is introduced because of the downhole water losses. The energy equations incorporate convection, conduction, and transient heat storage terms.[14] Because heat conduction within the rock is primarily orthogonal to the fracture plane, only one-dimensional conduction need be considered. (Consequently, although the physical situation being modeled appears three dimensional, the numerics need consider at most two-dimensional equations.) Based upon in situ measurements,[17] the thermal conductivity of the rock was taken as 2.9 $Wm^{-1}K^{-1}$. Water properties were taken from steam table compilations.

This model permits any shape of fracture. However, the granitic rock in which these fractures were created is fairly homogeneous and unstratified with respect to its mechanical properties; thus, all the fractures discussed here are assumed to be approximately circular in shape, rather than rectangular as is usually assumed for oil and gas reservoirs in sedimentary formations,[18-20] as well as the multiple-fracture model of the previous section. It was also assumed that the fractures are nearly vertical because the planes of hydraulic fractures are orthogonal to the minimum (least-compressive) component of the tectonic earth stress. In tectonically relaxed geological settings, this stress is expected to be a horizontal one at depths greater than about 1 km. The minimum compressive horizontal tectonic stress at the reservoir depth is 37 MPa (5400 psi), about one-half the vertical overburden stress, as estimated by pressurization tests.[2]

For both reservoirs tested to date, the manner in which the major vertical fractures are connected with the production well, GT-2B, is complex as illustrated by a number of measurements including downhole temperature and flow rate (spinner) surveys, radioactive tracer logs, caliper logs, and televiewer surveys. Major connections apparently consist of a set of natural fractures or joints with a dip of approximately 60° from the vertical, which intersect both vertical hydraulic fractures and the GT-2B wellbore as shown in Fig. 3-1. In the independent-fractures model described here, explicit modeling of these slanting joints was not attempted as this would have required a fully three-dimensional simulation, for which the computing expenses were not justified considering the geometric uncertainties. Instead, the heat-transfer area associated with the joints, expected to be small, was simply absorbed into the main hydraulic fractures, and the total area was sought in terms of vertical circular fractures. However, the effects of the joints did have to be considered in terms of their influence on flow patterns; for example, a joint providing a fracture flow outlet very close to the inlet could result in short circuiting in which most of the injected flow could follow the shortest path to this outlet, thus bypassing the majority of the area potentially available for heat extraction. To account for these effects, models with multiple flow outlets were considered. As mentioned above, when more than one fracture had to be considered, as was the case for the latest reservoir (see Fig. 3-1), it was assumed that the fractures were far enough apart that no thermal interaction occurred. The required lateral separation distance to avoid thermal interaction is $3\sqrt{\kappa t}$, where κ is the thermal diffusivity of the rock, $10^{-6} m^2/s$, and t is time. For Run Segment 5 this distance is 15 m (50 ft), so that the assumption implicit in this modeling is that the main hydraulic fractures are at least 15 m apart. In contrast, the multiple-fracture model of the previous section allowed thermal interactions, and in fact fractures as close as 5 m were considered. In principle, thermal interactions could also be incorporated in the independent-fractures model, but this would require a truly three-dimensional computer program, an expense that once again was not considered justifiable in view of other uncertainties.

The first application of the independent-fractures model was to the first reservoir, when only the smaller hydraulic fracture shown to the right in Fig. 3-1 existed. This reservoir was tested extensively during Run Segment 2, occasionally referred to as the 75-day test, and described in Ref. 3. Based upon spinner and temperature surveys in the production well, the depths of the intersection of the production well with the slanting joints were estimated as well as the flow rates communicated by each joint. In the calculations, the actual temporal variations of production and injection flow rates were used. The fracture inlet temperature was estimated with a separate wellbore heat transmission calculation.[13] With this information, estimates of the thermal drawdown were calculated with the model for various trial values of fracture radii and vertical position of the fracture inlet. It could not be assumed that the inlet was located at the center of the fracture because the earth stresses increase with depth, so that during its creation the fracture probably grew preferentially in the upward direction. A fracture radius of 60 m with an inlet located 25 m above the fracture bottom resulted in a good fit to the measurements, and, as shown in Fig. 6-9, the computed thermal behavior was in good agreement with the measured temperature. The temperature shown is the mixed mean reservoir-outlet temperature. That is, the mean outlet temperature is taken as the mean of the joint-outlet temperatures measured in the production well, averaged, or weighted, by the flow rate fraction in each joint. This mean outlet-temperature measurement is considered the best

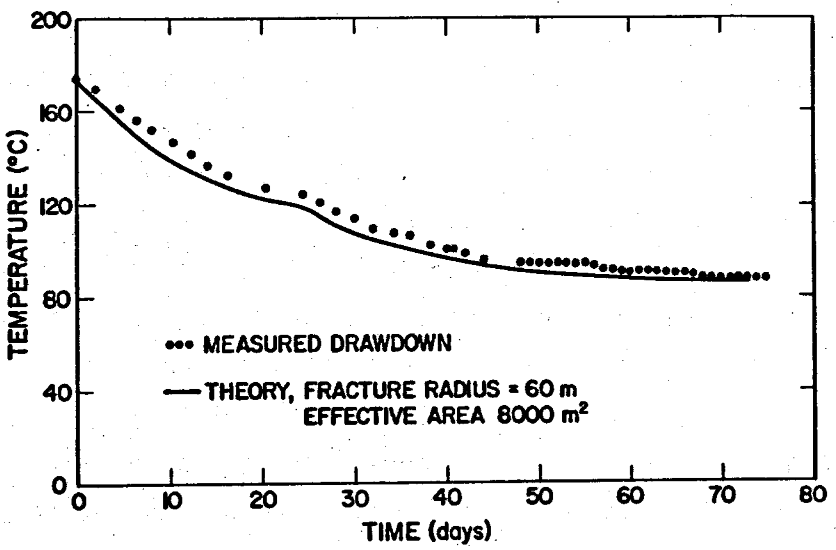

Fig. 6-9.
Computer model comparison with field data for multiple-fracture model with a single lower fracture.

measure of the overall thermal performance of the reservoir and is used here to describe not only the old reservoir, but also below, the enlarged, two-fracture reservoir. A radius of 60 m implies a total fracture area (on one side) of 11 000 m^2; however, because of hydrodynamic flow sweep inefficiencies, the net area effective in heat exchange was only 8000 m^2 during Run Segment 2.

Six months after the conclusion of Run Segment 2, Run Segment 3 (the so-called high back-pressure experiment) was conducted in October of 1978. The purpose was to examine reservoir behavior under conditions of high mean-fracture pressure. The test duration was short, less than 1 month, but the thermal drawdown suggested that, according to the independent-fractures model, the effective heat area was about 25% greater during this run. This increase was attributed, at the time, to high pressure, resulting in greater hydrodynamic sweep efficiencies because of the reduced fracture flow impedance.

As described in Sec. 1, the reservoir was enlarged during the fracturing operations of 1979. For the independent-fractures model the enlarged reservoir is portrayed as two fractures, the old one operative in Run Segments 2 and 3, and a new and larger one shown to the left in Fig. 3-1. The enlarged reservoir was evaluated during Run Segment 4[8] and Run Segment 5. The details of the independent-fractures modeling of the new reservoir were described in Ref. 15. To summarize the Run Segment 4 studies, it was found that the old fracture had an effective heat-transfer area of 15 000 m^2, and the new fracture had an effective area of at least 30 000 m^2. We say "at least" because the heat-extraction period was only 23 days, far too short to result in significant depletion of the new fracture. The area determined in Run Segment 4 for the old fracture was at least twice that determined in Run Segment 2. This trend of increasing area, as observed in both Run Segments 3 and 4, is now attributed to thermal stress cracking effects[16,21] because, during Run Segment 4, the operating pressure conditions were similar to those of Run Segment 2, so that the augmented heat transfer cannot be due to pressure alone.

Better estimates of the total effective heat-transfer area of both fractures were obtained in Run Segment 5, during which the thermal drawdown, that is, the decline in temperature, of the mean reservoir-outlet temperature, attained 8°C. This drawdown and the model predictions for several values of the combined areas are shown in Fig. 6-10. The data ranges shown should not be interpreted as error bars. Instead, the ranges merely reflect the differences that occur if the thermal decline is measured with respect to the initial mean reservoir-outlet temperature or, instead, with respect to the highest mean outlet temperature observed. The mean outlet temperature actually increased slightly during the early portion of Run Segment 5, as shown in Fig. 6-3 by the curve labeled "total flow." This temporary increase is due to transport of deeper, hotter, water to the production well as well as to some interaction of the fractures. For simplicity the effect was neglected in the independent-fractures model as it is fairly small, less than 2°C. As shown in Fig. 6-10, the data are fit very well by a model with a combined area of 50 000 m^2, some 5000 m^2 greater than the area tentatively estimated from the very small drawdown during Run Segment 4.

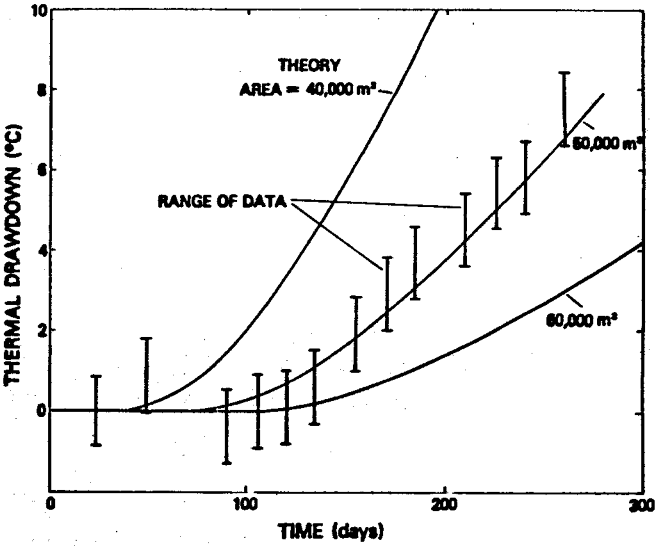

Fig. 6-10.
Computer model comparison with field data with independent-fracture model for Run Segment 5.

6.4. Comparison of the Models

The results of the independent-fractures model are compared with the best estimates of the multiple interacting-fractures model (model A) in Table 6-II below. For the multiple-fracture model, it was concluded that the old reservoir originally consisted of three fractures; and because of pressurization and thermal stress effects, the net area grew from 8000 m^2 to 30 000 m^2, still maintaining three fractures. In contrast, the independent-fractures model concludes that the growth of this original fracture was caused primarily by thermal stress cracking and that the latest area is 15 000 m^2, not 30 000 m^2. Furthermore, for simplicity, the independent-fractures model assumes that the old fracture can still be represented as a single fracture rather than three fractures. The multiple-fracture model assumes that the reservoir enlargement caused by hydraulic fracturing in 1979 resulted in two additional fractures, each with an area of 7500 m^2. In contrast, the independent-fracture model assumes that the enlargement resulted in a single additional fracture with an area of 35 000 m^2.

If attention is focused on the combined areas, we see very good agreement, 45 000 m^2 for the multiple-fracture model and 50 000 m^2 for the independent-fractures model. However, this agreement does not translate to equally good agreement of heat-extraction characteristics. If heat extraction

TABLE 6-II

COMPARISON OF HEAT-TRANSFER MODEL RESULTS

	Multiple-Fractures Model (Model A)	Independent-Fractures Model
Old Reservoir (Run Segments 2 and 3)	Three fractures, sum of areas = 30 000 m^2	One fracture, area = 15 000 m^2
Additional Reservoir due to enlargement (Run Segments 4 and 5)	Two new fractures, each area = 7500 m^2, sum = 15 000 m	One new fracture, area = 35 000 m^2
Total fracture area	45 000 m^2	50 000 m^2

had been prolonged for several more months during Run Segment 5, the multiple-fracture model with constant fracture area would have predicted a more rapid rate of drawdown because of the continuously increasing overlapping of thermal depletion regions.* This overlapping and interaction effect is missing in the independent-fractures model so the predicted rate of drawdown would have been somewhat slower. Even with this caveat, however, the agreement of the two models is quite good when one considers the great disparity of geometrical assumptions inherent in each model. Both models use two-dimensional simulators in which heat is transported by conduction within the rock to the fractures, but the similarity ends there. The multiple-fracture model assumes that the fractures are rectangles and that flow is distributed uniformly along the bottom of each fracture and uniformly withdrawn from the top of each fracture. The flow is thus one-dimensional and the streamlines are straight vertical lines. Consequently fluid dynamic considerations do not enter into the heat-extraction process -- the sweep efficiency is implicitly assumed to be 100%. However, a rigorous two-dimensional heat-conduction solution is incorporated for the rock between the fractures, and this permits valid consideration of thermal interaction effects. In contrast, the independent-fractures model assumes that the fractures are circular (but other assumptions are permissible) and allows proper local positioning of the inlet and outlets, that is, the point-like intersection of the injection well with the fracture can be modeled, as can the intersection of the main hydraulic fractures and the slanting joints that provide the multiple outlets. (However, as was cautioned earlier, whereas the fluid dynamic effects of the joints/outlets can be faithfully modeled, the heat-transfer effect of the joints cannot -- the area of the joints must be lumped with the main fractures.) In view of this more faithful representation of inlet and outlets, and the fact that a complete two-dimensional solution to the Navier-Stokes fluid dynamic equations is incorporated, the independent-fractures model results in a more realistic assessment of the effect of fluid dynamics and sweep efficiencies upon heat extraction. The penalty, however, is that in the present two-dimensional

---

* There is evidence, however, that the fractures are growing during thermal depletion, and accounting for this fact would alter the rapid drawdown of the multiple-fracture model.

version of the code, thermal interaction cannot be accurately and realistically represented.

In summary, the heat-extraction modeling was approached from two directions, each using different sets of assumptions. Although both models are now only two-dimensional, both models predict reasonably well the overall drawdown of the present reservoir. This agreement gives pause to the development of more complicated and expensive three-dimensional models, but it appears that this development may be required for future reservoirs.

6.5. Comparison of Reservoir Geometry Determined by Heat Transfer-Modeling with Geometry Determined by Microseismicity

As mentioned previously, near the end of Run Segment 5 a separate experiment, the SUE was conducted.[10] The objective was to achieve partial relaxation of the thermal stresses and strains induced by the 15 million kilowatt hours of heat produced in Run Segment 5 prior to SUE. The means of achieving the partial release was to inject water at high flow rates, about 0.04 m^3/s (700 gpm) into both wells until the reservoir pressure exceeded the earth confining stress that opposes opening of the fractures. This was accomplished in 8 h of pumping. By completing the pressurization in such a rapid manner, it was hoped that diffusional spreading of the injected water would be minimized, so that acoustic signals would result from thermal stress relaxation and redistribution, not from additional rock failure induced by conventional hydraulic fracturing. By this means, only the thermally stressed, and consequently, thermally affected region of the reservoir would be seismically activated, and one would then have an independent method of defining that region of the reservoir effective in heat production. There will be more discussion on this point below.

In the remainder of this subsection, we discuss only the microseismic results of SUE because these bear directly upon heat extraction. Section 9 of this report discusses more generally the seismic monitoring conducted during all of Run Segment 5. Seismic signals were detected with two downhole geophone packages. Each package consisted of 12 geophones, 4 each in three orthogonal directions. One package was located at a true vertical depth of 2.70 km (8850 ft) in GT-2B, the production well, whereas the other was located at 2.92 km (9570 ft) in EE-2. Well EE-2 was recently drilled for the future Phase II reservoir and served merely as a monitoring well during this experiment. Because of their downhole locations, both packages were well within a kilometer of all the detected events. As a consequence of this proximity and the excellent detection characteristics of the geophones, microearthquakes with local magnitudes as low as -6 could be detected.

Before presenting the SUE microseismic results, we must first briefly discuss the complex relation between microseismicity, pressurization, and thermal stresses. It is believed that most of the thermal contraction strain during Run Segment 5 was "locked in" by frictional forces on the fracture faces (downhole operating pressures were well below the confining earth stress on average). This belief is supported by observations from tracer studies, reported in Sec. 8.1, that the measured volume increase of the reservoir was only 10% of that expected on the basis of free thermal contraction. Consequently, these frictional forces had to be relieved by pressurization in excess of the local earth confining stress to "unlock" the thermal contraction. Unfortunately, such pressurization results in microseismicity on its own account, as has been shown during many past experiments as discussed below. The question then is, How can one distinguish microseismicity caused by pressurization alone from that caused by thermal stresses abetted by pressurization? At the present time there appears to be no clear cut answer; certainly there does not seem to be any distinguishing characteristics in the microseismic signals themselves. However, a partial and qualitative picture can be assembled by examining maps of the microseismic event locations from past experiments and comparing these with the SUE locations. A summary of this information is provided in Table 6-III. For each recent experiment in which microseismicity was measured, we have tabulated the total injection volume and injection rate, the maximum wellhead pressures, and the diameter of microseismic activity. This diameter is not meant to imply that the microseismic events define circular fractures, but is merely the length of the chord that passes through the bulk of the locations in a given experiment. In reviewing the operating conditions of Table 6-III, it can be seen that, although there are small variations of injection flow rate and pressures of the order of ±50% about the mean, the major difference occurs with injection volume. These injection volumes vary by nearly a factor of 10, from 600 m^3 to 5000 m^3, so as a first approximation, one would seek a correlation between the microseismic activity diameter and the injection volume. For the first three experiments, in which heat extraction and thermal contraction were insignificant (Expts. 203 and 195 lasted 1 day; microseismicity during Run Segment 4

TABLE 6-III

SUMMARY OF MICROSEISMIC EXPERIMENTS

Experiment	Date	Injection Volume (m^3)	Max. Injec. Rate (m^3/s)	Max. Inj. & Prod. Well Pressures (MPa)	Diameter of Microseismic Activity (m)
203	10/14/79	603	0.032	19.5/5.5	580
195	3/21/79	755	0.051	10.7/10.3	650
Run Seg. 4	10/30/79	5 000	0.025	17.0/10.0	920
SUE	12/8/80	1 000	0.040	15.5/13.0	250

was measured only 7 days from the start of heat extraction), it can be noted that the microseismic diameter indeed correlates with injection volume. Admittedly the variation is not a strong one — the diameter ranges only from about 600 m to 900 m despite a nearly 10-fold increase of injection volume. However, the SUE microseismicity, following 280 days of heat extraction during Run Segment 5, is significantly different. The microseismic diameter is only 250 m, less than half the diameter measured during Expts. 203 and 195, despite the fact that the SUE injection volume was actually larger than either Expt. 203 or 195. No doubt water was injected during SUE just as far away from the injection well as it was during Expts. 203 and 195, but the microseismic activity in the regions unaffected by thermal drawdown was dimminished by the repeated injections prior to and including SUE. In other words, these regions were becoming aseismic to pressure disturbance. The SUE microseismicity is thus thought to be predominantly due to the released thermal stresses, and on this basis it may tentatively be concluded that the microseismic activity during SUE focussed on thermal effects. However, we cannot exclude the possibility that some events due primarily to pressure are still included in the population. Indeed, as will be seen, the comparison with heat transfer-inferred geometries suggests that remaining pressure effects do distort the microseismic geometry somewhat. This distortion is unavoidable, even for reservoirs in nearly impervious rock. Because of the presence of natural joints, both filled and unfilled, and the finite, albeit low, permeability of the rock fabric, there will always be water losses to the rock surrounding the fracture system. Consequently, pressurization and microseismicity can occur not only in regions of the fracture not usually available for heat transfer in the continuous circulation flow-through mode, but many of the events also stem from locations large distances away from, and orthogonal to, the fractures. Some indication of the extent of this lateral water diffusion can be noted that the modal volume (Ref. 10) of the fracture just prior to SUE was 185 m^3. This represents the self-propped volume, that is, the volume at operating pressures below that required to open the fracture against the local earth stress. After inflation the fracture would be expected to have a volume several times larger, say 400 to 800 m^3; nevertheless, this inflated volume is still less than some of the injection volumes of Table 6-III, indicating that some water does indeed diffuse away from the fractures.

Figures 6-11 and 6-12 compare the locations of the microseismic events of SUE with the heat transfer geometries discussed earlier. Figure 6-11 is a plan view, that is, the reader is looking vertically down; whereas Fig. 6-12 is an elevation view in which the reader is looking horizontally, in approximately an east-west direction, perpendicular to the planes indicated in Fig. 6-11. In Fig. 6-11, the plan view, the three upper fractures of the multiple fracture model and the two fractures of the independent fracture models are shown as lines. From Figs. 6-11 and 6-12 it can be seen that from one fracture extremity to the other the seismic activity takes place within a separation distance of about 250 m. As discussed above, this is in sharp contrast to the microseismic results of Run Segment 4 (Ref. 8), in which the microseismic diameter was over 900 m.

Referring now to the elevation view, Fig. 6-12, it is seen that if a circle is drawn around all the microseismic events, this circle has a radius of about 140 m and an area of about 60,000 m^2. In comparison the largest of the parallel circular fractures of the independent fractures model has an area of 35,000 m^2 per Table 6-III. The multiple fractures model consisted of five fractures, three in the upper reservoir and two below. In the elevation view of Fig. 6-12 one would see one of each, and because the upper and lower fractures are connected in this model, one would see one long rectangle about 50 m wide and 300 m long in the vertical direction, a total area of about 15 000 m^2. In summary the microseismic area from SUE is still considerably greater than the appropriate heat transfer area, by a factor of 2 for the independent fractures model and by a factor of 4 for the multiple fracture model. As

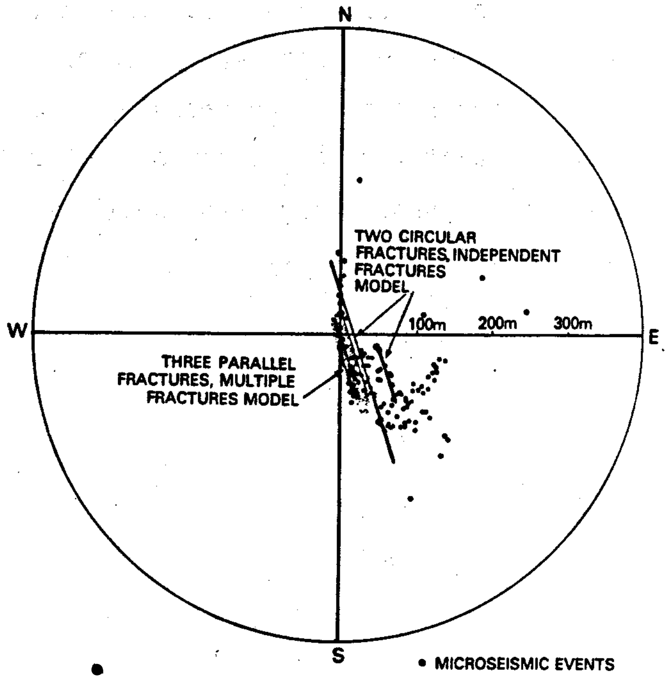

Fig. 6-11.
Plan view comparing microseismic event locations with heat-transfer model geometries.

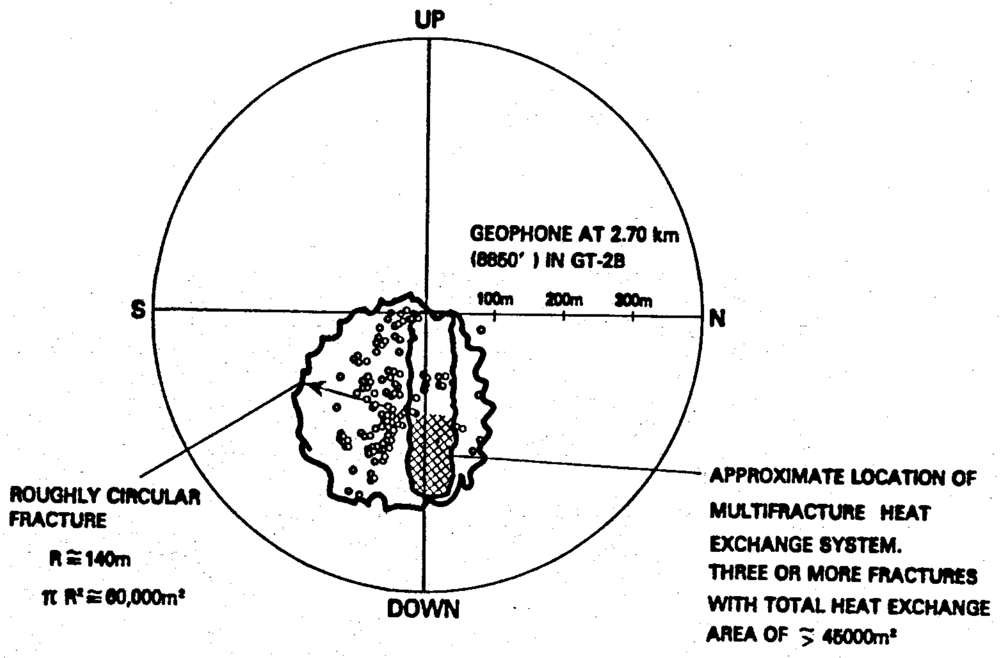

Fig. 6-12.
Elevation view (looking approximately from east to west) comparing microseismic event locations with heat-transfer model geometries.

explanation for these discrepancies, we suggest the strong possibility that the SUE microseismic events were not completely confined to the thermally affected region, as discussed earlier. Nevertheless, despite these numerical discrepancies, the rough qualitative agreement of the microseismic and heat transfer model geometries is encouraging when the sharp differences in approach of the two methods are considered.

7. GEOCHEMISTRY

Samples of the geothermal fluid were collected at regular intervals, typically every day, from the GT-2B wellhead, the EE-1 wellhead, and at the make-up pump, which provided the water from reserve pits to replace the downhole water loss. Samples of the dissolved gases were collected at less frequent intervals. The gas samples included both noncondensible gas samples and samples for radon analysis. Fluid samples were analyzed for pH, Eh (oxidation-reduction potential), conductivity, SiO_2, Na^+, K^+, Li^+, Ca^{++}, Mg^{++}, Sr^{++}, Mn^{++}, $Fe^{+2 \text{ and } +3}$, B, $SO_4^=$, Cl^-, HCO_3^-, F^-, and total suspended solids (TSS). Dissolved noncondensible gas samples were analyzed for H_2, N_2, O_2, CO_2, and H_2S. Details of the sampling and analytical procedures for the fluid and gas samples are provided in Appendix B.

7.1. Variation in Concentrations with Time

Typical results of the fluid analyses from the GT-2B wellhead are presented in Table 7-I. Gas and radon analyses are in Table 7-II. The results from these tables are plotted vs time for several major elements in Figs. 7-1 through 7-7. As was observed in the closed-loop portion of the Run Segment 4 test,[8] steady-state levels of species concentrations were established rapidly. During Run Segment 5, however, a gradual decline in dissolved species concentration started at about day 100.

There are several very sharp perturbations on the graphs in Figs. 7-1 through 7-5 at days 102-110 and 230-234. These periods show the chemical response of the reservoir to a step change in inlet fluid composition. This change was produced when the operational mode was switched from closed-loop with about 7 to 10% make-up to fully open-loop. This type of perturbation experiment is termed "fresh-water flush" (FWF). Descriptions of the FWF episodes are presented later in this section.

Noncondensible gas and radon analyses are shown in Figs. 7-6 and 7-7. The predominant noncondensible gases are CO_2, N_2, and O_2. Minor concentrations of H_2 and H_2S were also observed. As in Run Segment 4, CO_2 is highly enriched while O_2 is depleted relative to N_2. However, the much higher CO_2 fraction in Run Segment 5 ($\sim$78%) than in Run Segment 4 ($\sim$55%) was due to dilution effects in Run Segment 4. The radon analyses (Fig. 7-7) showed a gradual increase to a steady-state value of 9 to 10% nCi/ℓ.

TABLE 7-I

SELECTED ANALYSES OF PRODUCED AND MAKE-UP FLUID FROM RUN SEGMENT 5

(Analyses are reported in ppm unless otherwise noted.)

Sample No.	Date	Time	pH	Eh mv	Ca	Mg	Na	K	Cl	SO_4	HCO_3	SiO_2	Fe	Li	Mn	F	B	Conductivity µmho/cm
Produced Fluid																		
G-2	3/10/80	15:00	6.57	284	83	3.0	1490	110	1750	341	538	267	nd	nd	nd	8.7	42.3	7500
G-3	3/11/80	00:30	5.95	336	61	2.3	1110	90	1220	290	513	245	5.55	17.0	0.17	10.6	33.1	5600
G-4	3/11/80	07:00	6.05	333	42	1.6	855	75	921	248	493	232	5.83	14.0	0.15	15.3	25.0	4500
G-8	3/14/80	10:00	6.33	305	26	0.8	750	53	583	227	400	214	1.00	9.5	0.09	16.5	14.5	3100
G-15	3/21/80	10:30	7.33	249	28	0.6	554	48	528	260	471	214	0.64	8.8	0.09	11.2	13.5	2900
G-22	3/28/80	10:30	6.78	290	24	0.5	485	46	422	241	455	209	0.38	7.8	0.07	14.1	12.0	2500
G-29	4/4/80	10:30	7.31	253	25	0.5	470	47	387	222	483	211	0.42	7.6	0.07	14.4	10.9	2400
G-36	4/11/80	14:00	6.15	56	27	0.6	490	48	381	245	477	226	0.44	7.9	0.08	15.8	11.4	2500
G-50	4/25/80	10:00	6.13	34	24	0.5	485	47	412	258	454	227	0.30	7.8	0.07	14.6	11.2	2500
G-63	5/9/80	06:00	6.27	288	25	0.5	475	48	420	256	448	233	0.30	7.8	0.07	13.3	11.2	2500
G-76	5/30/80	10:30	6.14	61	28	0.6	535	48	485	286	450	233	0.39	8.6	0.06	17.0	13.4	2900
G-94	6/20/80	10:00	6.28	17	25	0.6	490	46	380	229	490	228	0.23	7.8	0.06	13.0	11.8	2400
G-104	7/11/80	10:00	6.37	-15	21	0.5	402	39	314	190	471	211	0.20	6.8	0.04	12.6	9.8	2300
G-114	7/25/80	11:10	6.37	4	19	0.5	398	39	351	205	467	225	0.21	7.1	0.04	13.0	10.9	2300
G-175	10/31/80	10:45	6.26	66	19	0.5	360	35	305	180	346	204	0.38	6.0	0.04	17.2	8.7	2000
G-183	11/21/80	11:45	6.26	-39	20	0.5	405	38	302	208	434	199	0.36	6.3	0.04	20.3	0.2	2000
Makeup Fluid																		
M4	3/11/80	07:00	7.67	271	23	3.0	13	3	9	8	79	62	0.22	0.0	0.02	0.7	0.0	205
M36	4/11/80	13:15	7.65	132	38	4.4	13	5	15	8	166	69	0.04	0.0	0.00	0.0	0.0	290
M63	5/9/80	05:45	7.87	265	37	3.7	12	6	15	7	166	72	0.03	0.0	0.00	0.1	0.0	280
M94	6/20/80	09:15	7.44	201	6	2.7	5	1	0	4	50	35	0.10	0.0	0.01	0.1	0.0	76
M114	7/25/80	09:55	7.38	124	7	3.2	4	1	2	2	53	43	0.04	0.0	0.01	0.1	0.0	90
M175	10/31/80	11:20	6.72	220	17	2.0	125	8	130	82	259	108	2.88	2.32	0.11	8.0	3.4	1030
M183	11/21/80	11:00	6.79	43	14	1.7	300	27	228	134	388	144	5.73	4.34	0.16	14.0	6.7	1650

TABLE 7-II

ANALYSES OF NONCONDENSIBLE GAS AND RADON SAMPLES

(Compositions are reported as % or ppm in the noncondensible gas phase)

Sample No.	Date	Time	CO_2 (%)	O_2 (%)	N_2 (%)	H_2 (%)	H_2S (ppm)	Rn (nCi/ℓ)
G4	3/11/80	10:00	80.9	15.7	2.6	0.8	145	4.7
G8	3/14/80	10:30	71.4	2.3	25.9	0.4	350	3.6
G15	3/21/80	11:30	78.0	0.7	20.8	0.1	265	7.2
G22	3/20/80	13:00	77.2	0.9	21.9	--[a]	360	nd[b]
G29	4/4/80	14:30	78.4	0.7	20.9	--	660	9.5
G35	4/10/80	10:30	73.5	1.5	24.8	0.2	660	9.6
G50	4/25/80	13:15	74.4	1.3	24.2	0.1	350	8.0
G62	5/8/80	20:00	75.6	1.2	21.3	1.9	nd	8.8
G76	5/30/80	11:30	78.6	0.8	20.6	--	850	9.3
G93	6/19/80	11:30	78.4	0.8	20.8	--	820	9.8
G104	7/11/80	04:00	73.1	1.7	25.2	--	725	10.1
G114	7/25/80	12:55	76.0	0.3	23.7	--	1050	10.2
G187	12/4/80	11:00	nd	nd	nd	nd	nd	8.4
G187	12/4/80	11:00	nd	nd	nd	nd	nd	9.2

---

[a] -- indicates below detection limit.
[b] nd indicates not determined.

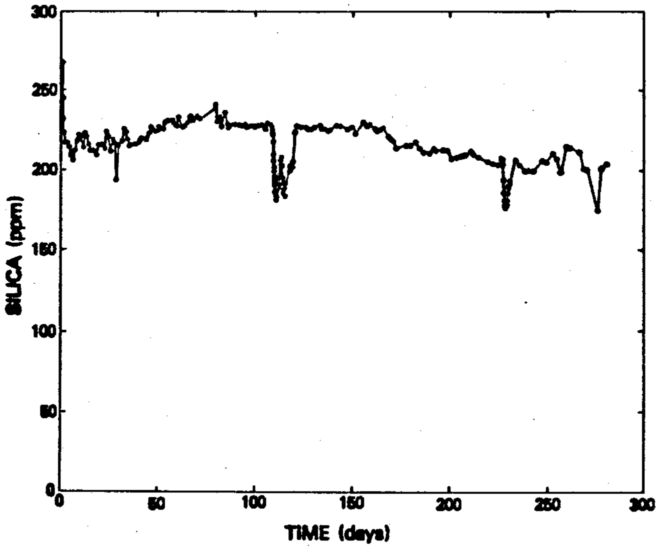

Fig. 7-1.
Variation of silica concentration with time.

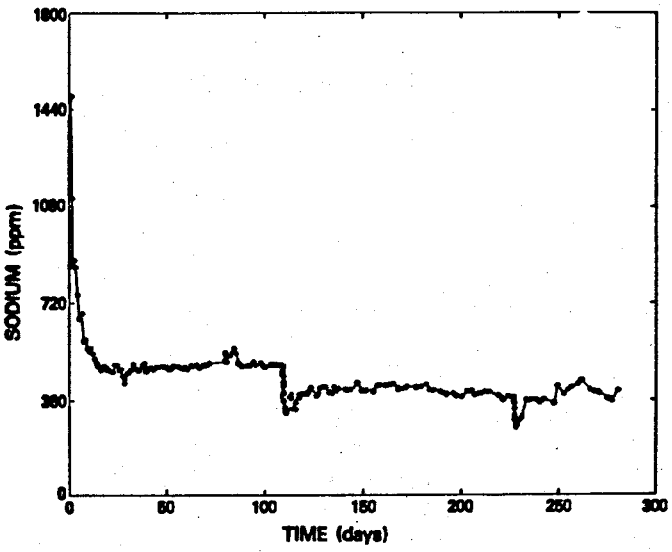

Fig. 7-2.
Variation of sodium concentration with time.

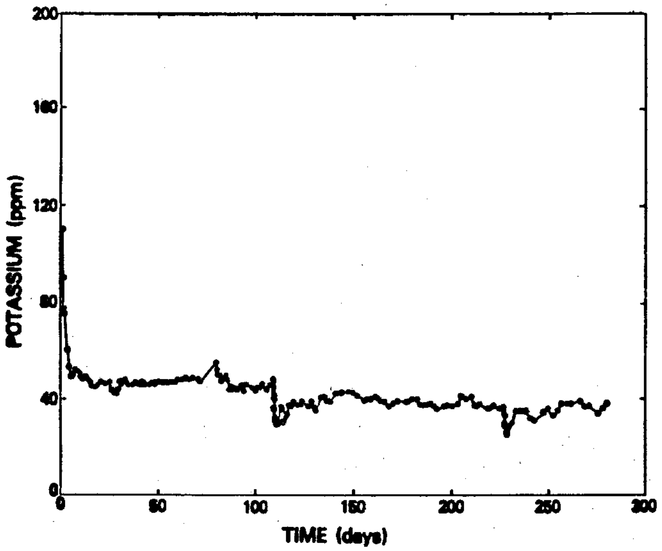

Fig. 7-3.
Variation of potassium concentration with time.

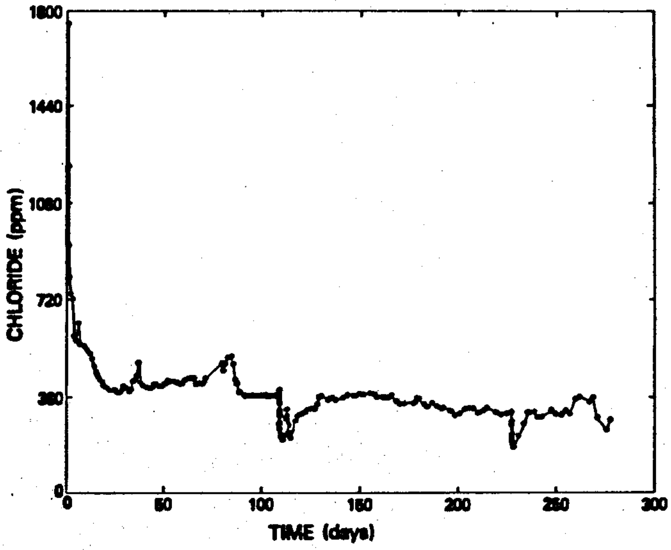

Fig. 7-4.
Variation of chloride concentration with time.

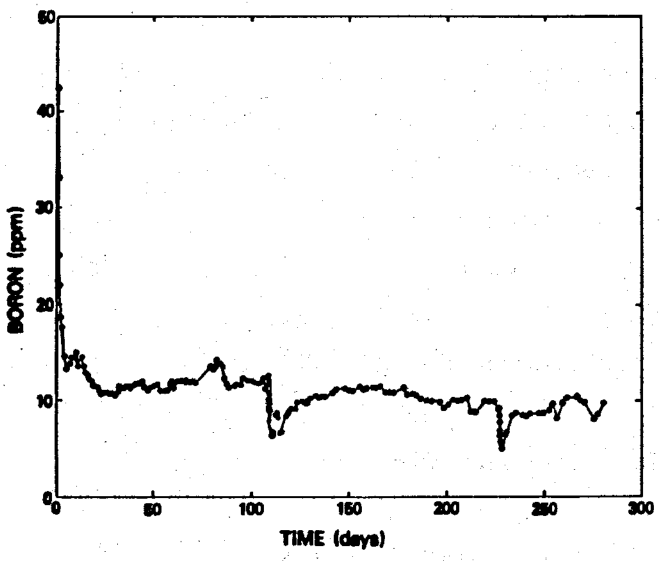

Fig. 7-5.
Variation of boron concentration with time.

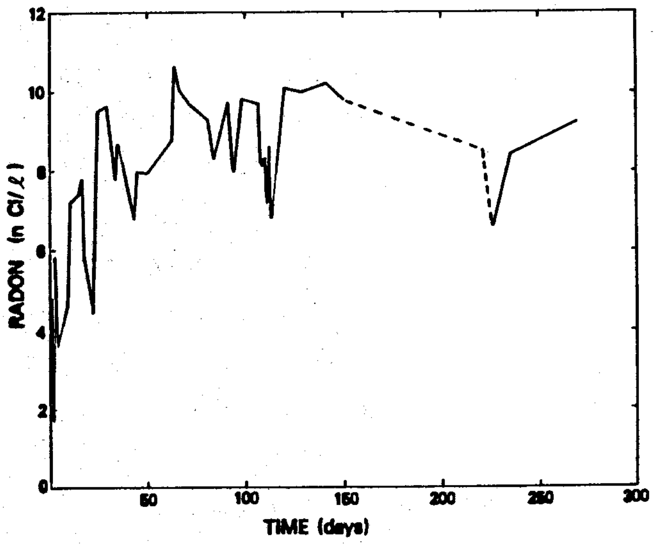

Fig. 7-7.
Variation of radon activity with time.

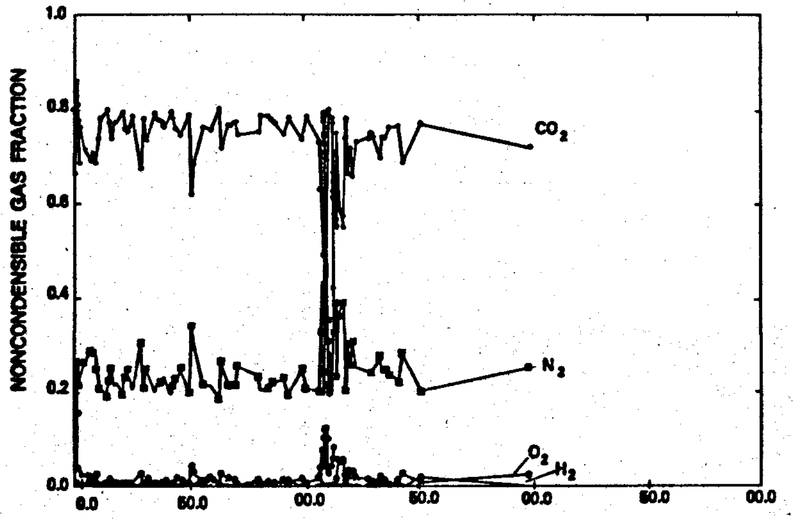

Fig. 7-6.
Variation of noncondensible gas fraction with time.

7.2. Geochemical Behavior of the Reservoir

Arguments based on the constant ratios among soluble ions for the previous (Run Segment 4) test were used to infer the presence of an indigenous fluid within the connected pores and microfractures in the granodiorite reservoir rock. This fluid, called pore fluid, has been in intimate contact with the reservoir rock for a very long time; hence, the ratios among cations such as Na, K, Ca are fixed by equilibrium with reservoir minerals even though the absolute concentrations of these species far exceed the solubilities of the reservoir minerals. This pore fluid is slowly displaced by fresh water, and under conditions of long-term recirculation, the pore fluid would eventually be replaced by fresh water.

The degree to which the ratios among the dissolved species Na^+, K^+, Cl^-, and B are constant is shown in Fig. 7-8 where the nondimensional concentrations for these species are plotted vs time. The nondimensional concentration $\langle C \rangle$ is defined as

$$\langle C \rangle \equiv \frac{C^\infty - C(t)}{C^\infty - C_m} , \qquad (6)$$

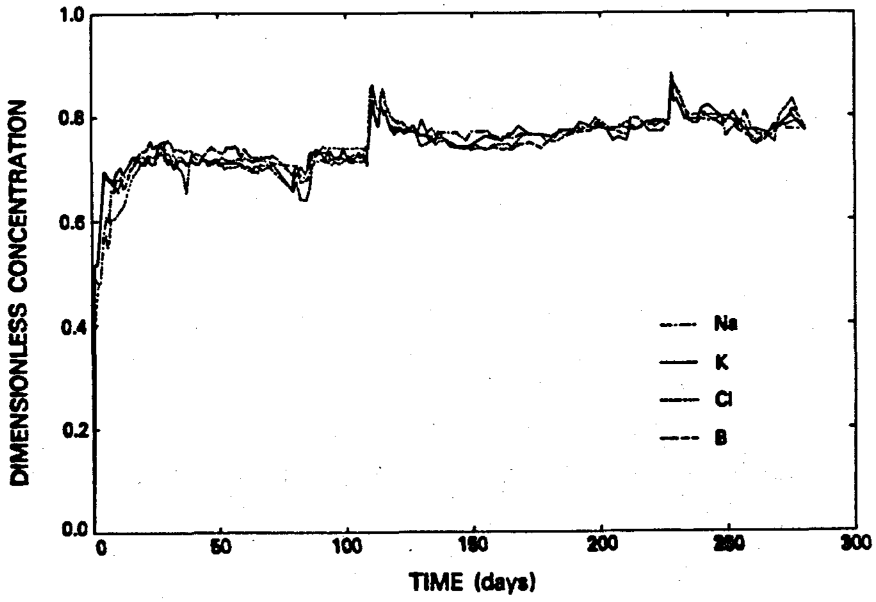

Fig. 7-8.
Comparison of nondimensional concentrations for several reservoir species.

where C^{∞} is the pore fluid concentration, C_m is the make-up concentration, and C(t) is the produced fluid concentration of a given species at time t. As was observed for these species in Run Segment 4, the ratios are constant over long periods of time, and the pore-fluid concentrations C^{∞} used in this normalization are very close to those used in Run Segment 4.[8] Table 7-III gives the C^{∞} and C_m values used for normalizing these species in both the Run Segment 4 and the Run Segment 5 tests.

The flow rate at which the pore fluid enters the circulating system can be calculated by considering the increase in concentration of the circulating fluid as it passes through the downhole system. The reservoir can be treated as consisting of two parallel flow paths: path 1 is the fracture dominated flow path that includes all of the heat-extraction surfaces discussed thus far, while path 2 is a very low flow-rate path consisting of the connected microfractures and pores in the rock surrounding the heat-extraction portion of the reservoir. Path 1 has a short residence time; the mean residence time is approximately 12 h. Therefore, on the scale of tens of days, the fluid originally in this flow path is completely replaced with the injected fluid that has a characteristic composition of C_{EE-1} ($C_{injected}$). Path 2, on the other hand, has a very long mean residence time, so the fluid displaced from this path is, for long times, pore fluid that has a composition denoted by C^{∞}. This model is shown schematically in Fig. 7-9. If we presume that the concentration of the pore fluid is constant, a mixing relationship between the

TABLE 7-III

VALUES OF C^{∞} AND C_m USED IN CALCULATING THE DIMENSIONLESS CONCENTRATION FOR RUN SEGMENTS 4 AND 5
(Concentrations are in ppm.)

	Run Segment 4		Run Segment 5	
	C^{∞}	C_m	C^{∞}	C_m
Na	1600	130	1675	12
K	95	35	150	5
Cl	1600	30	1390	10
B	47	0	43	0

fluid entering the GT-2B wellbore from path 1 and path 2 is

$$C_{EE-1}(\dot{q}_1) + C^{\infty}(\dot{q}_2) = C_{GT-2} \quad ,$$

where $\dot{q}_1$ and $\dot{q}_2$ are the flow fractions in path 1 and path 2. Because $\dot{q}_1 + \dot{q}_2 = 1$, we can easily solve for $\dot{q}_2$. A plot of $\dot{q}_2$ vs time calculated in this manner from chloride, boron, and sodium data is shown in Fig. 7-10. The points shown are the mean values and the bars show the maximum and minimum values. For most of the points, the range is small, and except for the initial transient, the mean value for $\dot{q}_2$ is ~2 to 5% of the flow rate at the GT-2B wellhead.

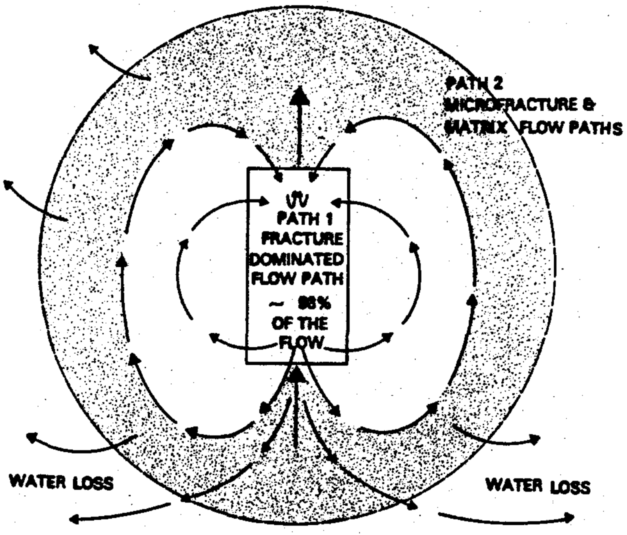

Fig. 7-9.
The two-path reservoir used for modeling the chemical behavior of the reservoir.

Because this analysis presumes that the pore-fluid concentration is constant, the small variation in $\dot{q}_2$ in the last 240 days of the experiment indicates that no breakthrough of fresh water has occurred in the secondary flow path. The slight decline observed in chloride, sodium, potassium, boron, and other species concentrations after the 100th day of the experiment correlates with decline in the injected fluid concentrations as a result of increased dilution of the produced fluid with make-up water prior to reinjection. If the residence time of the secondary flow path is greater than 280 days at ~5 gpm, the total volume of this path is in excess of 6800 m^3 (1.8×10^6 gal). If the volume of the secondary flow path is contained in microfractures, it is apparent that a very large fracture system is connected hydraulically to the main flow path through a large impedance.

7.3. Geothermometry

The quartz geothermometer[22] and the Na-K-Ca geothermometer[23] temperatures have been calculated for the fluid produced during Run Segment 5. A graph of these temperatures as well as the downhole measured temperatures is shown in Fig. 7-11. There is measurable decline in downhole temperature in the Run Segment 5 test. This temperature decline is observed in the quartz

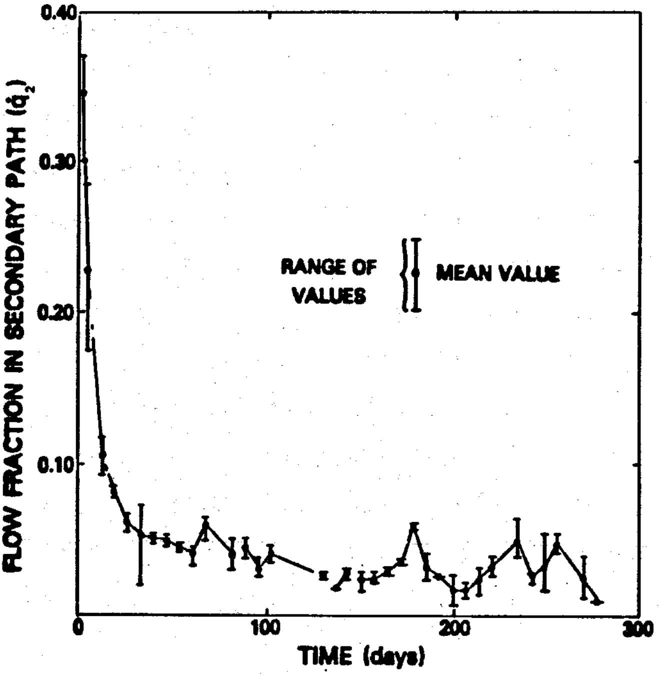

Fig. 7-10.
Calculated pore flow from two-path model.

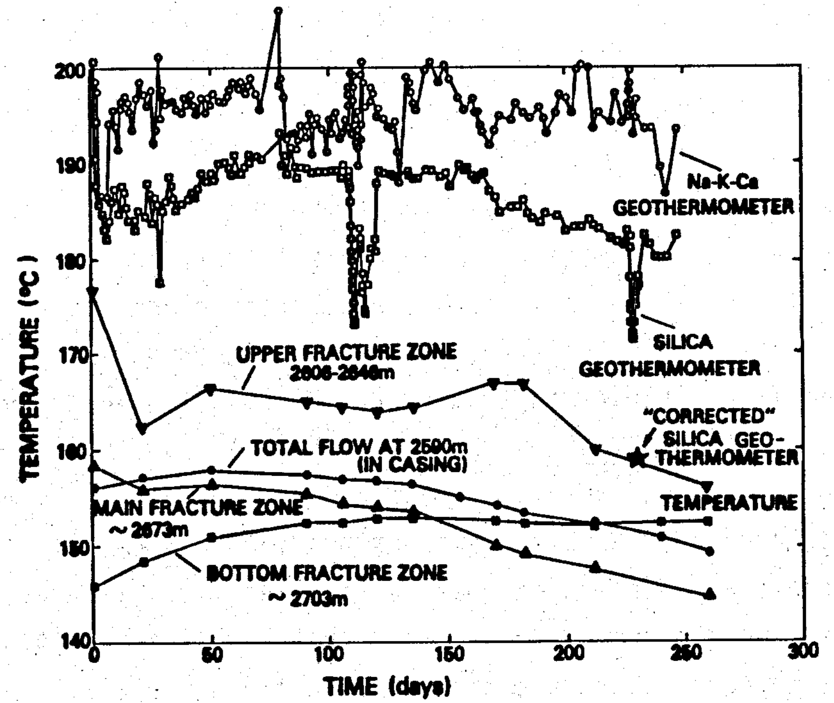

Fig. 7-11.
Comparison of calculated geothermometer temperatures and measured downhole temperatures.

geothermometer; however, no similar decline is seen in the Na-K-Ca geothermometer. In addition, the Na-K-Ca geothermometer is affected significantly less during the open-loop portions of Run Segment 5 (FWF) than is the quartz geothermometer. This insensitivity of the Na-K-Ca geothermometer to reservoir temperature decline and to changes in inlet-fluid composition during a test is due to the constant Na/K ratio in the pore fluid, which is displaced from the secondary flow path. This Na/K ratio in the pore fluid is fixed by equilibrium with the feldspars at the initial rock temperature (∽195 to 198°C), and dilution of the pore fluid with fresh water (containing very low Na and K concentrations) does not affect the Na/K ratio in the produced fluid. Because re-equilibration of this geothermometer is extremely slow (see, for example, Ref. 24), the Na-K-Ca geothermometer reflects the initial rock temperature rather than changes in the reservoir temperature as a result of heat extraction.

The quartz geothermometer, on the other hand, is affected by changes in temperature in the main flow path as well as changes in the inlet-fluid composition. This is particularly true when a sudden change in inlet-fluid composition exceeded the ability of the main flow path to dissolve quartz and thus raise the silica concentration in the produced fluid. Re-establishing the closed-loop mode resulted in a rapid rise in the silica concentration back to the pre-open-loop levels.

The constant difference between the temperature measured downhole and that predicted by the quartz geothermometer is largely due to the addition of small amounts of pore fluid that are saturated with quartz at the initial rock temperature. It is likely, however, that at least some fraction of the silica in the produced fluid is derived from quartz dissolution in the main flow path.

7.4. Fresh-Water Flush (FWF)

In order to resolve questions about how the quartz geothermometer applies to the Phase I reservoir, an experiment was designed to perturb the steady-state chemical interactions within the system. This experiment, termed the FWF, called for the sudden change from recirculating or closed-loop operation to open-loop operation where the injected fluid was all fresh water. The intent was to determine the flux of silica into solution as a result of quartz dissolution in the main flow path.

The rate at which quartz dissolves locally depends upon the following factors:

- temperature of the rock/fluid interface,
- kinetic dissolution rate of quartz [f(T)],
- rate of precipitation of a secondary silica phase [f(T)],
- ratio of quartz surface area to fluid volume,
- solubility of quartz [f(T)],
- fluid flow rate, and
- local degree of undersaturation [f(inlet fluid composition)]

For a FWF experiment, all of these factors except the last (the inlet-fluid composition) are held constant. For the duration of the FWF experiment, the temperature change in fracture system due to heat extraction would be negligible. Indeed in 286 days of heat extraction, the observed drawdown was only 8°C. The response of the reservoir to the step change in inlet concentrations can be used to sort out contributions of silica from different flow paths within the reservoir.

Two FWF experiments were performed during the course of Run Segment 5 operations. The first of these occurred from June 26 to July 7, 1980, and the second was from October 22 to October 26, 1980. For the first FWF, approximately 250 000 gal of fresh water were injected into the system, whereas the fluid produced at GT-2 was vented to the GT-2 pond. The system was then returned to closed-loop operation. The concentrations of dissolved species such as silica and chloride in the produced fluid declined in response to the fresh water injection (Figs. 7-1 through 7-6). After 2 days of closed-loop operation, a second part of the experiment was started. In this part, 50% of the injected flow was fresh make-up water and the other 50% was produced (GT-2) fluid. The rest of the produced fluid was vented to the EE-1 pond. This mixture gave an injected-fluid composition intermediate to the normal closed-loop operation and the open-loop FWF operation. Here, the concentrations of silica and chloride declined; however, the decline was slightly less steep than was observed in the first part of the experiment (Figs. 7-1 through 7-6). After part 2 was completed, the silica and chloride concentrations in the produced fluid recovered to their pre-FWF values.

For the October test, 250 000 gal of fresh water were injected and the produced fluid was discharged to the EE-1 pond. After the 250 000 gal of fresh water had been injected, the system was returned to closed-loop operation. The recovery of the system to pre-FWF concentration levels was interrupted by a power outage that forced the shutdown of the pumps.

Two methods for analyzing the response of the reservoir to the FWF experiment have been considered. The first involves solving the mass balance equation

$$\frac{\partial C}{\partial t} + U \frac{\partial C}{\partial z} = KA \frac{C^{sat} - C}{V} \tag{7}$$

for a series of control volumes at different temperatures along the fracture surface. In this equation, $\partial C/\partial t$ is the accumulation term, $U\ \partial C/\partial z$ describes the change in fluid composition along a flow streamline with local velocities U in the z direction, and $KA(C^{sat}-C)/V$ describes the rate of dissolution of quartz. Both K, the kinetic-rate constant, and C^{sat}, the saturation concentration of silica, are exponential functions of temperature. Temperature is a function of distance along the fracture, flow velocity, and time. Incomplete knowledge of the temperature dependence of quartz dissolution kinetics as well as lack of knowledge of the temperature distribution in the fracture system has been the main impediment in analyzing the FWF experiment by this approach.

The second method will predict the amount of quartz that has dissolved in the main fracture path and can be used to determine the maximum temperature in the fracture without requiring knowledge of quartz dissolution kinetics. This approach is developed by considering the changes in output concentrations of two parallel flow paths as shown in Fig. 7-9. First, let us consider the response of a soluble species such as chloride.

Because path 2 has a very long residence time compared to the duration of a FWF experiment, the output concentration path 2 remains constant at C^{∞}. On the other hand, the fluid in path 1 is soon diluted and removed from the reservoir, and this fluid is ultimately replaced by fresh water. The chloride produced by path 2 is simply the flow fraction in path 2, $\dot{q}_2$, times the concentration of fluid from that path, C^{∞}. For path 1, the chloride concentration is initially C_{EE-1}, which is simply the chloride concentration in the injected fluid during closed-loop operation, but during a FWF, this declines to C_m, which is the chloride concentration in the make-up fluid. The rate of chloride decline in path 1 is related to the residence time distribution (RTD) for that path. The response to a step change in input concentration is the integral of the RTD, which results from a pulse input such as is commonly measured by dye and radioactive tracers.[5,24,25] If we designate this integral as F(t), then the chloride concentration in the fluid produced at GT-2 is

$$C(t) = \mathring{q}_2 C^{\infty} + \mathring{q}_1 \left[C_{EE-1}\, F(t) + C_m \left[1 - F(t) \right] \right] \tag{8}$$

(F(t) = 1 for t = 0). Because C(t) varies between C(t = 0) and C(t = ∞), the concentrations can be normalized by defining a dimensionless concentration, θ, as

$$\theta = \frac{C(t) - C(t = \infty)}{C(t = 0) - C(t = \infty)} \quad . \tag{9}$$

It is quite simple to show that

$$\theta = F(t) \quad . \tag{10}$$

A plot of F(t) vs time using data from the NH_4Br^{82} tracer experiment of September 3, 1980, is given in Fig. 7-12. The curve is inverted from the normal sense of direction for tracer experiments (increasing concentration with time) because the "tracer" used in the FWF experiments was more dilute than the fluid in the system. Chemical data from the October FWF were used for the preliminary analysis for reasons that will be discussed shortly. Combining Eqs. (9) and (10) and rearranging, we find

$$C(t = \infty) = \frac{C - F(t)C(t = 0)}{1 - F(t)} \quad . \tag{11}$$

At each time, we know the value of C(t) and F(t), and the value of C(t = 0) is simply the chloride concentration before the start of the FWF (∿305 ppm). Equation (11) was applied to the chloride data, and a value for C(t = ∞) of 72.4 ± 2.4 ppm was found to be the optimum. Substituting for C(t = ∞) in Eq. (9), values of $\theta(t)$ were calculated, and these values are plotted vs time as the triangles in Fig. 7-12. A similar approach is followed for the silica. Here, C(t = ∞) = 156.6 ± 2.4 ppm. The comparison of θ vs time for silica is shown in Fig. 7-12 as the open circles.

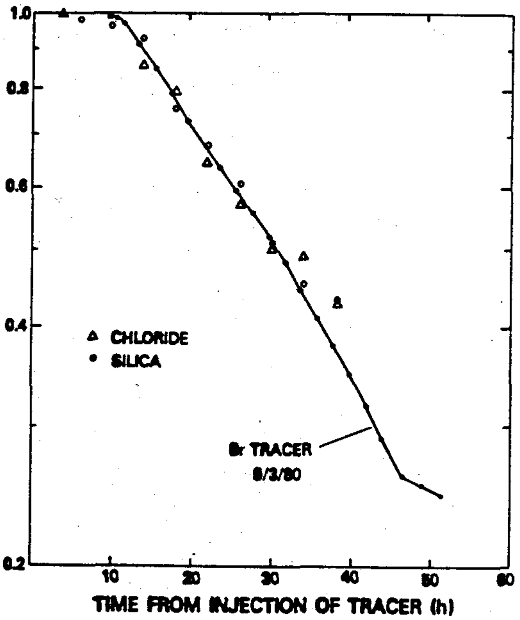

Fig. 7-12.
Comparison of chemical tracer data with NH_4Br^{82} tracer data for tracer experiment of September 3, 1980.

This analysis predicts that the chloride and silica concentrations in the produced fluid would be 72 and 157 ppm, respectively, if the FWF had been continued until steady state had been reached. The amount of silica added by the secondary flow path can be subtracted from 157 to find the ultimate contribution of the main flow path to the silica concentration measured at GT-2. The initial rock temperature is approximately 195 to 198°C, as estimated by the Na-K-Ca geothermometer, so the silica concentration of the fluid leaving the secondary flow path should be $\sim$260 ppm. This estimate compares with the silica concentration of 267 ppm in the second sample collected during this experiment. The amount of silica contributed by the secondary flow path is $\dot{q}_2\ C^{sat} \sim 13$ ppm. Subtracting this from 157 ppm, the silica concentration in the fluid that transits the main flow system is found to be $\sim$144 ppm. Applying the quartz geothermometer to this silica concentration, the temperature at which this fluid would come to equilibrium with quartz is 159°C. This temperature is shown on Fig. 7-11 as the star at about 230 days. The calculated maximum temperature is higher than the mean measured downhole temperature by about 8°C. This "corrected" value of the silica temperature is much closer to actual temperatures measured in a production well; however, there is considerable uncertainty in the result because of the assumptions inherent in this type of modeling. How the experiment is conducted can seriously affect the outcome as well. During the first FWF, pressure levels in the reservoir were not maintained as high as the pre-FWF pressure levels so that considerable flowback of water from the formation occurred. The production flow rate was about 2 to 5 gpm higher than the injection flow rate. Because the composition of the fluid flowing back from the formation is unknown, this earlier experiment cannot be evaluated simply. Further studies of the FWF experiments, particularly when good kinetic data for quartz dissolution are available, should allow the interpretation of this earlier experiment.

As can be seen from the discussion, the FWF experiment can be used to adjust the silica geothermometer to within a few degrees Celsius of temperatures actually measured downhole. Much of the uncertainty would be eliminated by continuing such an experiment to the steady-state condition before returning to closed-loop operation. In addition, knowledge of the temperature dependence of quartz dissolution kinetics and of the rate of removal of silica by mechanisms, such as precipitation of secondary silica phases, will increase the level of detail observable by this type of experimentation.

7.5. Dissolved Gases

Calculations of carbonate equilibria for fluid and gas analyses from Run Segment 4[26] indicate that the CO_2 fraction in the gas phase is close to saturation with respect to carbonate species (predominantly HCO_3^-) in the aqueous phase at the temperature and pressure conditions occurring in the gas separator. Throughout much of the Run Segment 5 test, the HCO_3^- levels were 10 to 20% above the (steady-state) HCO_3^- levels observed in Run Segment 4. The higher CO_2 fraction in the gas phase observed during Run Segment 5 is probably due to the higher HCO_3^- concentrations in aqueous solution; however, calculations to support this statement have not been made. Within the scatter of the gas analyses, the gas concentrations appear to be constant with time (Fig. 7-6).

The depletion of oxygen relative to nitrogen is an indication that oxidation is occurring within the reservoir. Two likely mechanisms are (1) the oxidation of the iron casing and (2) the oxidation of pyrite (FeS_2) in the rock to produce hematite or magnetite and sulfate ions in solution. The high sulfate concentration in the fluid (Table 7-I) could be explained by the second mechanism, whereas the presence of free hydrogen could result from the hydrolysis of water by either of these mechanisms. Equilibria among sulfur and iron species in geothermal systems often depend on iron-bearing alteration phases in the reservoir rock such as epidote and chlorite,[27,28] for which thermodynamic data are sparce or unavailable. However, the presence of these species in the core samples[29] suggests that the requisite alteration phases could be participating in reactions.

7.6. Radon

Radon (^{222}Rn) is the radioactive daughter product of radium (^{226}Ra) decay by alpha emission. The emanation of radon from the rock depends very strongly on the surface area of rock exposed to the fluid.[30] Because of its short half-life (∿3.83 days), radon has been used as an internal tracer in hydrothermal systems to study changes in fracture permeability.[31] Radon analyses were performed during Run Segment 2 to look for changes in rock surface area that could be attributed to thermal stress cracking.[32]

Results of radon analyses performed during Run Segment 5 are shown in Fig. 7-7. Although there is wide variation in the data, several observations can be made: (1) The initial radon concentration was low and increased with time; (2) the radon reached steady-state levels of around 9-10 nCi/ℓ; and (3) during the FWF episodes, the radon concentrations decreased.

Consider the steady-state behavior of radon. Let the radon activity in the produced fluid be constant at 10 nCi/ℓ and let the make-up fluid contain insignificant radon activity. A nonradioactive tracer is used to mark a volume of fluid at time t = 0. The produced fluid including our nonradioactive tracer is diluted by ∿7% with make-up fluid so that the radon activity in the injected fluid is ∿9.3 nCi/ℓ. The mean residence time of the fluid in the wellbore and fracture system is ∿15 h and the radon in the fluid element will decay by the relation

$$A_{Rn} = A^{\circ}_{Rn}\, e^{-\lambda t} \quad ,$$

where A°_{Rn} is the injected radon activity (9.3 nCi/ℓ) and λ is the decay constant ($\lambda = 0.007553\ h^{-1}$ for ^{222}Rn). The radon in the produced fluid, then, consists of 8.3 nCi/ℓ, when it is produced at GT-2B after being injected 15 h earlier. The amount of radon produced in the reservoir at steady state is the difference or 1.7 nCi/ℓ.

Kruger et al.[32] calculated a source strength for Rn based on the measured value of 1.7 pCi/g of radium in the rock and estimates of the emanation power (EP) of 0.1 and of the porosity of the rock (including microfractures) of $\phi = 0.01$:

$$\mathrm{Rn} = \frac{[\mathrm{Ra}]\,(\mathrm{EP})\,\rho_{\mathrm{rock}}}{\phi} = \frac{1.7\mathrm{pCi/g}\,(0.1)(2.5\ \mathrm{g/cm^3})}{0.01}$$

$$= 42.5\ \mathrm{pCi/cm^3} = 42.5\ \mathrm{nCi}/\ell\ .$$

Using this value as the radon activity of the pore fluid as it enters the circulation system, the contribution of the secondary flow path is estimated to be

$$[\mathrm{Rn}]_2 = \dot{q}_2\ (42.5\ \mathrm{nCi}/\ell)\ e^{-\lambda t}\ ,$$

where $\dot{q}_2 \sim 0.02 - 0.05$ and t is the time for a given volume of pore fluid to transit the GT-2 wellbore after entering the fracture system. Values for t range from 3 to 7 h. The range in radon activity produced in path 2 according to these assumptions is 0.81 to 1.66 nCi/ℓ or 50 to 100% of the radon needed to maintain the steady-state conditions. It is apparent from this analysis that new heat-transfer surface created in the fractured portion of the reservoir will not be observed in the radon data obtained during closed-loop operation.

7.7. Comparison with Previous Experiments

Run Segment 5 is basically a continuation of the low back-pressure portion of Run Segment 4. The results of these two tests are understandably quite similar. As was concluded in Run Segment 4 (and in Run Segment 2, for that matter), pore-fluid displacement is the single most important process involving the fluid chemistry. As has been described in this section, the pore-fluid contribution to the fluid chemistry determines the temperature predicted by the Na-K-Ca geothermometer and interferes with the temperature prediction in the fracture flow paths based on the silica geothermometer. These points were not clear from Run Segment 4 data; however, they are as valid for Run Segment 4 as well as Run Segment 5. Another interesting feature of the Run Segment 5 results is the suggestion developed in Fig. 7-10 that the pore fluid was displaced at a constant rate and composition throughout most of the test. The volume of displaced pore fluid is in excess of 6800 m^3 (1.8×10^6 gal). A calculation using a microfracture porosity of 0.01 shows that the volume of rock affected by fluid flow and pressurization is 680 000 m^3.

This is equivalent to a circular cylinder of rock with a diameter 330 m corresponding to the wellbore separation distance having a height of 7.95 m.

The completion of a FWF experiment during this test is an important step toward using geochemical data in determining the temperature distribution within a fracture. Significant development remains to be done in modeling and interpreting this experiment; however, it is hoped that a FWF type of experiment may become useful in predicting Phase II reservoir temperatures before measurable thermal drawdown occurs.

Preliminary analysis of the radon data suggests that interpretation of changes in the fracture area by radon transient analysis could be misleading in the same way that interpretation of the quartz and the Na-K-Ca geothermometers could be misleading. Apparently only the heat extraction is confined to the fracture system; the results of the fluid chemistry analyses indicate that the affected rock volume is significantly larger.

8. RADIOACTIVE AND DYE TRACER EXPERIMENTS

In Run Segment 5 the tracers injected were of two types. The first was a visible dye, sodium fluorescein, which was injected down the EE-1 wellbore in a 95-ℓ (25-gal) pulse of water with a 1200 ppm concentration of dye. The dye was then monitored with a uv spectrophotometer in the GT-2B production fluid. This dye was used to obtain volume estimates of the system to be used in comparison with previous experiments. The other tracer, irradiated ammonium bromide, NH_4Br^{82}, was used for two purposes: (1) to give fracture system volumes and (2) to provide mappings of fracture wellbore intersections. There were a total of five NH_4Br^{82} tests performed, four of which were used for the dual purposes just mentioned and one that was used only for fracture mapping. The first of the radioactive tests was conducted with a 40-mCi source strength, and all subsequent tests were conducted with a 400- to 550-mCi source strength. Because of the concern over possible release of radioactive material, a special container was fabricated to transport the NH_4Br^{82} to the site and to inject it into the system. Figure 8-1 is a schematic of the injection system used in the radioactive tracer experiments. A schematic of the surface equipment used for counting the NH_4Br^{82} is shown in Fig. 8-2.

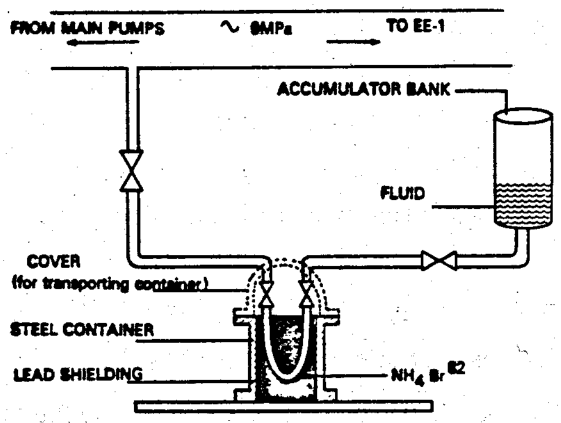

Fig. 8-1.
Schematic of the injection system used in the radioactive tracer experiments.

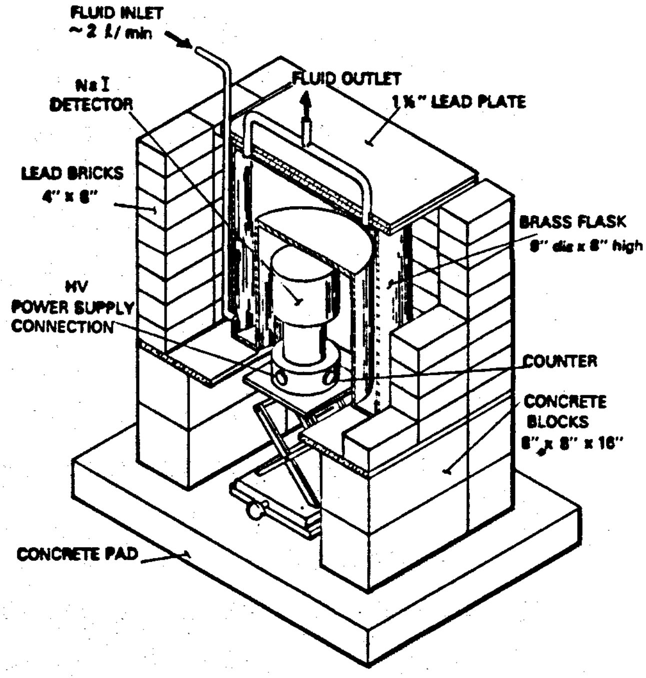

Fig. 8-2.
Schematic of the surface equipment used for monitoring the radioactive tracer activities.

8.1. Tracer Volume Studies

One of the main objectives of the tracer studies is to assess the volume changes associated with the creation of the Phase I (Run Segment 5) system and also to determine the dynamic behavior of the system volume as the system undergoes long-term heat extraction. Flow conditions and preliminary results of Run Segment 5 tracer tests are compared with tracer tests conducted during Run Segment 4 in Table 8-I. In this table, the definitions of modal volume, integral mean volume, and variance are the same as those presented by Tester et al.[5] and are presented in Appendix A. Comparison of the modal volumes from Run Segments 4 and 5 shows a regular increase of the modal volume with time. This volume increase is attributed to thermal contraction effects due to heat extraction, which is analyzed in more detail below. A rather large change in the modal volume is observed after the hydraulic fracturing of the system during the SUE in the December 12 tracer experiment.[10]

The integral mean volumes do not show this regular increase because of the difference in volume of fluid produced during a given experiment. For example, during the tracer test run on September 3, 4140 m^3 of fluid were produced. Even the very low concentrations of Br measured at the high volumes tend to skew the distribution towards longer residence times and a larger calculated mean system volume. In contrast, during the subsequent tracer experiment on December 2, 1980, counting continued only until 1310 m^3 were produced so that the tail of the distribution was effectively (if unintentionally) eliminated. Because of equipment malfunction, the data for the December 2 and 12 experiments were recorded by hand at roughly 1-h intervals. Unfortunately, data for the 6-h period centered at about the modal volume in the December 2 experiment were not recorded. The modal value for this experiment presented in Table 8-I was found by superimposing the data measured downhole with the data measured at the surface. The mode of the downhole data was then adjusted for the transit time to the surface to give the mode in the surface data.

The highly increased sensitivity of the method for analyzing Br^{82} over that for Na-Fluorescein is responsible for the longer tails on the bromine tracer experiments. Dye tracer experiments typically end when the dye concentrations in the produced fluid can no longer be measured (typically <1400 m^3 total produced volume at GT-2B). Bromine tracer experiments, on the other hand, have continued to 4140 m^3 without completely reaching background.

TABLE 8-I

SUMMARY OF DYE AND RADIOACTIVE TRACER EXPERIMENTS IN RUN SEGMENTS 4 AND 5

Experiment and Date	Tracer[a]	EE-1 Injection Pressure MPa	GT-2B Production Pressure MPa	GT-2B Production Flow Rate (m^3/s)	Average[b] Production Temperature (°C)	Cumulative Power Extracted During each Run Segment $(10^6$KW-h)	Modal[c] Volume (m^3)	Integral Mean Volume (m^3)	Total Produced Vol During Tracer Test (m^3)	Variance σ_θ^2
Run Segment 4										
10/26/79	F	17.2	1.1	0.0064	153.	0.1	136.	207	469	0.26
10/29/79	F	17.2	10.3	0.0081	154.	0.3	144.	230	619	0.17
11/2/79	F	9.3	1.1	0.0066	153.	0.6	121.	262	570	0.38
11/12/79	F	9.3	1.1	0.0064	153.	1.3	129.	283	662	0.32
Run Segment 5										
4/15/80	F	9.8	1.3	0.0075	158.	1.6	155.	404	1440	0.45
5/9/80	B	9.5	1.3	0.0071	158.	2.8	161.	1100	3030	0.53
9/3/80	B	8.8	1.3	0.0070	154.	7.5	178.	1511	4140	0.56
12/2/80 (Pre-SUE)	B	8.5	1.1	0.0065	149.	11.1	187.	581	1310	0.40
12/12/80 (Post-SUE)	B	8.4	1.3	0.0098	149.	11.4	266.	1118	2690	0.46

---

[a] F = Sodium fluorescein dye, B = ^{82}Br.

[b] Reservoir outlet temperature measured downhole.

[c] Modal Volume is defined as the volume of tracer circulated through the fracture system from time of entry until that time at which the tracer concentration at the outlet is maximum. We believe this volume to be the most easily measured one, as well as the most unambiguous one for making comparisons of the effect of pressure or temperature or fracture size.

Integration of the long tails of the RTD curves biases both the integral mean volume and the variance to higher values. To eliminate the effect of this bias, Tester et al.[5] truncate the integration when 90% of the tracer has been recovered. Another way to remove the effects of long residence times is to truncate the distribution at a fixed produced volume, for example, 1136 m^3 (300 000 gal). Variances for Run Segment 5 were calculated for the full integrated distribution, the 90% trimmed mean, the 75% trimmed mean, and for 1136 m^3. These values are given in Table 8-II. The variances for the trimmed distributions still show the effects of the long tails; however, the distributions truncated at 1136 m^3 indicate that up to this point the integrated distributions have roughly the same variance. That is, the flow distribution is not changing drastically. The large shift in distribution occurs before the last (that is, post-SUE) tracer experiment. This change is reflected in the modal volume, however, the variance of the total (that is, 100%) distribution is similar to that of the other tracer experiments conducted during Run Segment 5. This effect is most clearly shown in Fig. 8-3 where normalized tracer concentrations are plotted vs produced volume. (The wellbore volumes

TABLE 8-II

STATISTICAL VARIANCE FOR VARIOUS INTEGRAL VOLUMES

Date	Integral Mean	90% Trimmed Mean	75% Trimmed Mean	Variance Trimmed at a volume of 1136 m^3
4/15/80	0.45	--	0.35	0.38
5/9/80	0.53	0.52	0.49	0.37
9/3/80	0.56	0.54	0.47	0.34
12/2/80	0.40	0.38	0.36	0.38
12/12/80	0.46	0.42	0.40	0.29

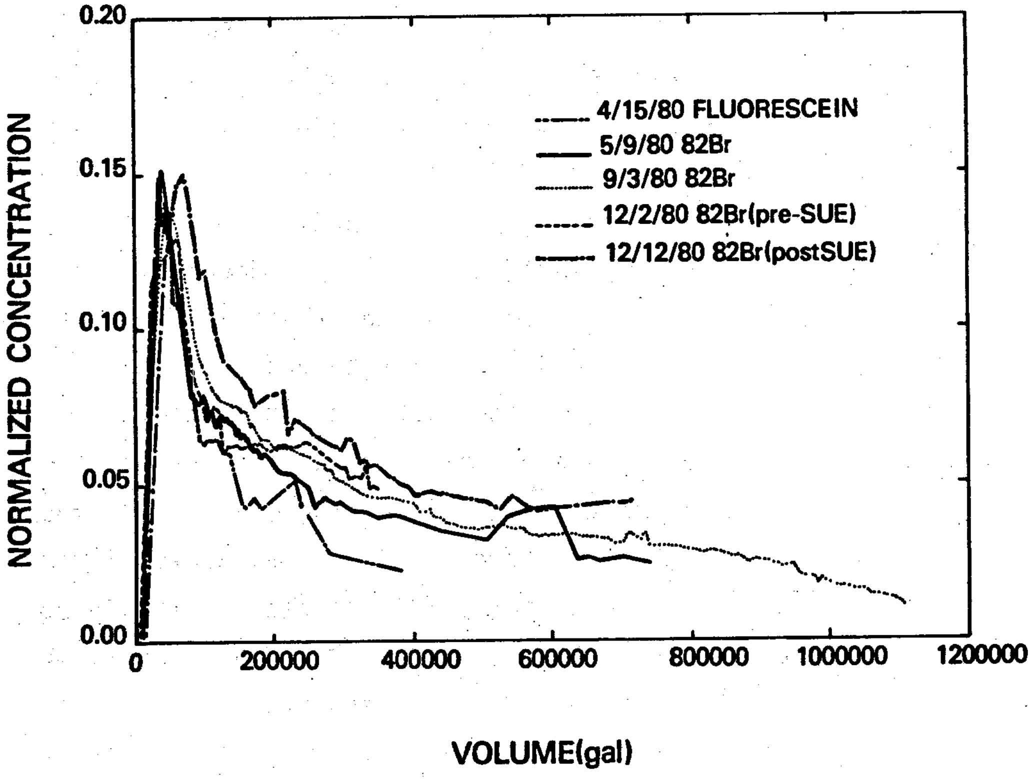

Fig. 8-3.
Variation of normalized tracer concentrations with produced volume of fluid.

have been subtracted so that the volume shown is a fracture system volume.) Because of the inconsistency in the calculated integral mean volumes, the usual normalization procedure, which relates the concentration to the integral mean volume <V> and the fraction of tracer which is recovered $\int_0^\infty C_i i dV$,

$$C_\theta = C_i \Big/ \left[\frac{1}{\langle V\rangle} \int_0^\infty C_i \, dV\right]$$

cannot be used. A much more meaningful procedure substitutes the modal volume $\overset{\circ}{V}$ for the integral mean volume in the above equation:

$$C_\theta = C_i \Big/ \left[\frac{1}{\overset{\circ}{V}} \int_0^\infty C_i dV\right] .$$

In this case, the concentration is normalized to a measured volume (the mode), which is a feature of the residence time distribution that is independent of the tracer used. The second normalization procedure is used for producing Fig. 8-3. The really significant difference among the Run Segment 5 tracer experiments is the drastic increase in modal volume due to the SUE experiment. However, the mode increases regularly with time. Apparently, the volume of the system increases systematically, whereas the shape of the distribution remains fairly unchanged even after the SUE (Table 8-I).

Because the volume changes in the mode are attributed to thermal contraction of the rock, the modal volume was plotted against thermal energy extracted in Fig. 8-4. A reasonably linear increase of fracture modal volume occurred as heat was extracted, and the total heat extracted E resulted in a volume increase ΔV of 37 m^3. The energy E is related to the integral of the temperature decrease over the entire reservoir rock volume affected by thermal drawdown. If the rock is assumed to be a stress-free, freely contracting medium, then ΔV is also related to the same integral, and it can be shown that

$$\Delta V = \alpha_V E/(\rho c) \quad ,$$

where α_V is the volumetric thermal expansion coefficient of the rock and ρc is its volumetric heat capacity. Using a typical value from Ref. 17, $\rho c = 2.7 \times 10^6$ J/(m^3 °C), α_V can be estimated as 3.3×10^{-6} per °C. This is only one-tenth the value typical of laboratory experiments with dense granite.[33] This large discrepancy is attributed to two causes. (1) The rock is actually under considerable tectonic stress, and much of the expected thermal contraction simply was consumed in relieving a part of these stresses; and (2) much of the thermal contraction may have been manifested as an increase in porosity that occurred far enough away from the main fracture system that the

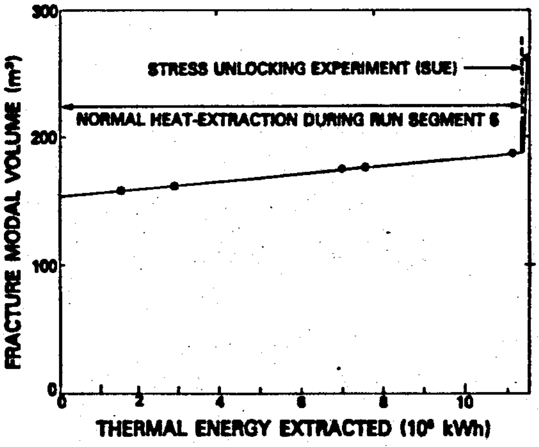

Fig. 8-4.
Variation of modal volume with thermal energy extracted.

porosity increase was not detected by the tracer passing through the fracture system.

8.2. Fracture Mapping with Radioactive Tracers

This section will examine the results obtained from downhole measurements in both wellbores of the gamma-ray activity following the surface injection of a sequence of the five different NH_4Br^{82} tracer sources during Run Segment 5 and provide information about flow distribution and the residence time distributions of individual fractures.

The method, described in detail in earlier reports,[34-39] consists simply of injecting a small sample of NH_4Br solution containing a few hundred millicuries of the Br^{82} isotope. This isotope with a conveniently short half-life ($\sim$35 h) and strong gamma-ray strength ($\geq$1 Mev) provides an almost perfect tracer for following the movement of fluid both in the wellbores and behind the casing with the use of gamma-radiation logging tools.

The details of the surveys are given in Table 8-III. The main differences between them is the change in source strength after the first survey and the absence of logging in one of the holes in several of the surveys.

The following is a description of a typical survey that consisted of monitoring the tracer activity by successive logging sweeps in both boreholes until its value was reduced by system flow to nonuseful levels. The tracer was injected under pressure into the flow stream at the EE-1 wellhead. Its

TABLE 8-III

DETAILS OF TRACER SURVEYS INDICATING SOURCE STRENGTH AND GAMMA-RAY TOOLS

Survey Number	Date	Source Strength (mCi)	Use of Gamma Ray Tools EE-1	Use of Gamma Ray Tools GT-2B
1	5/8/80	40	Yes	Yes
2	9/4/80	400	Yes	Yes
3	9/24/80	400	Yes	No
4 (Pre-SUE)	12/2/80	550	No	Yes
5 (Post-SUE)	12/12/80	400	Yes	Yes

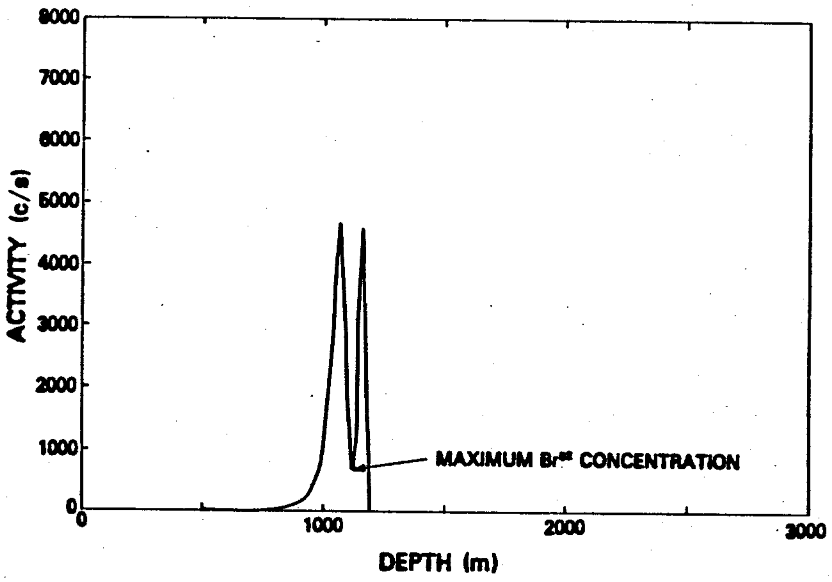

Fig. 8-5.
Variation of activity with depth in the EE-1 borehole.

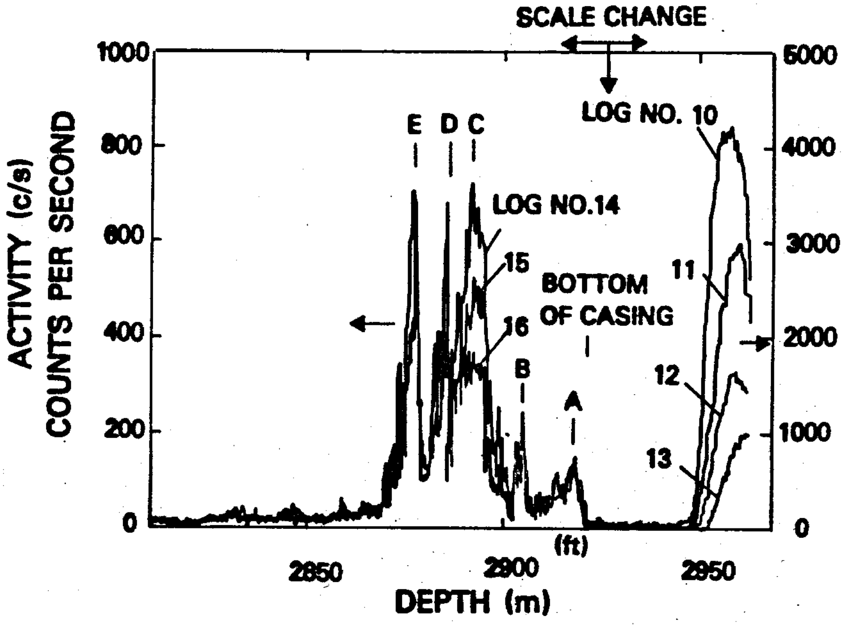

Fig. 8-6.
Variation of activity with time in the EE-1 borehole.

passage down the wellbore was followed by logging through it as shown in Fig. 8-5. The peculiar shape of the activity vs depth curve is due to saturation of the tool at the higher levels of activity. When the tool saturates, its output actually falls, so that the minimum between the two peaks shown in Fig. 8-6 corresponds to the maximum activity. A sequence of these logging scans followed the movement of the location of the maximum value of the pulse as it moved down through the casing and into the openhole section of EE-1. Movement of the tracer into several fractures was detected by changes in the pulse velocity. Figure 8-6 is a typical sequence showing the reduction in activity with time in the openhole section along with later growth in activity at several locations higher in the casing. Each of these several locations in the casing showed a growth of activity followed by subsequent decay. This behavior is interpreted as movement of the tracer through individual fractures crossing the EE-1 wellbore. This observation again indicates the unique value of this wellbore as an observation well, providing information similar to that obtained from temperature recovery logs. The tracer moving through the complex system finally starts to appear in the GT-2B wellbore. A sequence of logging scans in GT-2B followed the arrival and subsequent growth of activity in the flows from the several fractures mapped in the temperature spinner surveys. Figure 8-7 shows such a sequence, with changes in activity caused both by the amount of flow and the level of activity. Again the activity reached a maximum and then slowly died away.

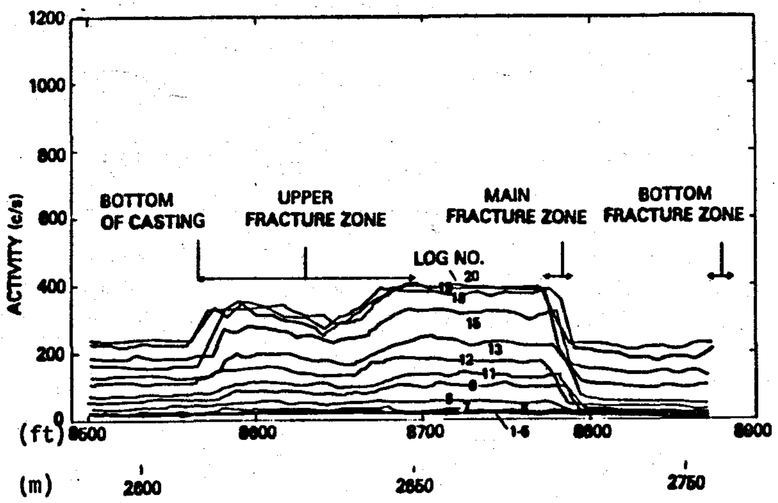

Fig. 8-7.
Variation of activity with depth in GT-2 from logging through the tracer pulse.

8.2.1. Properties of Fractures in the EE-1 Openhole. The fracture intersections with EE-1 that accept fluid can be located by measurement of the velocity changes obtained from sequential logging runs through the moving tracer pulse as described above. Figures 8-8 through 8-11 show the results from the four surveys in which logging was done in the EE-1 wellbore. Significant improvement in the quality of the measurements can be seen in the last two surveys. This was due to both improvement in logging strategy and increased source strength. However, in all of the surveys, well-defined breaks in the logging velocity at several depths indicated the location of specific fractures. Table 8-IV gives both the depth and flow into each of the located fractures. It is difficult to assign a precision to these values, but it is evident that the locations are reasonably well defined and that major changes in the relative values of flow occurred particularly at the 2950-m fracture between the first and second survey and after the SUE.

8.2.2. Properties of Fractures Cutting Across the EE-1 Borehole. In the later stages of logging in EE-1, the history of gamma activity at several depths indicated the passage of the tracer front through fractures behind the casing at these depths. Figure 8-12 shows the activity as a function of time for five such fractures whose locations are shown in Fig. 8-6. (The first survey was normalized to an activity of 400 mCi.) These curves can be used to estimate volume and degree of mixing or dispersion for each such zone. The two fractures (A,B) closest to the injection zone are considerably different

TABLE 8-IV

EE-1 OPENHOLE FRACTURES

Survey Number	Fracture Depth (m) (Flow ℓ/s)			
1	-- (~4)	2950 (~2.3)	2955 (~0.5)	-- (~0.06)
2	-- (~6)	2949 (0.15)	2954 (0.09)	-- (0.09)
3	2940 (6.0)	2948 (0.11)	2953 (0.09)	2959 (0.05)
5	2940 (7.1)	2949 (1.5)	2954 (0.22)	-- (0.16)

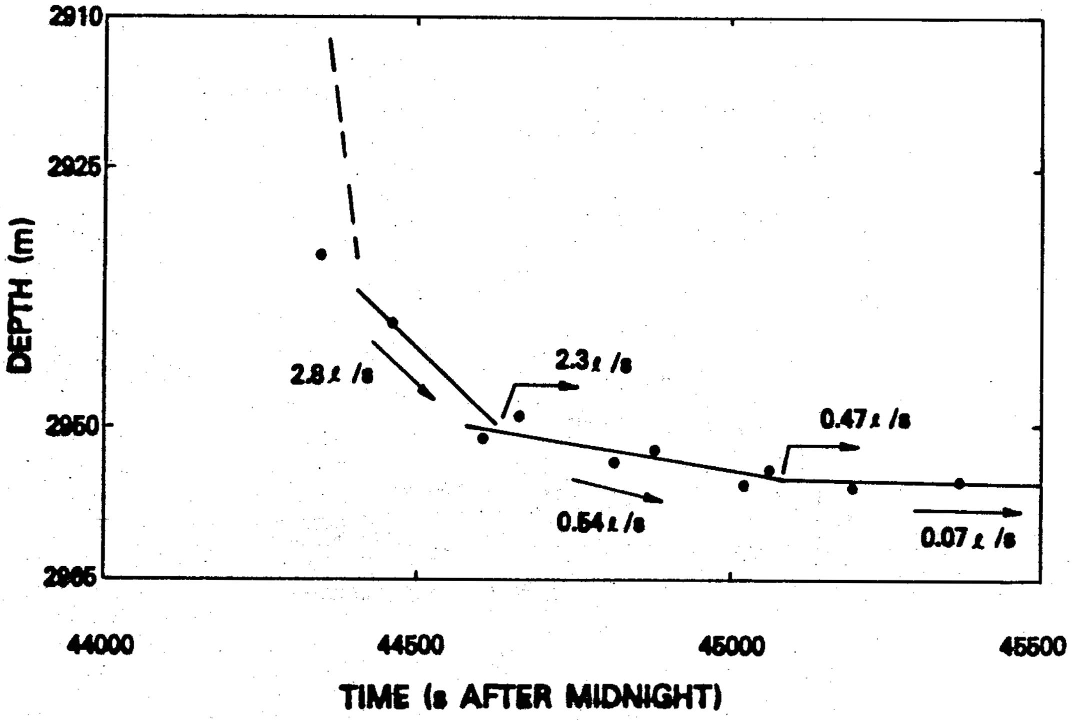

Fig. 8-8.
Movement of tracer in EE-1 on 5/8/80.

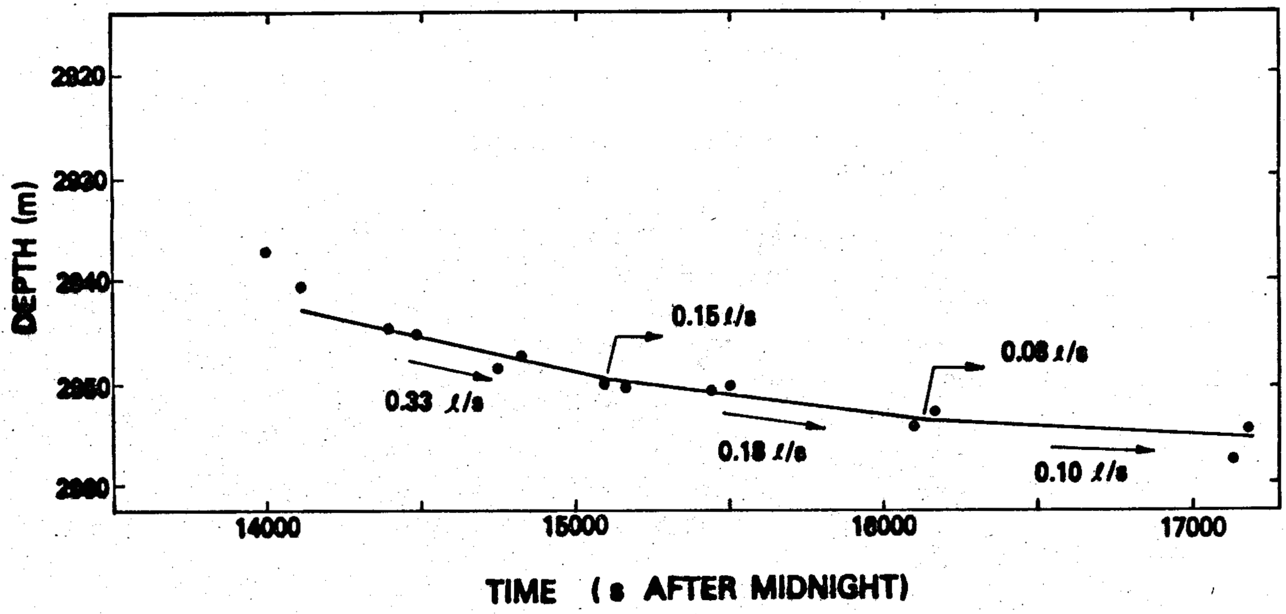

Fig. 8-9.
Movement of tracer in EE-1 on 9/4/80.

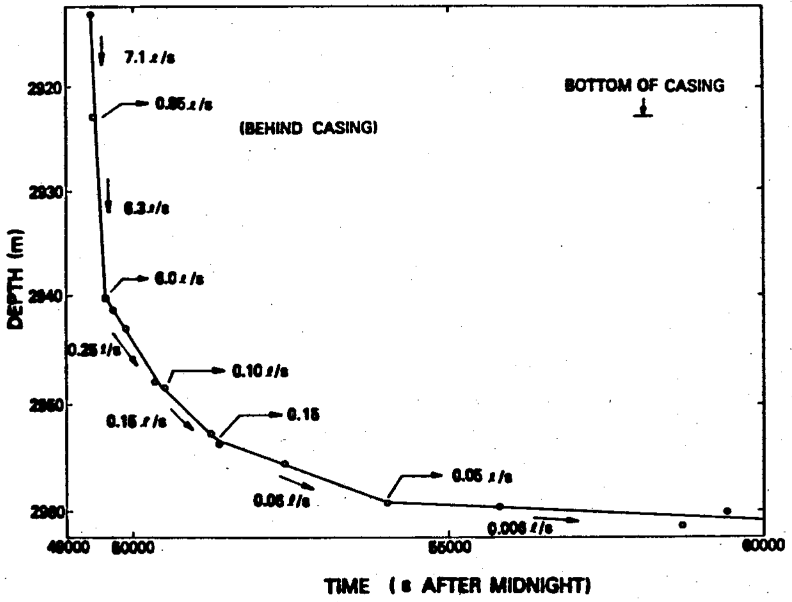

Fig. 8-10.
Movement of tracer in EE-1 on 9/24/80.

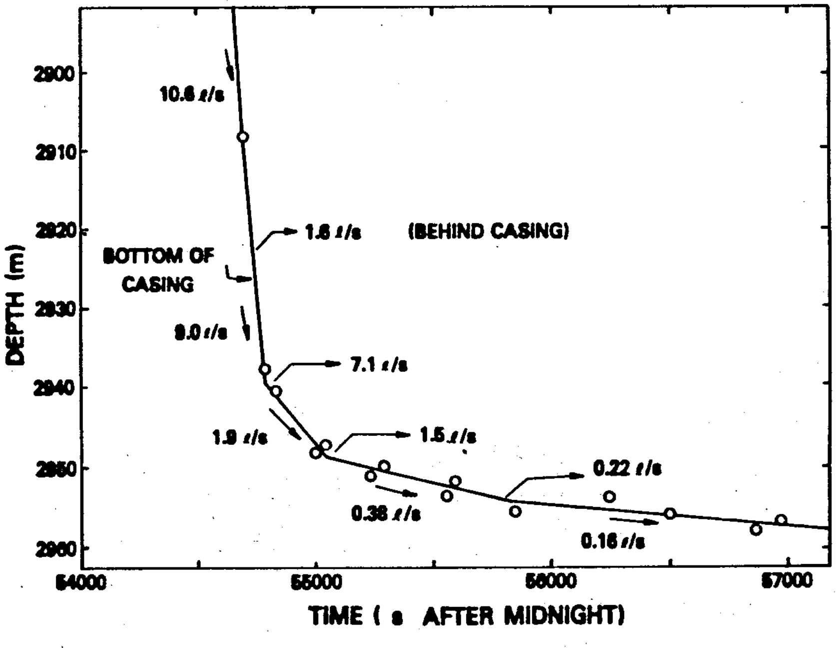

Fig. 8-11.
Movement of tracer in EE-1 on 12/12/80.

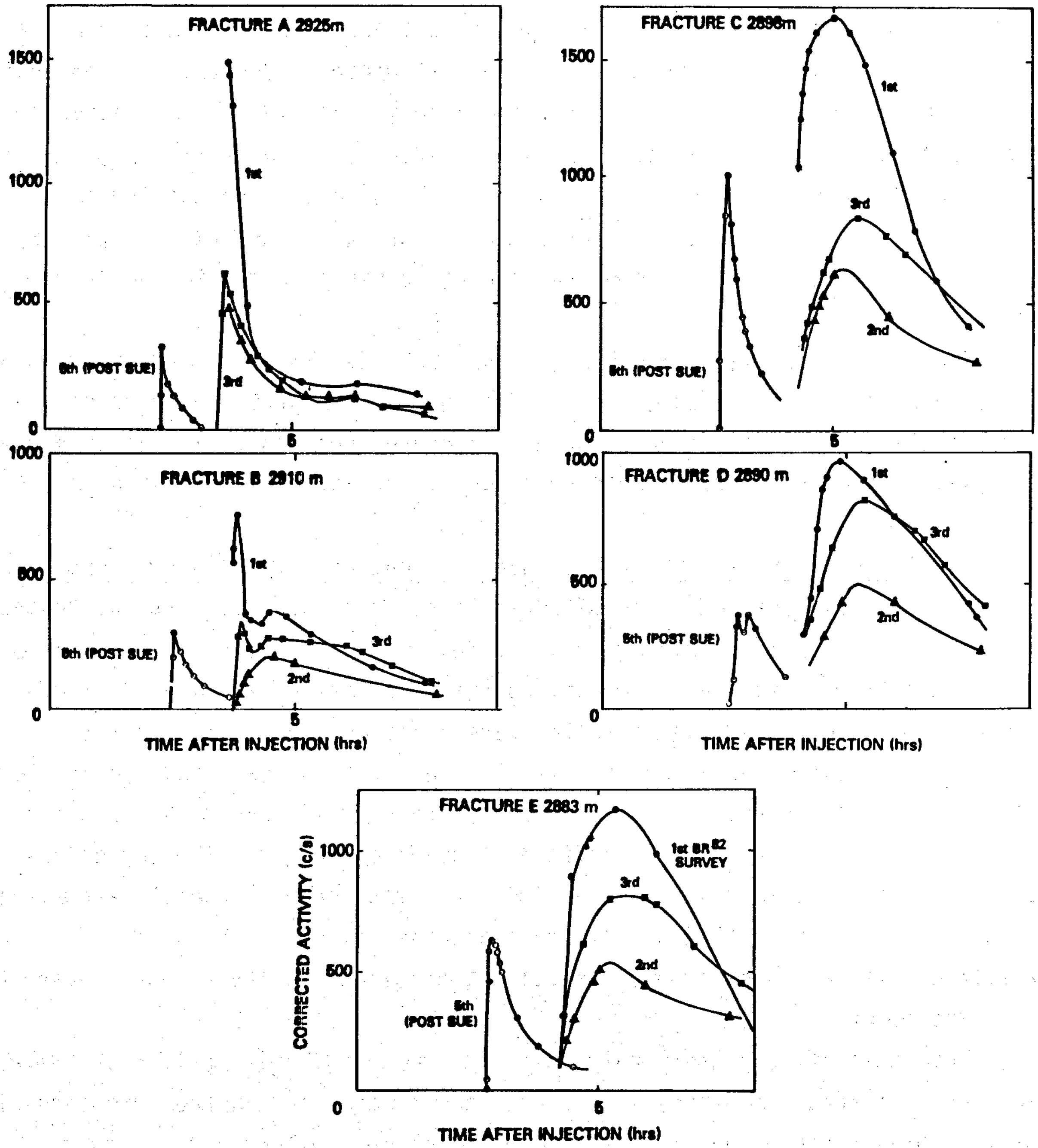

Fig. 8-12.
Variation of activity with time for five fractures cutting across EE-1.

in character as measured in the first three surveys from the upper three (C,D, and E). A crude measure of the size (or volume) of the system sampled at each of these locations in EE-1 is given by the half width of the peak of the activity vs time curve. There is a general increase in this value with increasing distance from the injection point (taken as ~2940 m). The injection of the tracer in the second survey was halted for 13 h to repair the logging tool, which resulted in significant dispersion of the pulse. This may explain the apparent anomalously low values of the second survey relative to the third survey.

The major difference, however, is the change in the shape of the dispersion curves after the SUE experiment. The half widths of the dispersion curves are significantly reduced for all fracture crossings. In addition the risetimes to the maxima are almost an order of magnitude shorter than in the earlier surveys.

8.2.3. Properties of Fracture Intersections with the GT-2B Openhole.

The arrival of the tracer in the GT-2B wellbore is complex in that the tracer activity results from the mixing of individual streams of fluid, each with a different activity history. However, using the relative values of flow obtained from spinner, that is, the flow rate fractions, surveys, and the principle of mass conservation, the level of activity of each individual flow with time can be determined. Figures 8-13 through 8-15 show such histories for the three fracture zones as defined in spinner surveys. The curves obtained from surveys taken before the SUE experiment bear a general resemblance to those obtained from the upper three fractures in EE-1. The post-SUE curves exhibit significant superimposed structure, highlighting the changes caused by this experiment.

The radioactive tracer analysis has become a valuable tool in the determination of fracture geometry. In fact, it was important in the formation of the multiple-fracture heat-transfer model described in Sec. 6.2.

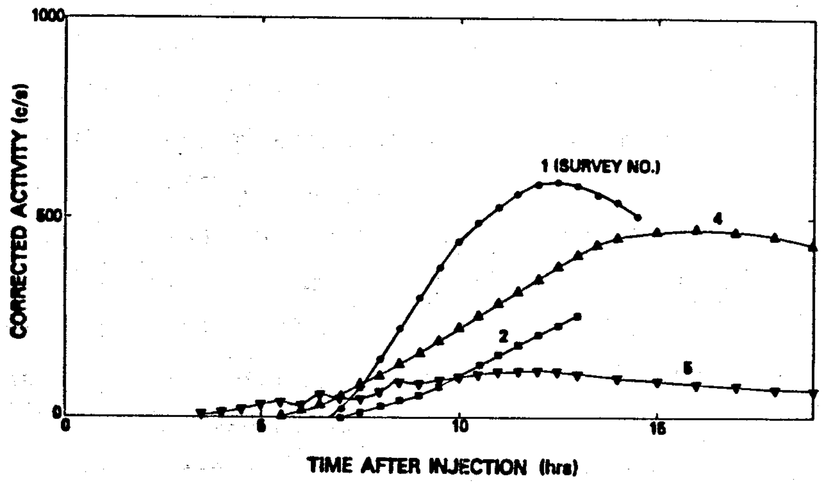

Fig. 8-13.
Variation of activity with time for bottom fracture in GT-2B.

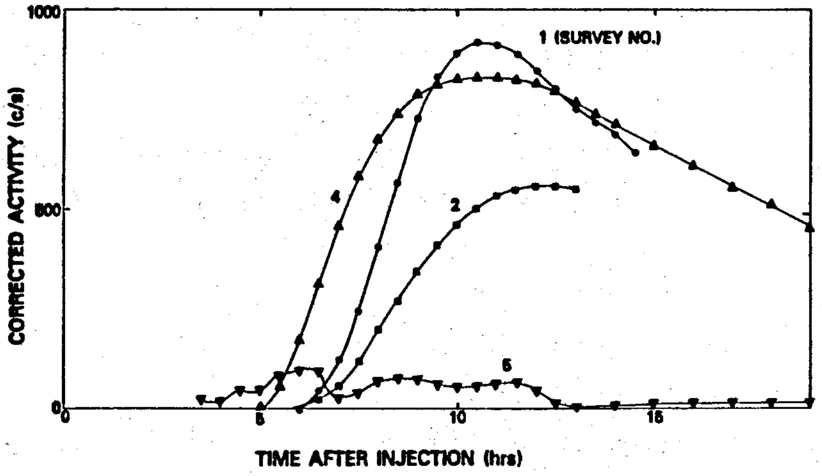

Fig. 8-14.
Variation of activity with time for middle fracture in GT-2B.

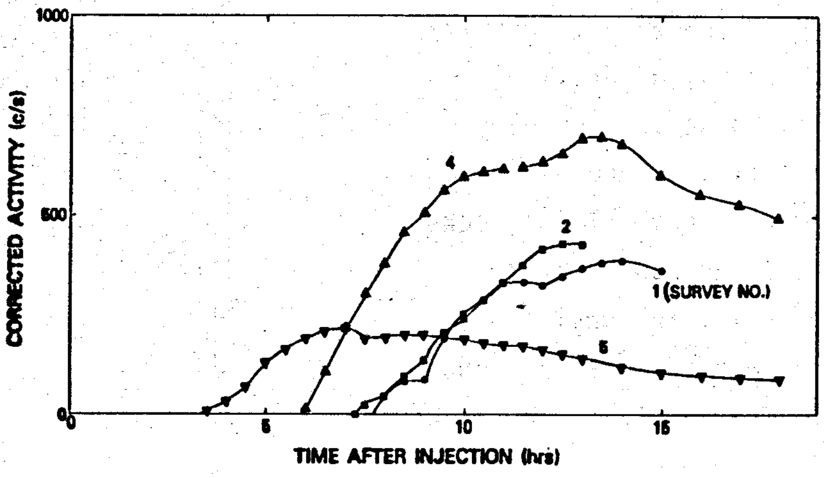

Fig. 8-15.
Variation of activity with time for upper fracture in GT-2B.

9. SEISMICITY

Reservoir seismicity was monitored with a surface seismometer array and a geophone package that was positioned downhole in EE-2 in the reservoir vicinity. EE-2 is a well recently drilled for the Phase II reservoir. For this experiment it served merely as an observation well. The surface array consisted of six stations within 750 m (1/2 mile) of the site, five borehole stations located within 10 km of the site, and the Los Alamos National Laboratory regional net--the nearest of which is located at 10 km. The sensitivity of this surface array extended to Richter earthquake magnitudes of 0 to -1.5 and is limited by the nearly 3 km of vertical separation and the large seismic attenuation of the near-surface sediments and volcanics. The downhole geophone package consisted of 12 geophones, 4 each in the x-, y-, and z-direction axes (Fig. 9-1). The sensitivity of the downhole package during most of Run Segment 5 extended to magnitudes as low as -6. During those periods when the geophones were in place, the drilling rig had to be idled; therefore, the downhole geophones were used only during selected periods. During the 286 days of flow, 13 microearthquakes ranging between -1.5 and 0.5 on the extrapolated Richter scale were recorded by the surface seismic array. These events were located about 200 m north of EE-2 at a depth of about 1 km. The events are not related to Run Segment 5 activities but rather to the drilling of EE-2 or 3. They began about 11 days after EE-2 began losing large amounts [as much as 2×10^{-2} m^3/s (450 000 gal per day)] of drilling fluids at the lithological boundary separating the sediments and volcanics from the Precambrian crystalline rocks below. This leak was caused by a casing failure during the drilling operation. The related seismic events subsided about 60 days after the casing was repaired, but before that about 3×10^4 m^3 (8 000 000 gal) of fluid were

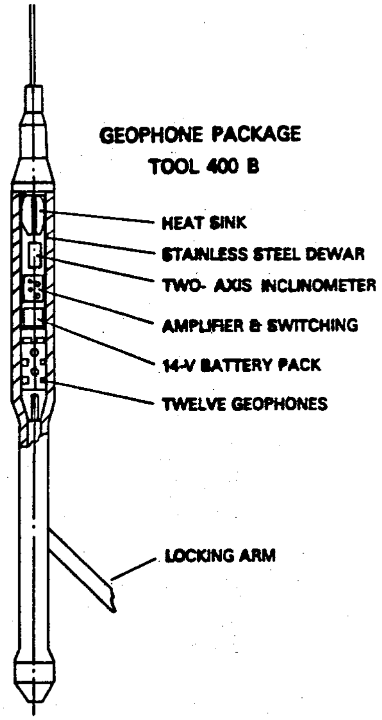

Fig. 9-1.
Los Alamos National Laboratory three-component geophone package.

pumped into the unconformity. It is believed this fluid triggered the release of tectonic stress that had accumulated at the unconformity or related faults. The cumulative seismic-energy release of these events was about that of a M_L = 0.75 earthquake. Locations of these events in plan view are shown in Fig. 9-2.

In an effort to record any seismic events too small to detect using surface geophones, the three-component geophone package was placed in EE-2 at 2100 h, June 24, 1980, and recorded the seismic background noise for 17 h. During this test the geophone was located at three depths (1005 m for 12 h, 1500 m for 0.75 h, and 2606 m for 3.5 h). These depths and times were chosen to allow us to maximize our recording time without overheating the tool and still record data within a few hundred meters of the heat-transfer surface. No events associated with microseismic activity in the HDR system were found at the 1000-m or 1500-m geophone position. However, in the lowest geophone position six events were recorded with clear S- and P-arrivals. They probably occurred near the geothermal system, although the P-wave was emergent and the events could not be located. A sample event is shown in Fig. 9-3. These event frequencies, about two events/hour, are 2 or 3 orders of magnitude less than those observed during Expts. 195 and 203 (fracture extension experiments) or during the high back-pressure phase of Run Segment 4, but are equivalent to event frequencies observed during the low back-pressure phase of Run Segment 4.

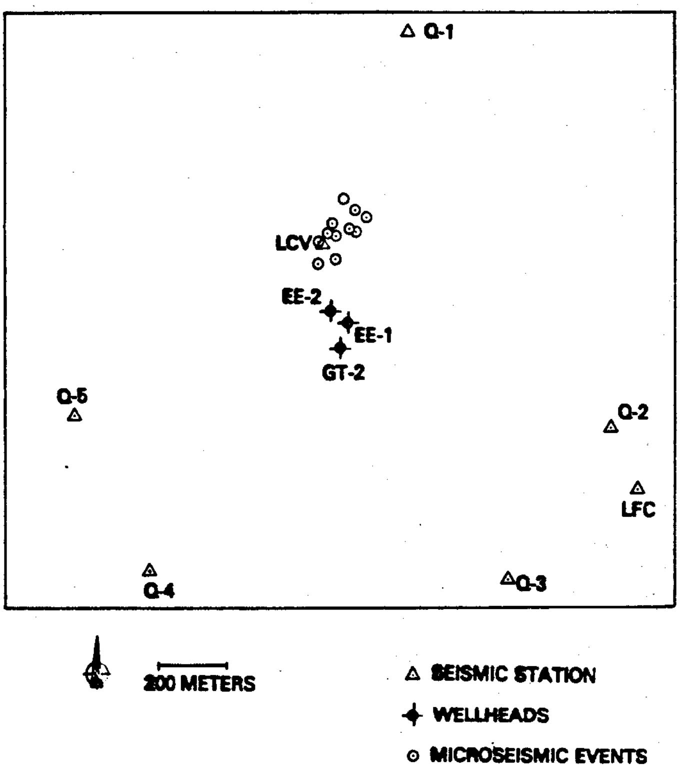

Fig. 9-2.
Plan view of location of seismic events that occurred during Run Segment 5.

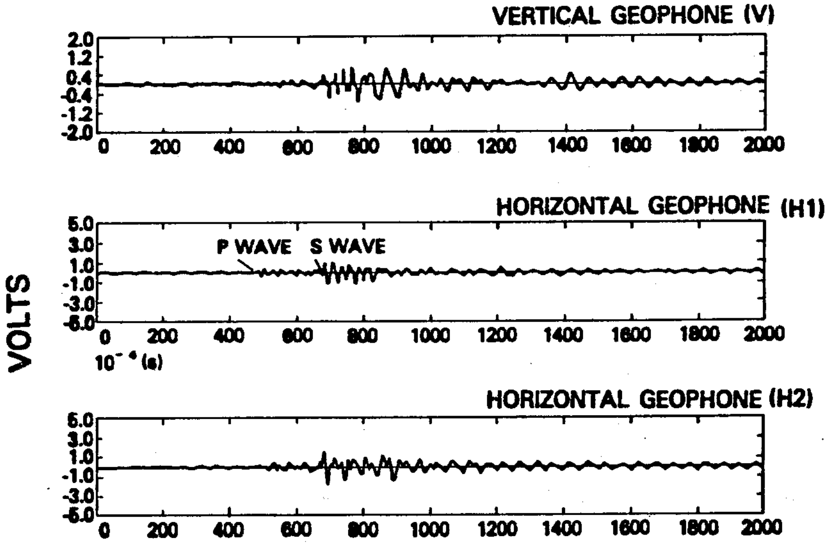

Fig. 9-3.
Sample event occurring during Run Segment 5.

10. CONCLUSIONS

The new reservoir, created by fracturing granitic rock at 2.93 km (9600 ft) and evaluated with a long-term (286-day) flow test, sustained an 8°C thermal drawdown. This result, along with the inlet-to-outlet spacing of 320 m, led to heat-transfer areas of 45 000 to 50 000 m^2, the range a result of different types of models. Measured tracer volumes suggest a fracture area of at least 80 000 m^2. Thus, all methods are in qualitative agreement with the fact that this reservoir is much larger than that evaluated in Run Segment 2, 75-day test, the first geothermal reservoir at Fenton Hill.

Water losses for the new reservoir were very encouraging because only a 30% increase in water loss was observed for a several-fold increase in heat-transfer area. The impedance remained constant throughout the experiment at about 1.6 GPa s/m^3, corrected for bouyancy. This is in contrast with the old reservoir that exhibited a sharp decline in the impedance. Presumably this was due to the large thermal drawdown that the old system experienced.

Geochemical monitoring of the system produced many valuable insights into the behavior of the system. In particular, geothermometry techniques provided a measure of the maximum reservoir temperature. It also established that this temperature qualitatively followed the drawdown pattern established with the outlet temperature. The concentrations of dissolved chemicals in the produced water were low and the pH was near neutral, so the produced water was of good quality.

Seismic monitoring of the new reservoir during Run Segment 5 showed very little seismic activity. The events that did occur were very small (less than -1.5 Richter) and were attributed to nearby drilling operations. Electrical power generation from hot dry rock was demonstrated with the operation of the 60 kW electrical power generation unit. Mechanical difficulties, however, prevented continuous operation of the unit.

ACKNOWLEDGMENTS

This work was supported by the Division of Geothermal Energy, US Department of Energy, and conducted under the overall supervision of G. Nunz, M. C. Smith, and R. W. Spence of the Hot Dry Rock Geothermal Energy Development Program Office and R. Brownlee, leader of the Geosciences Division, all at Los Alamos National Laboratory. Field operations and data acquisition at the Fenton Hill site were conducted by the Geothermal Operations Group headed by

B. Dennis, J. Hill, and R. Lawton. The efforts of B. Ramsay and G. Cremer in preparing and reviewing the manuscript for publication are gratefully acknowledged.

REFERENCES

1. M. C. Smith, R. L. Aamodt, R. M. Potter, and D. W. Brown, "Man-Made Geothermal Reservoirs," in Proc. Second United Nations Symp. on the Development and Use of Geothermal Resources, San Francisco, California, May 1975.

2. H. D. Murphy, R. G. Lawton, J. W. Tester, R. M. Potter, D. W. Brown, and R. L. Aamodt, "Preliminary Assessment of a Geothermal Energy Reservoir Formed by Hydraulic Fracturing," Soc. Petr. Engr. J. 17, 317-326 (1977).

3. J. W. Tester and J. N. Albright, Eds., "Hot Dry Rock Energy Extraction Field Test: 75 Days of Operation of a Prototype Reservoir at Fenton Hill," Los Alamos Scientific Laboratory report LA-7771-MS (April 1979).

4. H. D. Murphy and J. W. Tester, "Heat Production from a Geothermal Reservoir Formed by Hydraulic Fracturing--Comparison of Field and Theoretical Results," paper SPE 8265 presented at 54th Annual Mtg. of Soc. Petr. Engrs. of AIME, Las Vegas, Nevada, September 23-26, 1979.

5. J. W. Tester, R. M. Potter, and R. L. Bivins, "Interwell Tracer Analyses of a Hydraulically Fractured Granitic Geothermal Reservoir," paper SPE 8270 presented at 54th Annual Mtg. of Soc. Petr. Engrs. of AIME, Las Vegas, Nevada, September 23-26, 1979.

6. D. W. Brown, "Results of Expt. 186, The High Back-Pressure Flow Experiment," Los Alamos National Laboratory report LA-8941-HDR (to be published).

7. J. W. Tester, R. M. Potter, H. Fisher, and C. Pearson, "Massive Hydraulic Fracturing (MHF) and Associated Flow Testing [Experiments 195, 203, and 204]: Preliminary Results and Recommendations for Future Work," Los Alamos Scientific Laboratory G-5 internal report Tech. Memo #7 (March 27, 1979).

8. H. D. Murphy, Ed., "Preliminary Evaluation of the Second Hot Dry Rock Geothermal Energy Reservoir: Results of Phase 1, Run Segment 4," Los Alamos Scientific Laboratory report LA-8354-MS (May 1980).

9. L. Aamodt and G. Zyvoloski, "Report on Phase 1, Segment 5, Stage 1 (Start Up of Experiment 217)," Los Alamos Scientific Laboratory G-5 internal report Tech. Memo #5 (April 21, 1980).

10. H. D. Murphy, Ed., "Relaxation of Geothermal Stresses Induced by Heat Production," Los Alamos National Laboratory report LA-8954-MS (to be published).

11. H. N. Fisher and J. W. Tester, "The Pressure Transient Testing of a Man-Made Fractured Geothermal Reservoir: An Examination of Fracture Versus Matrix Dominated Flow Effect," Los Alamos Scientific Laboratory report LA-8535-MS (September 1980).

12. R. G. Lawton, "The AYER Heat Conduction Computer Program," Los Alamos Scientific Laboratory report LA-5613-MS (May 1974).

13. G. Zyvoloski, "Bottom-Hole Temperatures and Pressures for Experiment 217," Los Alamos Scientific Laboratory G-5 internal report Tech. Memo #11 (November 7, 1980).

14. R. D. McFarland and H. D. Murphy, "Extracting Energy from Hydraulically Fractured Geothermal Reservoirs," in Proc. 11th Intersociety Energy Conversion Engineering Conference, State Line, Nevada, September 12-17, 1976.

15. H. D. Murphy, J. W. Tester, C. O. Grigsby, and R. M. Potter, "Energy Extraction from Fractured Geothermal Reservoirs in Low Permeability Crystalline Rock," to appear in J. Geophys. Res. (July 1981).

16. F. H. Harlow and W. E. Pracht, "A Theoretical Study of Geothermal Energy Extraction," J. Geophys. Res. 77, 7038-7048 (1972).

17. H. D. Murphy and R. G. Lawton, "Downhole Measurements of Thermal Conductivity in Geothermal Reservoirs," Trans. ASME Petr. Div., Series J 99, 697-611 (1977).

18. T. K. Perkins and L. R. Kern, "Widths of Hydraulic Fractures," J. Petroleum Tech., 937-946 (September 1961).

19. J. Geertsma and F. de Klerk, "A Rapid Method of Predicting Width and Extent of Hydraulically Induced Fractures," J. Petroleum Tech., 1571-1581 (December 1969).

20. A. A. Daneshy, "On the Design of Vertical Hydraulic Fractures," J. Petroleum Tech., 83-87 (January 1973).

21. H. D. Murphy, "Thermal Stress Cracking and the Enhancement of Heat Extraction from Fractured Geothermal Reservoirs," Geothermal Energy 7, 22-29 (1979).

22. G. W. Morey, R. O. Fournier, and J. J. Rowe, "The Solubility of Quartz in Water in the Temperature Interval from 25°C to 300°C," Geochimica et Cosmochimica Acta 26, 1029-1043 (1962).

23. R. O. Fournier and A. H. Truesdell, "Chemical Indicators of Subsurface Temperature, Part 2: Estimation of Temperature and Fraction of Hot Water Mixed with Cold Water," J. Res. U.S. Geol. Surv. 2, 263-270 (1974).

24. R. W. Charles, "Experimental Geothermal Loop: II. 200°C Study," Los Alamos Scientific Laboratory report LA-7735-MS (April 1979).

25. O. Levenspiel, Chemical Reactor Engineering, 2nd ed. (John Wiley and Sons, New York, 1962) p. 258.

26. C. O. Grigsby, J. W. Tester, P. E. Trujillo, D. A. Counce, J. Abbott, C. E. Holley, and L. A. Blatz, "Rock-Water Interactions in Hot Dry Rock Geothermal Systems: Field Investigations of In Situ Geochemical Behavior Under Recirculating Conditions," in preparation, to be submitted to special Hot Dry Rock issue of J. of Volcanology and Geothermal Research (1981).

27. W. F. Giggenbach, "Geothermal Gas Equilibria," Geochimica et Cosmochimica Acta, 44, 2021-2032 (1980).

28. W. F. Giggenbach, "Geothermal Mineral Equilibria," Geochemica et Cosmochimica Acta, 45, 393-410 (1981).

29. A. W. Laughlin and A. Eddy, "Petrography and Geochemistry of Precambrian Rocks from GT-2 and EE-1," Los Alamos Scientific Laboratory report, LA-6930-MS (August 1977).

30. J. N. Andrews, and D. F. Wood, "Mechanism of Radon Release in Rock Matrices and Entry Into Groundwaters," Institution of Mining and Metallurgy Transactions/Section B, 81, No. 792 (November 1972).

31. A. Stoker and P. Kruger, "Radon in Geothermal Reservoirs," Proc. of the 2nd U.N. Symp. on the Development and Use of Geothermal Resources, (San Francisco, California, 1975).

32. P. Kruger, G. A. Cederberg, and L. Semprini, "Radon Data - Phase I Test, Los Alamos Scientific Laboratory Hot Dry Rock Project, January 28-April 27, 1978," Stanford Geothermal Program technical report SGP-TR-27 (1978).

33. B. J. Skinner, "Thermal Expansion," in Handbook of Physical Constants, S. P. Clark, Jr. Ed. (Geol. Soc. Amer., New York, 1966).

34. D. W. Brown, "Dresser-Atlas Iodine Tracer Logs - Experiment 116," Q-11 memo, November 17, 1976.

35. R. Potter, "The Use of Radioactive Tracers in HDR Reservoir Studies," G-3 Tech. Memo #5 (March 14, 1979).

36. Los Alamos Scientific Laboratory HDR Project Staff, "Hot Dry Rock Geothermal Energy Development Project: Annual Report Fiscal Year 1977," Los Alamos Scientific Laboratory report LA-7109-PR (February 1978).

37. M. C. Brown, G. J. Nunz, G. M. Cremer, and M. C. Smith, "Hot Dry Rock Geothermal Energy Development Program: Semiannual Report October 1, 1978-March 31, 1979," Los Alamos Scientific Laboratory report LA-7959-HDR (September 1979).

38. Los Alamos Scientific Laboratory HDR Program Staff, "Hot Dry Rock Geothermal Energy Development Program: Annual Report Fiscal Year 1978," Los Alamos Scientific Laboratory report LA-7807-HDR (April 1979).

39. G. M. Cremer, R. B. Duffield, M. C. Smith, and M. G. Wilson, Compilers and Editors, "Hot Dry Rock Geothermal Energy Development Program" Annual Report Fiscal Year 1979," Los Alamos Scientific Laboratory report LA-8280-HDR (August 1980).

APPENDIX A

DEFINITIONS OF THE INTEGRAL MEAN <V>, THE MODE $\mathring{V}$, AND TRIMMED MEAN |V| VOLUMES

Because the dye tracer results express a continuous residence time distribution (RTD), they can be viewed as a probability distribution function. Consequently, a statistical analysis may enhance our understanding of the system. In light of this, calculations were done to provide modes and integrated and trimmed means of the observed RTDs as presented in Table 8-I. Integrations of the distribution are required to produce means and medians and are biased toward large volumes or residence times because of the long tails observed in the distributions. The mode, on the other hand, eliminates this dependence and may be a more accurate estimate of the central tendency of the distribution.

The volumes are defined as follows.

Modal volume:

$\mathring{V}$ occurs when $C_i = f(V_i)$ is a maximum.

Mean volume:

$$\langle V \rangle = \int_0^\infty VC_i dV \int_0^\infty C_i dV \quad .$$

Trimmed mean volume:

$$|V| = \int_0^{V^*} VC_i dV \int_0^{V^*} C_i dV \quad ,$$

where $\{o,V^*\}$ defines the trimmed distribution of tracer concentration C_i and measured volume V. The spread of the distribution is proportional to the degree of dispersion and can be represented by the statistical variance σ_ϕ^2;

$$\sigma_\phi^2 = \int_0^\infty V^2 C_i dV \quad \langle V\rangle^2 \int_0^\infty C_i dV \quad -1 \ .$$

Values of σ_ϕ^2 for various levels of truncation are presented in Table 8-II.

APPENDIX B

SAMPLING AND ANALYSIS PROCEDURES FOR RUN SEGMENT 5

1. WATER SAMPLING PROCEDURES

Liquid samples were collected from the GT-2 production wellhead through a sampling line that entered directly into the chemistry laboratory. Inside the laboratory, the fluid was cooled in a commercial heat exchanger at the production pressure. Sufficient fluid was discarded before samples were collected to completely flush the sample line and thus ensure a fresh sample was being taken. The fluid was sampled either after filtration through a 0.45-μm Gelman membrane filter in a stainless-steel high-pressure holder or directly, unfiltered.

Samples of injected fluid were collected at a sampling station located near the injection well, and system make-up water samples were collected at a location near the make-up water pumps. Because of the lower temperatures encountered at these locations, no heat exchanger was needed for sample cooling. Here again provisions were made for collecting both filtered and unfiltered samples.

A sample set for each location consisted of the following.

1. A 500-mℓ unfiltered sample for total suspended solid (TSS) determination.
2. A 500-mℓ filtered sample for anion analysis.
3. A 500-mℓ filtered sample for cation analysis. This sample was acidified to 0.1% with concentrated HNO_3.

4. A 500-mℓ filtered sample for aluminum determination.
   This sample was immediately treated according to the method of Barnes for the extraction of monomeric aluminum.
5. A 1-ℓ filtered sample for trace analysis.
6. A 50-mℓ filtered sample for strontium isotope analysis.
7. A 125-mℓ unfiltered sample for oxygen and hydrogen isotope analysis.

All the above samples were collected in sample bottles that had been rinsed at least twice with their volume of the sample liquid immmediately prior to collection. The first six samples were collected in new Nalgene bottles and the oxygen-hydrogen isotope sample was collected in a flint glass bottle with a Polyseal™ cap. All bottles were filled completely to eliminate air pockets and then tightly sealed. A strip of tape was used around the flint glass bottles as an extra precaution against leakage.

2. WATER ANALYSIS PROCEDURE

2.1. Total Suspended Solids (TSS)

Gelman 0.45-μm membrane filters were first dried at 30°C for at least 12 h and cooled at room temperature in a desiccator. Each filter was weighed to 0.1 mg before use, and a series of blanks were run to determine the average weight loss of the filter during this procedure. Both blanks and samples were run by first placing a weighed filter in a special filter holder and then forcing blank or sample through the filter using air pressure at 5 bars into a large beaker. After filtering the entire liquid volume, the filter with the collected solids was dried and cooled as before and then weighed. The collected filtrate volume was measured to the nearest 10 mm, and the weight of solids per volume of liquid was calculated in milligrams/liter from the increased weight of the filter. A correction was made in the calculations by taking the average weight loss obtained on the blank runs and adding it to the weight of the collected solids. The relative standard deviation (RSD) for the analysis was ±20%.

2.2. PH, EH, HCO_3^-,CO_3^{-2} and Conductivity

These analyses were performed as soon as possible after collection and immediately after opening the sample bottles. The pH and Eh electrodes were standardized daily with standard solutions using the same conditions as the samples. EPA quality control samples of known pH and HCO_3^- content were included with each group of samples to regulate the uniformity of the tests and to check the accuracy of the results.

Sample aliquots of 100 mℓ were poured into small beakers with a minimum of handling to avoid loss of dissolved gases. The electrodes were inserted in each sample, and pH and Eh readings were recorded while stirring gently with a magnetic stirrer. The maximum time allowed for each electrode reading was determined during standardization done before the analysis. The HCO_3^-/CO_3^{-2} determination followed directly and used the final pH reading as a starting point. The sample aliquot was titrated with 1.589 $\underline{N}$ H_2SO_4 using a HACH Digital Titrator cartridge to give a pH titration curve. The first end point of the titration at pH 8.3 (usually absent in the loop samples) was indicative of the CO_3^{-2} content in the sample whereas the second end point at pH 4.5 indicated the HCO_3^- content. The relative standard deviations for the pH and HCO_3^-/CO_3^{-2} measurements were ±2% and ±4% respectively. A much larger error, which was associated with the Eh analysis, was due to actual oxidation potential changes during measurement caused by the effects of temperature and the nature of the chemical systems operating in the solution.

Conductivity was measured with a conductivity probe using deionized water as a blank to adjust the baseline reading. Conductivity was read directly off a meter and reported in micromho/centimeter.

2.3. Silica

Silica analyses were performed on an aliquot of filtered acidified sample using the silicamolybdate method in which a color reagent of ammonium molybdate and sulfuric acid produces a yellow color with an intensity proportional to the reactive silica in solution. Because silica is found in glassware and can be present in many reagents, only plastic (usually Nalgene) equipment was used and blanks were run to correct for silica contamination.

The procedure used was as follows. A 0.2-mℓ aliquot of sample and a standard containing 250 ppm of SiO_2 were pipetted into the suitable plastic containers. Approximately 9.8 mℓ of the color reagent were added to each sample or standard. The resulting mixture was agitated, and the mixture was allowed to stand 10 min before reading the absorbance at 400 nm on a uv spectrophotometer. The spectrophotometer used to measure silica was a Beckman Model 25 equipped with an automatic concentration calibrating mode and a "sipper cell," which pumped the sample directly into the light path. Blank solutions were used to set the zero reading, and the 250-ppm standard was used to set the concentration dial to 250. Samples introduced into the instrument through the cell gave readings, which corresponded directly to silica concentrations. All standards were run in triplicate, and samples were run in duplicate due to the relative ease of silica contamination. Quality control for this analysis was done by comparing standards and by analyzing a laboratory prepared standard sample similar to the loop fluid. The relative standard deviation for the proocedure was ±4%.

2.4. Boron

Several 1-mℓ aliquots of filtered unacidified sample or standard were treated with 2 mℓ of ammonium acetate buffer and 2 mℓ of azomethime-H solution according to the method described by Meglen. The resulting color complex reached a peak intensity after 30 min when it was measured using the Beckman spectrophotometer described for silica analysis. A calibration curve of absorbance vs concentration was constructed from standard and blank readings. Since the range of the curve for standards from 0 to 10 ppm was linear, a linear regression program was used to calculate sample concentrations from their absorbance readings. The correlation coefficient for a typical curve of five standards from 0 to 10 ppm ranged between 0.9989 to 1.0000. The precision of the method was ±3% RSD. The standard described in the silica procedure was also used successfully as a quality control check.

2.5. Atomic Absorption Analysis

The following major cations were analyzed by atomic absorption spectroscopy (AA) using an air-acetylene flame: Ca, K, Na, Mg, and Li. For these analyses, all samples and standards were diluted at least 50% with a solution containing 2000 ppm Cs in 1% HNO_3 to eliminate ionization interferences. In addition to the Cs, a 5% La solution was used in a 1 to 4 ratio to eliminate molecular interferences caused by high sulfate and silica during the analysis of Ca and Mg. The low-temperature air-acetylene flame was preferred to other flames because of the higher absorbance to concentration ratios obtained.

The instrument used for these determinations was the Perkin Elmer Model 460. Instrument parameters were optimized for each elemental determination, and standardization was done using the automatic calibration option on the instrument. To eliminate errors introduced by high-order dilution, burner head angles on the instrument were rotated to reduce sensitivity and increase the linear working ranges. Initial samples were run against prepared standards and by standards prepared by the method of addition; however, when this was no longer deemed necessary, standardization was done only with prepared standards and comparisons were made with EPA standards. As a double accuracy check, different dilutions of each sample were prepared and checked against each other until at least two gave results in the same working range. This method not only yielded duplicate results but was also very valuable in detecting matrix interferences. The relative standard deviations for each analysis were as follows: Ca = ±1.4%, K = ±1.2%, Li = ±1.2%, Mg = ±1.4%, and Na = <±1%.

Silicon analyses, when required, were done by AA using a nitrous oxide-acetylene flame because atomization of silicon compounds requires higher temperatures. For convenience, sample dilutions for silicon were those already prepared for use with the air-acetylene flame. Silicon standards were prepared for analysis in the same manner as the actual samples.

Monomeric aluminum was determined by AA using a graphite furnace after extraction and concentration of the monomeric aluminum into methylisobutyl ketone (MIBK). This extraction was performed immediately after collection and was done as follows. To remove iron interferences present in the loop fluid by reduction of Fe^{+3} to Fe^{+2} and to complex the iron, 5 mℓ of 20% hydroxylamine hydrochloride and 5 mℓ of 2% phenanthroline 1, 10 solution were added to 500 mℓ of sample. The pH was then adjusted to 4. After removal of the interfering iron, the aluminum was extracted by adding 2 mℓ of 5% hydroquinoline and buffering the solution to pH 8.3. Twenty milliliters of MIBK were added to the buffer, and the Al complex in the buffer was extracted into the organic phase (MIBK). The MIBK phase was separated and analyzed. Blanks and standards were prepared by the same procedure. EPA standards as well as prepared standards were run routinely, and the relative standard deviation for the entire extraction and analysis was about ±10%. This relatively large error term was carried primarily by instability in the samples during storage of the organic phase.

Trace analyses were also analyzed by AA and were done only on selected samples after completion of the experiment. Elements in this category included: Ag, Ba, Cd, Co, Cr, Cu, Fe, Ni, Mn, Mo, Pb, Sr, and Zn. In all cases, filtered acidified samples were used and the HGA model 5000 graphite furnace was used. Multiple dilutions were made to check for matrix interferences, and a deuterium arc background correction was used on elements with analytical spectral lines below 400 nm. Whenever possible, EPA standards accompanied the samples as a check for accuracy. Relative standard deviation for the trace elements ranged from ±5% to ±40%.

Anion analyses of Cl^-, F^-, NO_3^-, SO_4^{-2}, PO_4^{-3}, and Br were done simultaneously using a Dionex Model 12 Ion Chromatograph on the filtered unacidified samples. Each sample being analyzed was loaded into a sample tube, which contained a small volume of effluent concentrate. When necessary, dilutions of the samples were made in the sample tubes before analysis. The concentrate was added to minimize effects of the "water dip," which is sometimes associated with ion chromatography. Retention times and peak areas from this chromatograph were measured on a Spectra-Physics Minigrator.

Calibration curves for each anion were prepared with each set of samples by inserting mixed anion standards with the samples. These mixed standards were prepared from dilution of individual primary standards prepared gravimetrically for each anion. A further check on the accuracy of the method and the calibration curves was made by including EPA standard solutions with each set of samples. Approximately 30 min were required by the ion chromatograph for each sample. A linear regression program was used for calculating concentrations from the corresponding peak areas. In most cases, the RSD for analysis with the ion chromatograph was within ±5%.

3. DISSOLVED GAS SAMPLES

The apparatus for gas sampling consisted of a 4-ℓ high-pressure stainless-steel separator tank and a 1-ℓ tank in an ice bath used to trap condensible vapors. The inside of the separator tank was fitted with a stainless steel tube drilled with 15 1/8-in. holes that were designed to spray incoming fluid inside the tank.

Samples were collected by slightly opening the intake valve on the tank and allowing liquid to flash inside the separator for 3 min with the drain valve open. When the gas and liquid phases in the tank had reached equilibrium, the drain valve was shut and a pressure of 15 psi was allowed to build up in the tank. The intake valve was then closed, and the contents of the separator were allowed to stand for another 2 min to further separate the phases. At 2 min, the outlet valve on top of the separator tank was momentarily opened and then closed to transfer some of the gas into the 1-ℓ cold-trap tank. A gas sample from this tank was extracted with a gas syringe by inserting the needle of the syringe into a septum connected to the tank and opening the sampling valve. The above procedure was repeated three times to flush the system before taking a final gas sample for analysis.

The sample in the syringe was analyzed by injection into a Carle Automatic Gas Chromatograph (GC) equipped with a thermal-conductivity detector. The sample loop of the chromatograph was thoroughly flushed with sample before each analysis cycle was started. A positive pressure was always kept on the contents of the syringe to prevent air contamination. Peak areas and retention times for the chromatograph were measured with a Spectra-Physics Minigrator.

Calibration of the GC was performed daily using a standard calibration gas, which was prepared by using partial pressure to mix gases in a small gas tank. The mixture in the tank was standardized against calibration curves, which were determined from gas mixtures containing measured volumes of pure gases. For the actual working range of the GC, the error associated with the instrument was about ±2% RSD.

Because concentrations of H_2S encountered during the experiment were below the detection range of the GC, a fraction of the gas sample was saved for a separate H_2S analysis. The sample gas was diluted with pure nitrogen gas in a special gas sampling bag and introduced into an Ecolyzer H_2S analyzer. Calibration of this instrument was performed using tanks of standard gas supplied with the instrument.

☆ U.S. GOVERNMENT PRINTING OFFICE: 1981-0-777-022/130